Coherent transfer between electron and nuclear spin qubits and their decoherence properties

Richard M. Brown

Linacre College

A thesis submitted for the degree of Doctor of Philosophy

at the University of Oxford

Hilary Term 2011

Linacre College, 2012.

Typeset in LaTeX 2$_\varepsilon$.

Coherent transfer between electron and nuclear spin qubits and their decoherence properties

Richard M. Brown

Linacre College

Hilary Term 2011

Abstract of a thesis submitted for the degree of Doctor of Philosophy

Conventional computing faces a huge technical challenge as traditional transistors will soon reach their size limitations. This will halt progress in reaching faster processing speeds and to overcome this problem, require an entirely new approach. Quantum computing (QC) is a natural solution offering a route to miniaturisation by, for example, storing information in electron or nuclear spin states, whilst harnessing the power of quantum physics to perform certain calculations exponentially faster than its classical counterpart. However, QCs face many difficulties, such as, protecting the quantum-bit (qubit) from the environment and its irreversible loss through the process of decoherence.

Hybrid systems provide a route to harnessing the benefits of multiple degrees of freedom through the coherent transfer of quantum information between them. In this thesis I show coherent qubit transfer between electron and nuclear spin states in a $^{15}N@C_{60}$ molecular system (comprising a nitrogen atom encapsulated in a carbon cage) and a solid state system, using phosphorous donors in silicon (Si:P). The propagation uses a series of resonant microwave and radiofrequency pulses and is shown with a two-way fidelity of around 90% for an arbitrary qubit state. The transfer allows quantum information to be held in the nuclear spin for up to 3 orders of magnitude longer than in the electron spin, producing a $^{15}N@C_{60}$ and Si:P 'quantum memory' of up to 130 ms and 1.75 s, respectively. I show electron and nuclear spin relaxation (T_1), in both systems, is dominated by a two-phonon process resonant with an excited state, with a constant electron/nuclear T_1 ratio. The thesis further investigates the decoherence and relaxation properties of metal atoms encapsulated in a carbon cage, termed metallofullerenes, discovering that exceptionally long electron spin decoherence times are possible, such that these can be considered a viable QC candidate.

Acknowledgements

There are many people whom I would like to acknowledge for helping me throughout my DPhil and in producing this thesis. Firstly, I would like to especially thank my supervisor John Morton, for teaching me EPR, his helpful advice and for always having the time to answer my numerous questions. I would also like to express my thanks to my supervisors Arzhang Ardavan and Andrew Briggs, for their constant support and useful discussions regarding my work. I extend my gratitude to Steve Lyon and my collaborators at Princeton University for working with me and allowing me to conduct experiments there. In particular, I thank Alexei Tyryshkin for his expertise on 'all things EPR'. I am indebted to Jeff Harmer who has the sometimes less than desirable job of running and maintaining the Oxford CAESR facility. Likewise, I am indebted to the numerous personnel whom have produced samples for me, in particular working closely with Kyriakos Porfyrakis, Simon Plant and Yasu Ito on the preparation of fullerene materials. I also specifically acknowledge materials preparation at the Lawrence Berkeley National Laboratory, Leibniz-Institut für Kristallzüchtung, PTB Braunschweig, VITCON Projectconsult GmbH and the labs of Hisanori Shinohara, Mike Thewalt and Kohei Ito. I thank Erik Gauger and Brendon Lovett for helping me with theoretical aspects of my work, Mathematica and time spent finding factors of two. I express my gratitude to Stephanie Simmons for collaborating on entanglement and nuclear relaxation, her help with the AFQ, red bull and in the same sentence thank Mr Scruff. I also extend my appreciation to Steve Karlen and Richard George, the

latter for his discussions and help on many aspects, including, coding and electronics. I further acknowledge funding from the EPSRC through project IMPRESS, QIP IRC and CAESR grants.

I more generally thank all those in the QIP building and the QSD group which has been a stimulating environment to work in. I particularly appreciate all in 'the basement' office which has been great fun to work in, Vasileia and Hua for Matlab help, Rizvi for his numerous scientific discussions and Muj for the in depth analysis of all sports, especially fantasy football (this year i will beat you!). I would like to say 'cheers' to all my friends in Oxford and at Linacre College, with whom I have shared many great times and of course all those not at Oxford as well! I also thank the Linace/Corpus MCR football team for all the football over the years. On a similar note, I am indebted to Gaz and 'the Gummies', as without the regular 9-a-side I would have probably gone crazy. Finally, I thank my family, my parent and grandparents for supporting me and for helping put me through university. Last, but my no means least, I extend the most thanks to Sally for giving me constant support and happiness, being a 'PhD widow' and commuting every day whilst I was still in bed.

Contents

1

Introduction to Quantum Information Processing (QIP)

1.1 Introduction

Classical silicon based computers have advanced at a relentless rate in the quest for more processing power. Moore's law accurately describes this exponential growth, observing that the number of transistors per chip is doubling every 18-24 months.[1] However, Moore's law is clearly not sustainable and at some point the limit to miniaturisation must be met, certainly when transistors are atomic in size. On this scale,

[1]Originally Moore in 1965 predicted the doubling of the number of transistors per chip every 12 months, this was revised in 1975 to every 24 months and allegedly by a colleague to 18 months.

the classical principles that govern a Church-Turing machine[2] will no longer be valid and quantum mechanics must be taken into account. This allows us to produce a new kind of computer, the quantum computer (QC), which has the potential to perform certain tasks exponentially faster than its classical counterpart.

The concept of a quantum computer was proposed by Feynman [Fey82] in 1982 with the premise of using it to simulate quantum mechanical systems. It later became clear that quantum computing could promise significant improvement over its classical counterpart for a number of applications. The first example of this was shown by David Deutsch [Deu85] in 1985 who explored the use of quantum mechanics in a computer, but for a somewhat artificial problem. It was not until 1994 that Shor's algorithm [Sho94] was developed with the ability to factorise large integer numbers, that the promise of quantum computing was truly appreciated. The inefficiency of this type of factorisation using a classical computer[3] forms the basis of much of today's cryptography, hence the algorithm significantly increased interest in the area. Further applications in which it is believed quantum computing will show an improvement in efficiency over classical computing includes solving discrete logarithms [Sho94] and database searching [Gro99].

1.2 Building a quantum computer

1.2.1 The qubit

The fundamental element of a quantum computer is the quantum bit or qubit. It is analogous to the classical bit in that it must reliably distinguish two orthogonal states often represented as $|0\rangle$ and $|1\rangle$. However, the qubit actually allows an infinite possibility of states and hence contains much more information than a simple bit. The qubit states can be represented by the Bloch sphere, shown in Figure 1.1, whereby the poles represent $|0\rangle$ and $|1\rangle$ and the sphere surface the states given by a superposition of

[2] A 'classical' computer often abbreviated to a Turing machine.
[3] By any known classical algorithm.

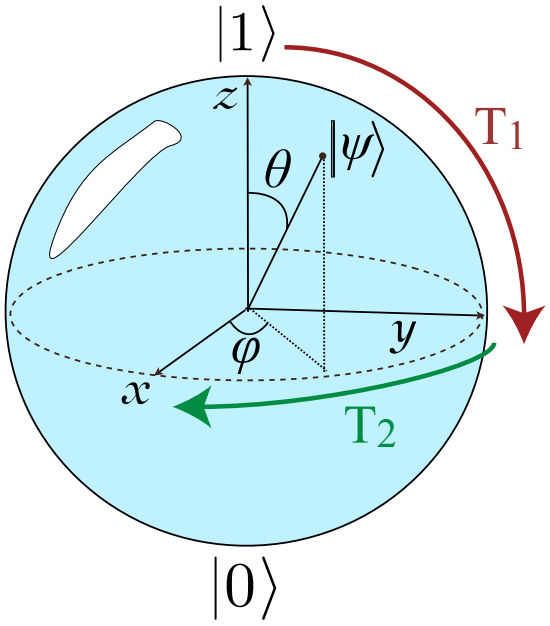

Figure 1.1: Bloch sphere with two decoherence mechanisms T_1 and T_2 as described in Section 1.2.2.

both $|0\rangle$ and $|1\rangle$ described by $|\psi\rangle = \alpha|0\rangle + \beta|1\rangle$, where α and β are complex numbers. Using the Bloch sphere notation this can be written using just two free parameters θ and ϕ, Equation (1.1), where $0 \leq \theta \leq \pi$ and $0 \leq \phi \leq 2\pi$

$$|\psi\rangle = \cos\left(\frac{\theta}{2}\right)|0\rangle + \sin\left(\frac{\theta}{2}\right)\exp(i\phi)|1\rangle \tag{1.1}$$

The power of the qubit becomes apparent when considering multiple qubit systems. A two qubit system is given by $|\psi\rangle = \alpha\alpha\,|00\rangle + \alpha\beta\,|01\rangle + \beta\alpha\,|10\rangle + \beta\beta\,|11\rangle$ with the number of coefficients scaling exponentially with the number of qubits, such that an N-qubit system is described by 2^N coefficients[4]. However, most of the quantum information stored within the wavefunction amplitudes will be lost due to the collapse of the wavefunction during measurement. Therefore in order to gain an advantage over

[4]the Hilbert (vector) space is described by 2^N coefficients in general but only if entangled states are considered. Without entanglement, the number of coefficients needed is 2N and the exponential enhancement is lost. A K-dimensional Hilbert space can be described by just K×(K-1)/2 complex numbers and K real numbers, and with only 2 qubits an infinite number of entangled states are found (i.e. $|00\rangle + \exp i\phi\,|11\rangle$ are entangled for any value of ϕ).

classical computing the qubit must be manipulated without measurement[5]. This is the basis of quantum parallelism as employed by quantum algorithms, such as those shown by Deutsch [Deu85], Shor [Sho94] and Grover [Gro99].

1.2.2 QIP qubit criteria

Implementation of a quantum computer requires five (plus two) main criteria to be met, as identified by DiVincenzo [DiV00]:

1. **A scalable physical system with well characterised qubits:** To describe a qubit, a quantum two level system is required. The qubit must further be scalable to multiple qubits systems with, for example, the ability to form entangled states (discussed further in Section 1.4). DiVincenzo points out that this is not completely straightforward as acceptable single qubit systems may not be able to produce multiple qubit entanglement e.g. one-electron quantum dots (due to super selection principles). In order to manipulate qubit states they must be 'well characterised' such that the internal Hamiltonian (hence energy eigenstates, often representing the $|0\rangle$ and $|1\rangle$ states), external interactions and couplings are known. Furthermore, the qubit should have a very low probability of excitation to any higher (energy) levels present, as this would be catastrophic to the qubit states.

2. **The ability to initialise the state of the qubit:** A computation requires the initial value of the state to be known before commencing and error correction further requires this state to be of low entropy, namely the state $|0\rangle$. The initialisation of the system must also be quick compared to the manipulation time. This is a problem for many proposals as initialisation is often slow via cooling or magnetic alignment techniques. Slow initialisation will also be problematic for implementing error correcting codes which require a continuous supply of $|0\rangle$ state qubits.

3. **Long coherence times, much longer than the gate operation time:** Decoherence is a fundamental process of a quantum system marking the onset of classical

[5]This does not apply to 'one-way' or measurement based QC, discussed in Section 1.6.

behaviour. The relevant decoherence time is therefore effectively a measure of how long information can be held in a system before it is irreversibly lost. Using the Bloch sphere two decoherence times are observed, T_1, a measurement of the corruption in θ and T_2, a measurement of the corruption in ϕ. Naming convention varies for these and although both lead to decoherence, I will refer to T_2 as the decoherence (coherence) time and T_1 as the relaxation time. T_2 merits particular attention as it does not require energy exchange with the environment and hence is generally the shorter of the two. The discovery of error correcting codes [Sho95, Ste96] allows for some probability of decoherence during computation, without destroying the ability of the quantum computer to perform a calculation. It was further shown that 'good' error correction codes could be implemented [CS96] and that fault tolerant quantum error correction (QEC) could be achieved [DS96, Pre98]. This relies on a number of ancillary qubits to detect and correct information that has decohered, without interfering with a computation. To allow QEC, the minimum decoherence time must be at least $10^3 - 10^6$ times longer than the time in which it takes to manipulate the qubit i.e. the gate time. However, it is preferable to have longer decoherence as this simplifies QEC and the associated number of ancillary qubits.

4. **A 'universal' set of quantum gates:** Classical computers use a set of logic operations or gates to perform a computation, the simplest of which is the NOT gate converting $|1\rangle$ to $|0\rangle$ and $|0\rangle$ to $|1\rangle$. Similarly, to perform quantum algorithms a set of quantum gates are required that cover all logic operations and thus are 'universal'. This corresponds to two single qubit gates giving rotations about any two axes of the Bloch sphere and subsequently, using Euler decomposition, any arbitrary rotation around the Bloch sphere. To make the set universal a final two qubit gate [BBC95] is needed such as the control-NOT or control-phase which is often applied by the turning on and off of qubit-qubit interactions. The application of gates varies with the qubit architecture and is explored in more detail in Chapter 1.4.

5. **A qubit-specific measurement capability:** To complete a computation the output of a qubit must be read with high efficiency. If a high efficiency cannot be

achieved then rerunning or 'copying' of qubits can be implemented[6] or alternatively computing can be conducted on an ensemble of qubits simultaneously (see Section 1.3). However, single spin detection is desirable in order to scale the number of qubits and, although challenging, most QIP schemes rely on such readout.

DiVincenzo also cites two further criteria primarily for quantum communication, **(6.) the ability to interconvert stationary and flying qubits** and **(7.) to faithfully transmit these flying qubits**. Here 'flying' qubits simply refer to qubits that will travel from one desired location to another in order to transmit quantum information. However, a quantum computer may employ flying qubits to transmit information between smaller qubit arrays in order to limit decoherence or for qubit-qubit interaction to implement two qubit gates [BAB06].

1.2.3 QIP proposals

To date, no QIP proposal has been produced that completely fulfils all the criteria in Section 1.2.2. Nevertheless, a number of different qubit systems have been suggested. These include nuclear spin [CFH97, Kan98], electron spin [Kan98, Llo93], electronic configuration [CZ95], photon polarisation [CY95] (cavity QED) [SW95], superconducting circuits [PdGHM07], Bose Einstein condensates [CZ02] and the presence or absence of an exciton [BdZR02]. These proposals possess advantages and disadvantages with respect to the DiVincenzo criteria, for example, nuclear spins have very long decoherence times and so are perfect for criterion 3 but do not fulfil criterion 1 or 2 (see Section 1.3). The Los Alamos Quantum Computing Roadmap [LANL] extensively examines the viability of some major proposals and a summary is given in Figure 1.2. However, these are very general areas and break down into further sections. For instance, superconducting circuits can use either 'flux', 'charge' or 'phase' qubits resulting in different properties. Furthermore, proposals may be viable within DiVincenzo's criteria but drawbacks may mean other systems may be more preferable. For example,

[6]The no-cloning theorem prevents actual copying of a qubit state [WZ82].

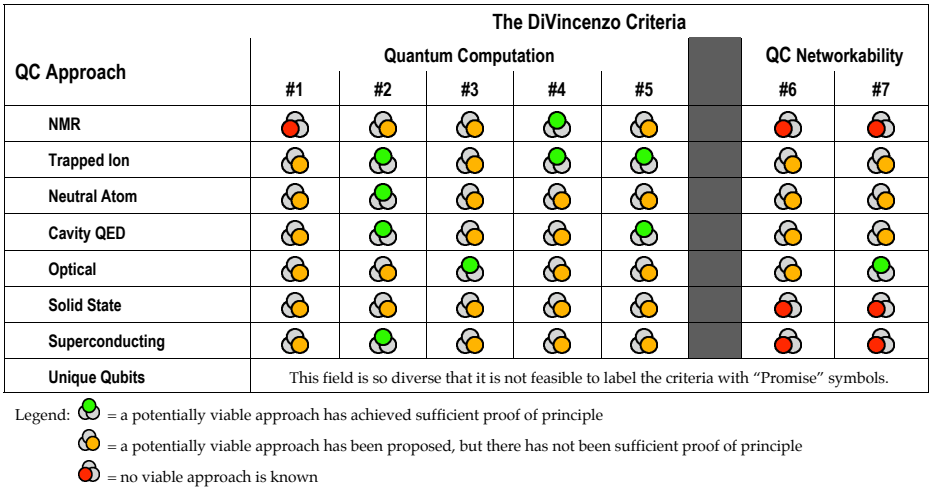

Figure 1.2: The Los Alamos Quantum Computing Roadmap, where $\#x$ refers to DiVincenzo's criteria and large general proposals are considered [LANL]. Copyright 2011 Los Alamos National Security, LLC All rights reserved.

a superconducting flux qubit has a decoherence time in the order of μs [BCB05], this is on the limit of error correction with gate times of the order of ns and hence may be viable, but would require many ancillary corrective qubits. The choice of architecture the qubit can be implemented into also varies as will be apparent in Section 1.3. Schemes range from those similar to a classical computation employing gates [Kan98], to those that use flying qubits and global control [BAB06]. Choice of a qubit system is complicated and predicting which of these may finally provide a quantum computer is not straightforward.

1.3 Spin Systems for QIP

1.3.1 Nuclear and electron spin systems

Using the nuclear or electron spin is a logical way to represent a qubit, with the Zeeman energy splitting in an applied magnetic field providing a natural two level quantum system. The differing energy levels of the aligned or anti aligned magnetic moment (spin 'up' or 'down') can refer to the states $|1\rangle$ and $|0\rangle$ respectively. The Zeeman energy

splitting is given by $\mu_n g_n B_0$ for a nuclear spin system and $\mu_B g_e B_0$ for an electron spin system where μ_n and μ_B are the nuclear and Bohr magnetons, g_n and g_e are the nuclear and electron spin g-factors and B_0 the applied magnetic field. However, the Zeeman splitting for a ^{1}H nuclei is 658 times weaker than that of an electron spin (due to a smaller magnetic moment), with other nuclei even weaker e.g. 1624 times smaller for a ^{31}P nuclei, as exploited within this thesis. The Zeeman splitting can be addressed with a resonant microwave field (GHz) for an electron i.e. electron paramagnetic resonance (EPR) or radiofrequency (MHz) for a nuclei i.e. nuclear magnetic resonance (NMR). Applying a continuous resonant ac field will drive transitions between $|0\rangle$ and $|1\rangle$ to give sinusoidal Rabi oscillations. A one-qubit gate can thus be performed by applying a resonant field for a given time equal to half a Rabi period (a π pulse).

The use of NMR for QIP was quickly established as a promising technique due to the existing expertise within the area. However, the small Zeeman splitting for nuclei poses a fundamental problem for initialisation of nuclear spins to a pure state at experimental temperatures and fields, $\mu_n g_I B_0 \ll kT$ (thermal energy). Hence, the nuclear qubit, using standard NMR to initialise[7] almost immediately fails DiVinenzo's 2nd criterion for a QIP proposal. Fortunately, this can be combated by producing a pseudo-pure initial state such that populations of all states except the ground state are equalised[8]. This can then be separated into two components to give a pure ground state and a component proportional to the Identity matrix which is unchanged under manipulation and thus can be ignored. Standard NMR is furthermore an ensemble technique acting on many nuclei, with measurement of the nuclear magnetic moment (i.e. a small magnetic field) and hence a number of moments are needed to create a field large enough to be detected. Thus, a readout sensitivity of 10^{14} spins is produced, far short of the single qubit detection required by DiVinenzo's 5th criterion. This rendered NMR QIP impossible until the advent of ensemble quantum computing in 1997 by Cory *et al.* [CFH97] and simultaneously Gershenfield and Chuang [GC97]. Ensemble QC makes use of the spins in individual molecules as independent quantum computers

[7] through cooling to a ground state $|0\rangle$ population.

[8] Ultimately, with a few exceptions this only allows the classical simulation of quantum algorithms.

with NMR addressing all spins simultaneously[9]. Readout is then of the ensemble average expectation value of the observable rather than the measurement of $|0\rangle$ or $|1\rangle$, though this is sufficient to perform most QC algorithms. NMR QC, having overcome these hurdles, ultimately fails at criterion 1, the scaling up of the qubit system being limited with current technology to a maximum number of around 10 qubits. This limit arises from the trade off in using a pseudo-pure initial state, whereby the effective qubit signal gets exponentially weaker with an increasing number of qubits in the system. Nevertheless, NMR has given the largest QC to date of 7 qubits and shown the successful implementation of Shor's algorithm, factorising 15 into 3 and 5 [VSB01].

EPR appears completely analogous to NMR except that it is acting on an unpaired electron spin rather than a nuclear spin. However, EPR crucially offers significant advantages over NMR as a result of the greater Zeeman energy splitting. The energy separation of the qubit states can be greater than the thermal energy ($\mu_n g_I B_0 \gg kT$) and so a pure initial state can be achieved resulting in no loss in sensitivity (in contrast to the pseudo-pure initial state). Furthermore, the larger magnetic moment of an electron compared to a proton gives a detection limit of 10^{10} spins. Overall this results in an achievable qubit system of approximately 23 qubits under standard experimental parameters and although significantly more than NMR QC will still fall short of the estimated 50-100 qubits to show real improvement over classical computing. The electron spin also suffers from much faster decoherence times compared to the nuclear spin, an essential element outlined in DiVincenzo's 3rd criterion, due to a stronger interaction with the environment. However, the gate times for EPR are in the order of ns, compared to that of NMR in the order of μs, and so with careful choice of the electron system, error correcting may be readily applicable (gate time $> 10^{-4} \times$ decoherence time) and much of the nuclear spin advantage is lost. The use of EPR (and NMR) for QIP is clearly limited as an ensemble technique but they can be applied to single spins with readout via another mechanism and hence have generated a plethora of spin proposals.

[9] i.e. a system of many molecule containing 10 nuclear spins will give a ten qubit QC.

1.3.2 Spin proposals

Spin proposals range in architecture and include electrons within quantum dots [LD98], ion traps [CZ95, Ste97], on molecules contained inside fullerenes [BAB06], in semiconductors [Kan98, BEL00], at diamond NV^- centres [JGP04b, Chi06] and even on the surface of liquid helium [Lyo06]. The following paragraphs will summarise some of these proposals, then two proposals, directly relevant to the experimental results of this thesis, will be explained and evaluated in more detail in Section 1.3.3 and Section 1.3.4.

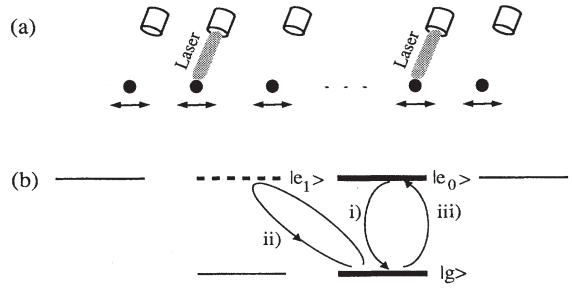

FIGURE 1.3: (a) Schematic of the ion trap proposal, the ions are confined in a linear trap and interact with different laser beams (b) Energy level diagram showing $|g\rangle$ and $|e\rangle$ qubit states with single qubit rotations (i) and (iii) and two qubit rotations (ii) where $|e\rangle_n$ refers to the nth ion in the trap. The laser interaction is used to control the qubit rotations and is tuned with the ion vibrational modes to produce a centre-of-mass quantised oscillator (and the states $|0\rangle_{cm}$ and $|1\rangle_{cm}$). Reprinted with permission from [CZ95]. Copyright 1995 by the American Physical Society.

The use of ion traps for QIP was proposed by Cirac and Zoller [CZ95] in 1995 and is now considered a relatively mature implementation. In this proposal, internal electronic states are used as the qubit but effectively the nuclear spin hyperfine states, $|\downarrow\rangle$ and $|\uparrow\rangle$, can also be used [MMK95]. The scheme uses a string of cold ions individually held by either electromagnetic (Penning) or radio frequency (Paul) traps. The qubit states, $|0\rangle$ and $|1\rangle$, are defined as the ground state $|g\rangle$ and a long-lived metastable excited state, often denoted $|e\rangle$. One-qubit gates can therefore be performed by addressing Raman transitions with resonant laser light. Readout of the system is via state selective fluorescence, for example a laser tuned to the transition between $|g\rangle$ and a short-lived

excited state, $|e'\rangle$ (not shown in the figure), will cause continual absorption and re-emission of the $|g\rangle$ state only. The application of a two qubit gate relies on the Coulomb repulsion between ions which results in a coupled vibrational mode of the string of ions. Light carries not only energy but also momentum and thus laser interaction with an ion results in an exchange of momentum and ion recoil. Subsequently, laser interaction tuned with the vibrational mode will result in coherent recoil of all ions (Mössbauer effect) and a centre-of-mass (cm) quantised oscillator. This gives rise to two quantum states of interest, the ground state $|0\rangle_{cm}$ and the first vibrational mode $|1\rangle_{cm}$, which can be used to induce interaction between the ions. An example would be an ion cooled to the $|0\rangle_{cm}$ state with a resonant laser pulse on the $|e\rangle \rightarrow |g\rangle$ transition also causing the $|0\rangle_{cm} \rightarrow |1\rangle_{cm}$ transformation. Hence, whilst the $|g\rangle|0\rangle_{cm}$ state is unchanged, $|e\rangle|0\rangle_{cm} \rightarrow -i|g\rangle|1\rangle_{cm}$ and information originally stored on a single ion is transferred to the collective mode of all ions. The ion system is highly isolated with long decoherence times and is potentially scalable. Current developments use an array of small ion trap registers arranged on a substrate using lithography rather than a single linear trap of ions, vastly simplifying manipulation difficulties. This type of scheme was proposed by Kielpinski [KMW02] and uses a 'quantum charge-coupled device' to confine and manipulate a few ions in a trap, whilst allowing others to move and communicate between traps. Steane [Ste07] produced a detailed proposal based on Kielpinski architecture for a 300 qubit system employing 13000 ions and 1000 laser beam pairs. This scheme is theoretically possible, with some efforts working towards scale up [BW08, HHJ09], but many factors still must be overcome and other problems such as the effect of ion heating have yet to be determined on this scale.

A diamond nitrogen-vacancy (NV^-) centre can be used for QIP [GOD06], comprising a substitutional nitrogen atom with an adjacent vacancy and associated electron spin. The centre has a long lived triplet state which can be used to address the physical qubit via the ground state (^{3}A) to first excited state (^{3}E) optical transition. Figure 1.4 shows how standard microwave manipulation can be used for the physical qubit, with optical polarisation and fluorescence of the ^{3}A m_S=0 state for initialisation and (single spin,

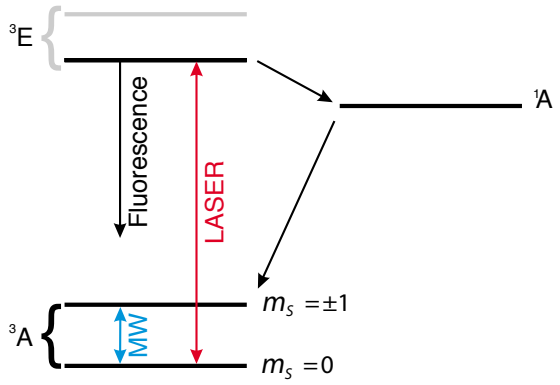

FIGURE 1.4: NV^- energy level structure. The grey line corresponds to the unused ^3E m_S=±1 sublevels. Reprinted with permission from [JGP04b]. Copyright 2004 by the American Physical Society.

single-shot) readout [JGP04b, NBS10]. The electron spin exhibits very long T_2 times of 350 μs at room temperature [GDP06] which have recently been improved using isotopically pure ^{12}C diamond containing no environmental nuclear spins to 1.2 ms [BNT09]. Thus, the NV^- centre has sparked much research in recent times but problems arise in coupling due to the limited control of implantation into diamond or growth by chemical vapour deposition (CVD). Two qubit coupling has been demonstrated using: the naturally abundant ^{13}C nuclear spin resource [JGP04a, DCJ07], which have also been entangled [NMR08]; N_2 implantation to give NV^--N pairs [GDP06] and impressively by neighbouring NV^- centres [NKN10]. However, realistically spin-light coupling, which has recently been shown [BFBA10], or 'flying' qubits may need to be employed for multiple qubit schemes [GOD06].

A quantum dot can contain a 3-D confined exciton (electron hole pair) within a semiconductor material where the exciton exhibits properties akin to a ^1H atom. The first quantum dot scheme was published in 1998 by Loss and DiVincenzo [LD98] and is based on exchange interaction within a double quantum dot. The qubit is given as the spin of the excess electron on a single-electron quantum dot and manipulation is as previously described with addressing via local magnetic fields or alternatively through an electric field. Two qubit manipulation occurs through electrical gating, controlling the tunnelling barrier between neighbouring quantum dots such that a high

voltage prevents tunnelling and a low voltage provides transient Heisenberg spin-spin coupling:

$$H_s(t) = J(t)\vec{S_1} \cdot \vec{S_2} \tag{1.2}$$

This will describe the coupling accurately only under certain conditions [LD98] and where $J(t)$ is the time-dependent exchange constant and $\vec{S_i}$ the Pauli spin operator for i. Readout can be through 'spin-valves' to another quantum dot, converting spin to a 'readable' charge or alternatively spin blockade phenomena could be harnessed [OATT02]. Other proposals make use of the exciton electric dipole coupling to address the physical spin qubits through optical Raman transitions and a single microcavity mode. Using these longer range interactions is perhaps more feasible for scale up and a 100 qubit scheme was suggested by Imamoğlu [IAB99] with details of one and two qubit gate implementation. However, within quantum dots the decoherence time is limited by interaction with the surrounding nuclear spins giving T_2 times on the order of μs, suitable for quantum error correction but shorter than many other qubit alternatives.

The principle material for quantum dot production is GaAs which contains many nuclear spins and has a short decoherence time of $\sim$10 ns [JPT05, PJT05]. This was improved by Johnson *et al.* [JPT05] by application of a mT magnetic field and further by Petta *et al.* [PJT05], using pulsed EPR to produce a T_2 exceeding 1 μs. Another solution to improve decoherence times would be to choose a material that has fewer nuclear spins. This was proposed by Friesen *et al.* [FRS03] where a SiGe alloy is used for confinement and electrons are contained in nuclear spin free ^{28}Si layer. Recent work has focused on this material with the observation of coherent spin phenomena [KSE07] and lifetime-enhanced spin blockade for readout [SST08]. However, silicon has a complex band structure and so practical implementation is difficult and results are hard to conclusively determine. A different approach is to take ^{28}Si and implant donor nuclear spins in the bulk system as the qubit, as described in one of the most significant QIP

schemes now known as the Kane proposal [Kan98].

1.3.3 Phosphorous doped silicon and the Kane proposal

^{31}P doped Si

Donor ^{31}P atoms in a silicon matrix provide a nuclear spin qubit and an associated Coulomb potential bound electron (qubit) at low temperatures. This allows the choice of an electron and/or nuclear spin qubit system integrated with the advances of existing silicon technology allowing preparation of highly pure defect-free samples. Natural silicon is 95.4% ^{28}Si (of no nuclear spin), with a 4.6% natural abundance of ^{29}Si, possessing a nuclear spin 1/2. This lack of environmental spins prevents decoherence from magnetic field fluctuations arising from nuclear spins [WdSDS05]. Donor electrons in silicon have a large energy splitting (around 10 meV) from the ground state to first excited state which reduces decoherence from spin-orbit coupling. The low abundance of environmental nuclear spins, low defects and small spin-orbit interaction gives rise to exceptionally long electron relaxation times ($T_{1e}\sim$1hr at 1.25 K)[10], identified as early as the 1950's by Feher and Gere [FG59]. The electron $T_{2\mathrm{e}}$ time is of greater importance for QIP and likewise was reported in the 1950's at a substantially lower 250 μs [GB58] at 1.4 K and 3×10^{16} donors cm^{-3}. This is a long $T_{2\mathrm{e}}$ time for an electron spin system but it can be improved further by using isotopically pure ^{28}Si containing no environmental nuclear spins. An isotopically pure ^{28}Si sample of a comparative concentration gives a $T_{2\mathrm{e}}$ of 520 μs [GB58] which can be improved using lower dopant levels to 2.8 ms at 1.2 K [TLAR03].

As discussed in Section 1.3 the nuclear spin relaxation times are generally much longer than those of the electron, with a $T_{1\mathrm{n}}$ of >10 hrs reported [FG59]. Theoretically an almost infinite (10^{18} s) $T_{2\mathrm{n}}$ time is predicted in very low doped systems at millikelvin temperatures [WS88] but experimentally this has not been verified due to the limit

[10]The subscript 'e' (in T_{1e}) refers to a property of the electron spin state and similarly 'n' the nuclear spin state.

of detection sensitivity. Using NMR, T_{2n} has been measured only at high doping levels (near the metal insulator transition) [HH86, AD87]. However, utilising EPR in Chapter 4 and Chapter 5, we shall presently investigate T_{2n} at low dopant levels.

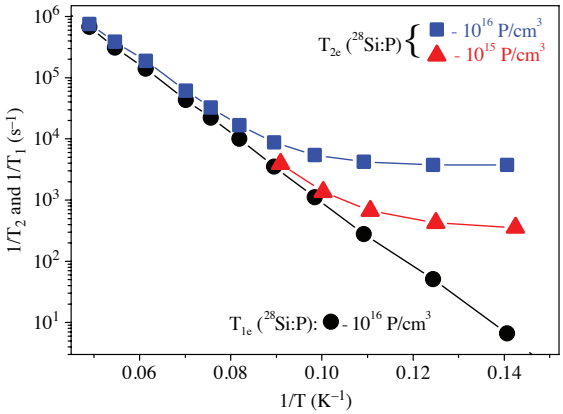

Figure 1.5: Temperature dependence of electron spin relaxation times in isotopically purified ^{28}Si:P. Reprinted with permission from [TMB06]. Copyright 2006 IOP.

Understanding the relaxation and decoherence mechanisms in phosphorus doped silicon is critical in producing samples to improve these parameters. The electron T_1 time has been found to be independent of doping concentration and falls exponentially with temperature (Figure 1.5 [TMB06]). The mechanism for T_1 is thus well established to be via an Orbach process (discussed in more detail in Section 6.2), with relaxation through resonant phonon transitions to an excited electronic state [Orb61]. Similarly, it is shown that T_{2e} at higher temperatures is also governed by this process. Figure 1.5 shows that T_{2e} at lower temperatures reaches a limiting value dependent on the ^{31}P concentration in the sample. The T_{2e} decoherence pathway is therefore attributed by Tyryshkin *et al.* to dipole-dipole interactions between donor electron spins. Thus, the effect ('instantaneous diffusion' [SDR81]) on a standard T_2 experiment can be exploited to give an optimised T_{2e} extrapolated for an isolated spin to ∼60 ms at 7 K [TLAR03], recently improved to ∼10 s at 1.8 K [TTM11].

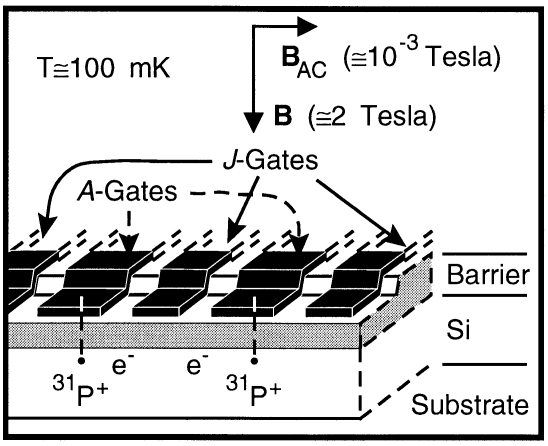

FIGURE 1.6: Schematic representation of the Kane proposal utilising ^{31}P donor nuclear spins with an associated electron in a Si host, separated by a barrier from metal gates on the surface. The 'A gates' allows individual addressing of the ^{31}P nuclei and 'J gates' mediate qubit-qubit interaction. Reprinted by permission from Macmillan Publishers Ltd: Nature [Kan98], copyright 1998.

The Kane proposal

The Kane proposal for a silicon based quantum computer [Kan98], has been highly influential and has motivated research in phosphorous doped silicon for quantum computing applications. The theoretical proposal is described in the beginning of this section and then progress in experimentally implementing the proposal or adaptations of the original scheme are discussed.

The Kane proposal utilises the extended electron wavefunction of shallow donors in a silicon crystal, which produce a ^{31}P hyperfine interaction proportional to the wavefunction probability density at the nucleus. This allows interaction of nuclear spins through the electron spin viz. electron-mediated or indirect nuclear spin coupling. Figure 1.6 shows a schematic of the proposal where typically the insulating barrier would be a SiO_2 layer. The hyperfine coupling can be controlled via application of a voltage on the A-gates such that a positive voltage will reduce the electron wavefunction probability density at a ^{31}P and hence the hyperfine interaction. This provides a hyperfine splitting (A) ranging from 50 $<$A$<$ 90 MHz and selective single qubit rotations through frequency matching with the oscillating magnetic (B_1 or B_{AC}) field (as in NMR). The

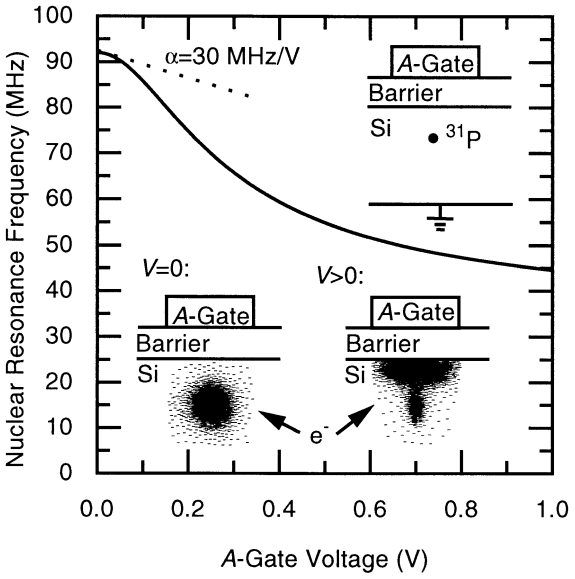

Figure 1.7: The 'A-gate' applies an electric field to pull the electron wavefunction away from the donor and towards the barrier, reducing the hyperfine interaction. This changes the resonance frequency of the ^{31}P nucleus so that it can be individually addressed. Reprinted by permission from Macmillan Publishers Ltd: Nature [Kan98], copyright 1998.

J-gate will facilitate two qubit operations through the electron-mediated coupling of the ^{31}P nuclei. The electron exchange energy, $4J$, is given by Equation (1.3) and is proportional to the electron wavefunction overlap for well separated donors.

$$4J(r) = 1.6\frac{e^2}{\varepsilon a_B}(\frac{r}{a_B})^{5/2}\exp(\frac{-2r}{a_B}) \tag{1.3}$$

J can therefore be controlled by applying a positive voltage on the J-gates inbetween donors to increase the overlap integral of the electron wavefunctions. In a magnetic field when $J < \mu_B B/2$, the system will remain in the ground state $|\downarrow\downarrow\rangle$ as shown in the Figure 1.8. Increasing the exchange interaction, the energy level diagram shows that the electron spin singlet $|\uparrow\downarrow\rangle - |\downarrow\uparrow\rangle$ level is lowered relative to the three triplet states. Furthermore, when in the $|\downarrow\downarrow\rangle$ state, using perturbation theory, the nuclear energy eigenstates $|10\rangle - |01\rangle$ are lowered in energy with respect to $|01\rangle + |10\rangle$ eigenstate, when the hyperfine interaction (A) of the two nuclear-electron systems is equal (Figure 1.8). Therefore, by modulating the J-gate voltage a controlled rotation between the nuclear

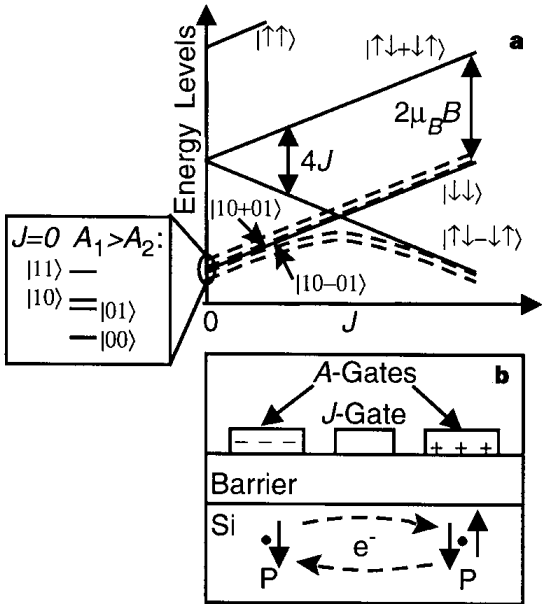

FIGURE 1.8: (a) Electron (solid lines) and lowest energy-coupled electron-nuclear (dashed lines) energy levels as a function of J (energy level of the $|\uparrow\uparrow\rangle$ state is cut in the figure). (b) Proposed readout of the $|\uparrow\downarrow\rangle - |\downarrow\uparrow\rangle$ state via production of a D^- state allowing charge motion between A-gates and a measurable capacitance. Reprinted by permission from Macmillan Publishers Ltd: Nature [Kan98], copyright 1998.

eigenstates can be achieved and a two qubit gate is shown. Using appropriate values, at low J, the nuclear spin exchange frequency, ν_J, gives the clock (processing) speed which is limited to a relatively long 75 kHz.

$$h\nu_J = 2A^2\left(\frac{1}{\mu_B B - 2J} - \frac{1}{\mu_B B}\right) \tag{1.4}$$

The proposal also produced a scheme for readout of the nuclear spin state via the electron spin state using a spin-resonance transistor (SRT). Measurement of the system is conducted with $J > \mu_B B/2$ such that the singlet $|\uparrow\downarrow\rangle - |\downarrow\uparrow\rangle$ state is lower in energy than the triplet $|\downarrow\downarrow\rangle$ state. At the crossing of these electron spin states they become coupled to the nuclei with the nuclear spin states $|10\rangle - |01\rangle$ and $|01\rangle + |10\rangle$ mapped onto the $|\downarrow\downarrow\rangle$ and $|\uparrow\downarrow\rangle - |\downarrow\uparrow\rangle$ electron spin states respectively. The $|\uparrow\downarrow\rangle - |\downarrow\uparrow\rangle$ spin state can then be read by binding both electrons to the same donor in a D^- state through biasing of adjacent A-gates. This produces charge motion between the ^{31}P

nuclei forming negatively charged defects and an increase in capacitance across the gates. A single-electron capacitance technique is proposed to measure this although implementation is yet to be experimentally achieved. The long decoherence times for this system have been previously mentioned, but the presence of fluctuations from the required gate voltage may limit these times. In particular voltage fluctuations of the A-gates will result in differences in the precession frequencies of adjacent spins and result in a shortened T_2 time. Material dependent fluctuations are also likely to have a large effect on the spin dephasing time arising, for example, from charge fluctuations between defect sites[11].

Some alternative Kane like schemes have also been proposed such as by Vrijen *et al.* [VYW00]. This scheme principally uses Si-Ge heterostructures rather than Si-P but is applicable to this material also. The paper introduces readout through a more practical field-effect transistor (FET or field-effect SRT) rather than the elegant but difficult to implement SRT in the original proposal. A FET measures spin by virtue of the Pauli exclusion principle, whereby a second electron will bind to a donor defect only if it is opposite in spin to the first electron. This gives a change in the electrical current across the FET which will measure a single spin if single charge sensitivity is achievable. The proposal also uses the electron spin qubit for processing rather than the nuclear spin, improving the clock speed from 75 kHz to around 1 GHz. This removes the need for transfer of information between nuclear and electron spin states but could still be implemented to form a quantum nuclear memory (see Section 1.5). Such an idea was suggested by Skinner *et al.* [SDK03] but using a 'hydrogenic' nuclear-electron spin pair with transfer, for example, to the electron spin to couple qubits via S-gates and electron shuttling.

Progress on the experimental implementation of the Kane proposal has been slow despite large investment in the area. The literature reveal modest steps towards achieving a functional silicon QC with work often divulging into related areas such as semiconductor quantum dots. One of the early breakthroughs was to achieve control over

[11] yet to be experimentally found.

^{31}P implantation using a precision STM technique [OSS01], adsorbing single phosphine (PH_3) molecules to produce the ∼20nm ^{31}P array required (or better). This technique has been improved using electron beam lithography (EBL) to further control placement [FRR07] and molecular beam epitaxy (MBE) to deposit a Si layer over the ^{31}P atoms in order to secure them [RPR07]. Alternatively, single ion implantation was demonstrated by ion bombardment and electrical detection of a successful event [DHJ03, JYH05]. Spatial control in this technique is achieved through masking and ion energy selection, to give the desired donor depth[12]. This led to a charge-based QC proposal [HDW04], similar to a double quantum dot charge based scheme [BDEJ95, FYV00], with a linear array of coupled ^{31}P and $^{31}P^+$ ions. Naturally, this led to work on Si:P double quantum dot systems with recent articles showing: gate-defined dots [AFDC07]; gate-controlled charge transfer [HFE08]; microwave assisted [PLF09] and lifetime enhanced [SKS10] transport; transistor charge state detection [MPC08, STR09] and spin relaxation times [STHL10, XHJ10, WSSW10].

Most quantum dot schemes use two dots capacitively coupled to quantum point contacts (QPC) for charge detection [EHWvB04] but there is growing research into extremely fast and sensitive radio frequency single electron transistors (rf-SET) [SWK98, LJP03, FHH04]. The advantage of these are that gate/readout times are in the order of ps [HDW04] and although using a charge qubit directly may not be feasible (fast decoherence), performing spin-charge conversion for readout is highly appropriate. Rf-SETs are directly applicable to the Kane proposal (two 'dots' not required) and the latest research has focused on these. Highlights include an aluminium rf-SET for single electron detection and transfer [ABW07] and a silicon rf-SET that allows easier integration but is not yet suitable for single electron charge detection[13] [AFDC08]. However, impressive recent experiments do report single-spin, single-shot sensitivity using a silicon-SET transistor with readout via spin-charge conversion based on spin-dependent tunnelling [MPZ10, MEH09].

[12]Control with this technique is currently not good enough for full QC scale up but is suitable for few qubit systems.

[13]sensitivity of $10\mu e/\sqrt{Hz}$ at megahertz bandwidth.

Another powerful new transistor is the silicon FinFET (3-D field effect transistor) reported by Lansbergen *et al.* [LRW08] which shows control over the degree of hybridisation of a single electron wavefunction, between the donor Coulomb well and a nearby interfacial well c.f. a J-gate. This hybridised system thus allows surface control of a quantum-confinement transition shown experimentally using As donors. A more traditional silicon metal-oxide-semiconductor field-effect transistor (MOSFET) has also been recently produced but using broadband electrically detected magnetic resonance (EDMR) readout [vB08]. EDMR is an alternative readout scheme measuring current variation due to a spin-dependent recombination of excess electrons and a Si/SiO_2 paramagnetic interface state (P_{b0}) in a magnetic field [BL03, HHG10]. ESR (see Section 1.3) is then used to induce Rabi oscillations from recombination to allow detection of coherent electron spin motion. Coherent Rabi oscillations have been shown by Stegner *et al.* [SBH06] who further suggested that through ^{31}P hyperfine coupling this could be used for recombination-based nuclear spin readout. Research by Huebl *et al.* [HHG08] has also used pulsed EDMR to give a spin echo and show an effective T_2 of 1.7 ± 0.2 μs, which has been improved to over 100 μs by Morley *et al.* [MMS08] and investigated in detail by Paik *et al.* [PLB10]. The present sensitivity using this technique is $\sim$100 electron spins [MHB06] and hence work must be done to achieve single spin detection. Progress has been been made in addressing single spins electrostatically to tune them in and out of resonance ('Stark' tuning), such as in the application of an A-gate. Application of an external electrical field pulls the electron wavefunction away from the donor nucleus to reduce the hyperfine coupling and field frequency. Recent work has shown the implementation of Stark shifts in ^{121}Sb [BTS06], ^{31}P [RWB07], for a single boron impurity [CWR07] and in SET devices [Mor10] in silicon. Also experiments on other similar donors in silicon such as bismuth have been conducted with the aim of utilising the larger (I=9/2) Hilbert space [MWS10, GWR10, MMM10]. Therefore, work on the implementation of the Kane proposal has in latter years shown good progress in individual areas, however putting components together in a fully functioning few qubit device has yet to be shown. This is likely to be problematic due to the associated component effects on the decoherence of the fragile qubit.

1.3.4 Endohedral fullerenes and fullerene based quantum computing

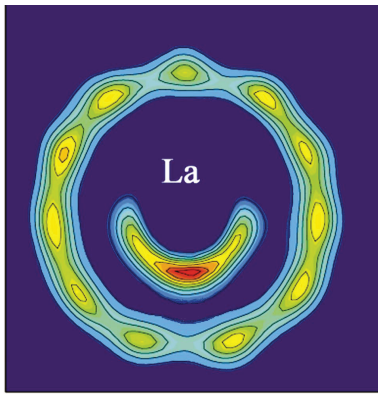

FIGURE 1.9: The maximum entropy method (MEM) charge density section showing the position of a La atom in a La@C_{82} molecule. The contour lines are drawn from 0 to 5 with a 0.5 $e/\mathring{A}^{-3}$ step. Reprinted with permission from [NIS04]. Copyright 2004 by the American Physical Society.

The use of endohedral fullerenes for QIP is less developed than proposals using phosphorous doped silicon, but offers significant promise. An endohedral fullerene comprises an atom or atoms encapsulated within a carbon cage, giving rise to a unique set of properties. The first example of such a molecule was discovered in 1985 by Heath *et al.* with a series of LaC_n^+ ion species identified using mass spectroscopy [HOZ85]. LaC_{60}^+ was further characterised by the lack of reactivity with reactive gases such as H_2, O_2, NO and NH_3 [WEO88] [CGJ91] but definitive characterisation by X-ray diffraction (XRD) was not achieved until 1995, using Y@C_{82}. Endohedral fullerenes are made using high-temperature laser vaporisation and DC arc-discharge methods[14] which vaporise carbon and atoms to be encapsulated to a plasma state[15]. On cooling from this state, amongst other products, the desired endohedral fullerenes are produced and isolated using high performance liquid chromatography (HPLC). Using these methods a range of atoms, predominately of group 2, 3 or a lanthanide e.g. Sc, Y, La, Ca, Sr, Ba and Ce−Lu, have been encapsulated in fullerenes such as C_{60}, C_{70}, C_{76}, C_{78}, C_{82} and

[14]Fullerenes are essentially soot so can be produced by any carbon burning but arc-discharge is the most popular for synthesise of larger amounts of material.

[15]Alternatively application of high temperature and pressure or atomic collisions can be used.

C_{84}. Most of these metallofullerenes incur charge transfer to give an unpaired electron 'qubit' on the cage which was thought to limit relaxation times ($T_2 < 1.5$ μs for La, Sc and Y@C_{82} [KGM98, OOS95]) but I have explored these properties in more detail within this thesis (Chapter 3). Alternatively, multiple atoms can be incorporated into a cage such as Er_2@C_{82} and the TNT (trimetallic nitride template) fullerenes composed of planar tri-lanthanide groups such as $ErSc_2$@C_{80}. These systems can result in little charge transfer to the cage with electron density remaining on the centred molecules which can be cooled to give an effective two level electronic structure viz. a qubit. Crucially, cage mediated state selective photoluminescence is observed in many of these metallofullerenes which could be used towards single spin detection, for example in $ErSc_2N$@C_{82} [MTD08]. Encapsulation of noble gases and group-V atoms also gives isolated systems with atoms centrally trapped by a harmonic like potential, of these only group-V species will be paramagnetic and of potential for spin based QIP.

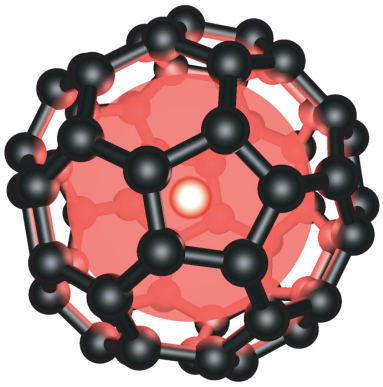

Figure 1.10: Pictorial representation of the N@C_{60} molecule. The red shading is illustrative of the electron spin wavefunction.

One of the most promising endohedral fullerenes for QIP is N@C_{60} which has been identified as having exceptionally long decoherence times for a molecular system [KDP97]. Originally produced in 1996 by Murphy *et al.* [AMPW96] it differs from many of the metallofullerenes as production is via C_{60} with encapsulation of atomic nitrogen through ion bombardment. Charge transfer from the nitrogen atom does not occur[16] and thus it acts as an isolated qubit within a carbon cage. This cage acts to protect the

[16] using the isotropic hyperfine coupling a 2% transfer is calculated [MTA05b].

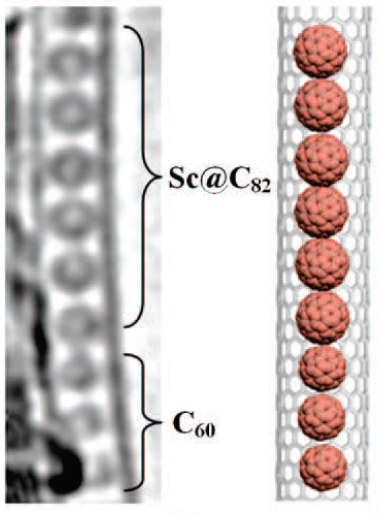

FIGURE 1.11: TEM and pictorial image of $Sc@C_{82}$ and C_{60} within a single walled carbon nanotube peapod, use of empty fullerenes could provide 'spacers' to control qubit-qubit interactions [WIZ08]. However, it has been shown that the metallofullerene hyperfine structure (hence qubit addressability) is lost, presumably due to charge transfer to the carbon nanotube, in such a structure [ZWI10]. Therefore, at present this approach appears less appealing. Reprinted with permission from [WIZ08]. Copyright 2008 by the American Chemical Society.

fragile qubit from environmental fluctuations which will otherwise cause the nitrogen spin to decohere. The high level of symmetry of the $N@C_{60}$ due to the carbon cage and a well centred nitrogen ion further prevents decoherence due to zero-field splitting (ZFS) commonly associated with high-spin systems. Thus the route for decoherence, like ^{31}P doped Si, has been found to be primarily due to an Orbach relaxation mechanism (in CS_2) [MTA06]. The Orbach process proceeds via two phonons resonant with a vibrational cage mode but with an energy difference producing system relaxation[17]. The T_2 time of $N@C_{60}$ in CS_2 (containing no environmental nuclear spins) was found to increase exponentially with decreasing temperature until 160 K, below which solvent freezing results in clustering and spin-spin relaxation. $N@C_{60}$ in CS_2 subsequently gave a T_1 of 0.5 ms and the longest T_2 recorded[18] for a molecular electron spin of 0.25 ms at 170 K [MTA06]. At lower temperatures the addition of S_2Cl_2 to $N@C_{60}$ in CS_2 is required to form a glass resulting in a T_2 below 20K that approaches 0.23 ms.

[17]The phonons are resonant on the transitions from the $|0\rangle$ and $|1\rangle$ states to an excited vibrational state and thus cause decoherence.

[18]until this thesis.

The long decoherence times of $N@C_{60}$ and/or the benefits of other endohedral fullerenes can be incorporated into larger structures to form QIP proposals. An interesting structure involves placing fullerenes within a carbon nanotube (CNT) to form a 'fullerene peapod' (Figure 1.11). This was discovered accidently by Smith *et al.* [SML99] in 1998 and occurs spontaneously under vacuum at 400-600 °C with up to 100% efficiency[19]. Fullerenes in the peapod act to alter the electronic states of the CNT and thus via nanotube-fullerene coupling this modulation could allow qubits to interact over distance [LKK02]. These interacting 'flying' qubits can be electrons which in nanotubes show 1-D ballistic transport with control through potential wells created by electrostatic gates or single injection and measured using a spin filter [BAB06]. Endohedral fullerenes can then be addressed through A-gates by applying a variable local magnetic field to change the resonant frequency in a similar manner to the Kane proposal. In a peapod scheme, separation for such gates can be conducted by functionalising the fullerene cages [BAB06], alternatively it has been proposed that fullerenes are placed on a surface with high precision [Har02]. The adjacent qubit interaction can then be addressed through magnetic dipolar coupling controlled through the direction of the magnetic field, Figure 1.12.

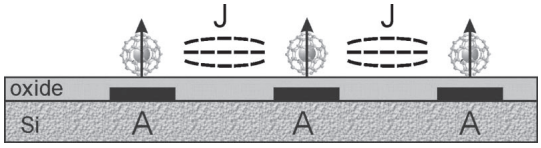

Figure 1.12: Schematic representation of a fullerene QC proposal by Harneit [Har02]. A-gates address single qubits and qubit-qubit interaction is mediated through magnetic dipolar coupling, controlled by the direction of the magnetic field (J-gate). Reprinted with permission from [Har02]. Copyright 2002 by the American Physical Society.

A different method is that of global addressing, originally proposed by Lloyd [Llo93] and refined by Benjamin [Ben01]; it allows pulses sent to an array to have a net effect on a single qubit. This requires an ABAB array of distinguishable qubits (extensively covered in [Twa03]) and thus is ideal for a peapod structure with, for example,

[19]This is the gas phase method, for thermally unstable materials such as $N@C_{60}$ a lower temperature solution phase method can be employed [SKR04] or a supercritical fluid filling processing [KBW04].

filling of dimer $^{14}N@C_{60}$ and $^{15}N@C_{60}$ pairs. It has been further shown that global control of all spins, with individual addressing of terminal spins only, is sufficient for QIP [Rau05, FT06, FXBJ07]. Hence global control appears a less demanding approach to produce a scaled quantum computer, discussed in Section 1.6. Fullerenes also offer many other theoretical proposals and have successfully been used to implement specific experiments, discussed in the context of 'gates' and 'memory' in the upcoming sections.

1.4 Gates and entanglement

The need for a universal set of quantum gates was identified in Section 1.2.2 and the ability to perform such gates for different spin schemes was addressed in Section 1.3. This section will evaluate gates in more detail and their implementation to date in spin systems, focusing on their use to perform entanglement, a key ingredient of a quantum computer.

1.4.1 Basic qubit gates

Table 1.1: Truth tables for classical 1-bit addition (AND and XOR gates), NAND and NOT gate

1-bit addition

A	B	C	T	Total
0	0	0	0	= 0
0	1	0	1	= 1
1	0	0	1	= 1
1	1	1	0	= 2

NAND gate

Input		Output
0	0	1
0	1	1
1	0	1
1	1	0

NOT gate

Input	Output
0	1
1	0

A classical computer works by implementing a series of classical gates in an algorithm to get the desired output from a particular input. A simple example of this is binary addition of two numbers (A and B) each consisting of just one bit. If both A and B are 1 then a 'carry' bit (C) must be created which can be achieved using an 'AND'

gate. The other remaining 1 states must be added up, but not when carried, to give the total (T), performed by an 'XOR' gate. The simple addition is shown in Table 1.1 constructed using the truth tables for the 'AND' and 'XOR' gates. If A and B consisted of two bits, addition of the second bit would then be required along with the carry bit (C) in a slightly more complicated circuit but using these same gates. The 'AND' and 'XOR' can actually be constructed by a single 'NAND' (NOT AND) gate which provides a universal set for classical computation [Tof80]. These gates can be seen in the truth tables of Table 1.1

Implementation of quantum gates is not so straightforward as now a qubit (q) is the input and another qubit (q′) the output. This corresponds to an input state, $|\psi\rangle = \alpha|0\rangle + \beta|1\rangle$, with the gate acting on the coefficients of output wavefunction to give $|\psi\rangle = \alpha'|0\rangle + \beta'|1\rangle$. Application of a NOT (X) gate (see Table 1.1 for classical truth table) will therefore swap the coefficients α and β. This is more clearly shown if the qubit is represented as a vector of length 2 and the NOT gate a 2x2 matrix acting on this vector in the basis $[|0\rangle, |1\rangle]$.[20] In terms of the Bloch sphere, using Equation (1.1), this can be seen as a 180 ° (π) rotation about the x axis. The physical implementation of this, within spin systems, has already been discussed by using resonant mw, rf or even optical pulses[21].

$$|\psi\rangle = \begin{pmatrix} \alpha \\ \beta \end{pmatrix} \qquad X = \begin{pmatrix} 0 & 1 \\ 1 & 0 \end{pmatrix} \qquad X.|\psi\rangle = \begin{pmatrix} \beta \\ \alpha \end{pmatrix} \tag{1.5}$$

This can give a rotation about any arbitrary in-plane angle (γ) by considering the function

X(γ)=cos(γ/2)$\mathbb{I}$+$i$sin(γ/2)X where $\mathbb{I}$ is the identity. To complete the single qubit set another gate is required to give a rotation about a different axis and example of such is a Z-gate (around the Z axis). Similarly this gives a 180 ° rotation but can be used

[20]This means the amplitudes of the basis states are given by the corresponding vector rows i.e. amplitude of $|0\rangle$ is α etc.

[21]Implementation of a c-NOT using mw/rf pulses actually introduces a phase, giving $-\alpha$ but this can subsequently be tracked and/or removed.

to give any angle rotation using $Z(\gamma)=\cos(\gamma/2)\mathbb{I}+i\sin(\gamma/2)Z$

$$Z = \begin{pmatrix} 1 & 0 \\ 0 & -1 \end{pmatrix} \qquad \mathbb{I} = \begin{pmatrix} 1 & 0 \\ 0 & 1 \end{pmatrix} \tag{1.6}$$

1.4.2 Two qubit gates and entanglement

Entanglement was famously described by Einstein as 'spooky action at distance' and although he thought it would prove to be a mathematical error, it is now accepted a fundamental element of quantum computing. Two systems (A and B) are entangled if they cannot each be completely described on their own. In other words, if mathematically A and B cannot be separated, then $|\psi_{Total}\rangle \neq |\psi_A\rangle\,|\psi_B\rangle$. In order to access the full Hilbert space that effectively gives QC its power over classical computing, entangled states are required, as shown by Jozsa [Joz98]. Entanglement has further been shown to be necessary for all pure state quantum algorithms to achieve significant improvement over classical computing [Joz03][22]. The maximally entangled states of a spin 1/2 system are given by the Bell pairs in Equation (1.7)

$$\Psi^{\pm} = \frac{1}{\sqrt{2}}(|\uparrow\downarrow\rangle \pm |\downarrow\uparrow\rangle) \qquad \Phi^{\pm} = \frac{1}{\sqrt{2}}(|\uparrow\uparrow\rangle \pm |\downarrow\downarrow\rangle) \tag{1.7}$$

Therefore, one of the main applications of a two qubit gate is to produce entanglement between qubits. This can be achieved using a controlled-NOT (c-NOT) gate shown in Table 1.2 which flips the target qubit (B) only if the control qubit (A) is in the state $|1\rangle$.

Application of the c-NOT to produce pseudo-entanglement between electron and nuclear spin states was shown for a CH radical spin 1/2 system (see Figure 1.13) by Mehring [MMS03]. To produce a particular Bell state a selective NMR $\pi/2$ pulse is applied to the $|1\rangle \rightarrow |3\rangle$ transition ($||\downarrow\uparrow\rangle\rangle \rightarrow \frac{1}{\sqrt{2}}(|\downarrow\uparrow\rangle + |\downarrow\downarrow\rangle)$) followed by a selective

[22]This covers all the 'main' algorithms, mixed states do not require entanglement (but are not preferable) and other algorithms that do not use entanglement such as that shown by Lloyd [Llo99] are more akin to classical computing.

Table 1.2: Truth tables for classical c-NOT and SWAP gates.

c-NOT gate

A	B	A'	B'
0	0	0	0
0	1	0	1
1	0	1	1
1	1	1	0

SWAP gate

A	B	A'	B'
0	0	0	0
0	1	1	0
1	0	0	1
1	1	1	1

EPR π pulse on the $|3\rangle \rightarrow |4\rangle$ transition to produce the -Ψ^- state with EPR readout. This has been further applied to a $^{15}N@C_{60}$ with a ^{15}N electron spin 3/2, nuclear spin 1/2 system to produce a pseudoentangled spin state [MSW04, SM08]. The pseudoentangled state arises as the experiment was conducted at 50 K and hence a pure initial state cannot be reached (see Section 1.3.1). The experiment proceeds as in the spin 1/2 system but the eight level system will allow up to 24 entangled states of a similar form to those in Equation (1.7). Alternatively, the eight levels can be considered as a 3 qubit system and thus 12 entangled states of the Bell state form can be produced. However, the entangled states are not long lived with a decoherence time of 208 ± 10 ns.

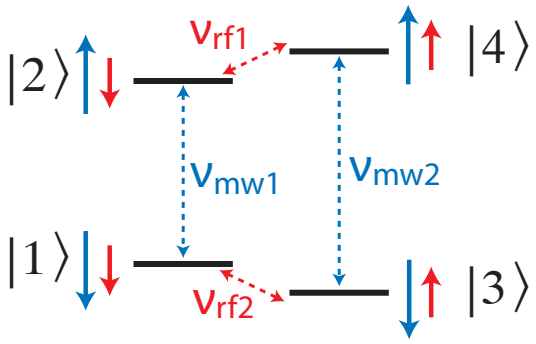

Figure 1.13: Spin 1/2 level system, the red arrow represents the nuclear spin and the blue arrow the larger magnetic moment of the electron spin.

A harder c-NOT to implement[23] is that between same spin systems, e.g. two electrons or two nuclei, but is an established technique for nuclei using ensemble NMR (and

[23]Coupling between same spins is generally less well defined and harder to control.

equally applicable to ensemble EPR).

$$c - NOT(A;B) = [(-\pi/2)B_y][(-\pi/2)A_z + (-\pi/2)B_z][(\pi)A_zB_z][(\pi/2)B_y] \quad (1.8)$$

The pulse sequence follows Equation (1.8), written by convention in reverse pulse order, where (A;B) refers to a 'A controlling B' i.e. A is the control spin and B the target spin [LBKF99].

The $[(\pi/2)B_y]$ therefore rotates the B spin (about y) into the x,y plane, whereby it precesses freely under the magnetic field and influence of the A spin. The free precession of B is dependent on the spin of A via the J-coupling, such that the Larmor frequency will increase when the A spin is 'up' and decrease when the A spin is 'down'. The precession time $[(\pi)A_zB_z]$, or τ=1/2J, results in a π phase shift, around the z axis, which is effectively forwarded by $\pi/2$ if the spin is up or retrograded by $\pi/2$ if the spin is down. The $[(-\pi/2)A_z + (-\pi/2)B_z]$ in the sequence refers to a change in the rotating frame and does not require additional pulses. The final $[(-\pi/2)B_y]$ subsequently rotates the B spin into the $\pm$z direction giving $|1\rangle$ or $|0\rangle$ dependent on the state of spin A. Hence, spins A and B are now in an entangled state and a c-NOT has been shown, though implementation for single spins is more difficult, recent experiments have shown this for two separate NV^- centres [NKN10]. The c-NOT has further been shown for quantum dots (optical scheme) [LWS03], ion traps [SKHR03], phonons [OPW03] and superconducting flux [PdGHM07]. In spin systems, recent work has focused on producing schemes for robust c-NOT gates to tolerate the error in qubit coupling [THWH07]. The c-NOT sequence can also be applied to higher spin systems with the $N@C_{60}$ electron spin 3/2 system discussed in more detail by Feng and Twamley [FT04].

In NMR, the J-coupling can be controlled by using the refocusing technique to effectively turn the coupling on and off. Refocusing works by applying a π pulse after a precession τ such that τ later the spin will come back into phase but with a π phase shift. Applying another π pulse then removes the effect of the J-coupling and hence

it appears 'off'. Addressing the coupling of two individual qubits is more difficult and many proposals rely on the J-gate architecture as described in the Kane proposal (see Section 1.3.3). Alternatively, it has been suggested by Suter and Kim [SL02a] that the coupling can be turned off by using a SWAP gate (see Table 1.2) to move the qubit between electron and nuclear states. The coupling between nuclear spins is six orders of magnitude smaller than between electron spins so will effectively be turned off when SWAPing electron and nuclear states (order of few hertz at 1 nm qubit separation). The SWAP in the spirit of a 'universal' gating system can be implemented using 3 c-NOT gates and is similarly well established in NMR [LBKF99]. This sequence however requires ideal, 'hard', pulses that are experimentally difficult to implement and therefore a better scheme uses selective pulses and is described in Equation (1.9) [SL02a] using the energy level diagram in Figure 1.13.

$$SWAP(S;I) = [(\pi)S_y^{(12)}][(\pi)I_x^{(13)}][(-\pi)S_y^{(12)}][(-\pi/4)I_z + (-\pi/4)S_z], \tag{1.9}$$

where $S_y^{(12)}$ refers to rotation about around the y axis of the $|1\rangle \leftrightarrow |2\rangle$ transition and rotations about the z axis can be implemented by composite pulses or as a phase shift. In ensemble NMR, Boulant *et al.* [BFP02] showed the implementation of the SWAP gate to move an entangled state state between two different ^{13}C nuclei pairs. However, the Suter and Kim [SL02a] scheme requires individual addressing of the qubit states which could be implemented using magnetic field gradients generated through micropatterend wires, see Figure 1.14. This would produce different Zeeman splittings and hence resonant frequencies, which can be selectively addressed (similar to Goldman *et al.* [GLYY00]). Therefore, to conduct a c-NOT gate the scheme first applies a SWAP gate to move the qubit from the nuclear spin to the electron spin state, the coupling is then 'on' and the c-NOT can be implemented. The qubit is then SWAPed back to the nuclear spin subspace where the coupling remains off such that the qubit can be stored. The scheme is actually much more powerful than this as it can utilise the benefits of the electron spin manipulation times and SWAP to the nuclear spin for a quantum nuclear memory as discussed in Section 1.5 and experimentally in Chapter 4

and Chapter 5.

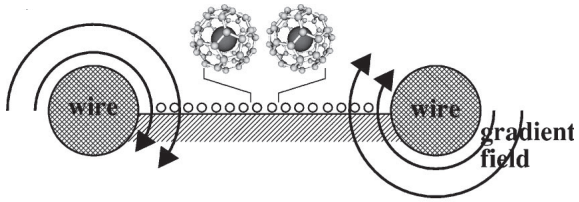

FIGURE 1.14: Arrangement of wires to give a magnetic field gradient such that the fullerenes on a silicon surface can be individually addressed. The current in the wires is equal and parallel. Reprinted with permission from [SL02a]. Copyright 2002 by the American Physical Society.

1.5 Quantum memories

In Chapter 1.2.2 the need for a long decoherence time was identified as a key requirement for a suitable qubit candidate. However, finding a suitable system that has a long decoherence time without compromising the other criteria is difficult. A simple approach is therefore to employ a quantum memory whereby the benefits of a 'processing' qubit can be exploited with transfer to a long decoherence 'storage' qubit for a memory. The Kane proposal [Kan98], covered in Chapter 1.3, is a powerful example of this, where the electron spin properties of fast manipulation, initialisation and achievable readout are utilised as the 'processing' qubit, and the longer decoherence time of the nuclear 'storage' qubit is used as a quantum nuclear memory[24]. The transfer of quantum information differs to that of classical information as the no-cloning theorem prevents copying across different degrees of freedom and thus transfer must take place directly [WZ82]. This has therefore limited the number of experimental examples of a quantum memory, some of which will be discussed below.

Similar to the Kane proposal, Dutt *et al.* [DCJ07] uses the long decoherence time of a ^{13}C nuclear qubit coupled with the processing ability of electron spin associated with a nitrogen vacancy (NV^-) centre. Initially the system must be polarised to the $|0,\downarrow\rangle$

[24]The original proposal actually uses slow nuclear spin gates for manipulation.

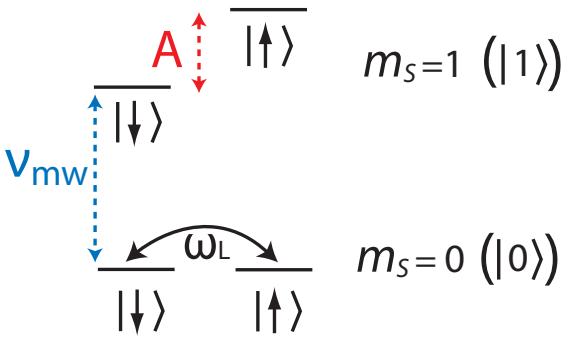

Figure 1.15: NV^- level structure with a nearby ^{13}C atom showing hyperfine splitting (A) of the ^3A $m_S = 1$ state ($|1\rangle$) but not the $m_S = 0$ ($|0\rangle$) state. Applying a weak magnetic field perpendicular to the nuclear spin quantisation axis, the nuclear spin precesses at the Larmor frequency (ω_L) when in the $m_S = 1$ state but not in the $m_S = 0$ state. Utilising this and selectively driving the mw addressable levels shown, a swap (mapping) operation can be performed. From [DCJ07]. Reprinted with permission from AAAS.

state in Figure 1.15 via optical initialisation of the NV^- centre. An arbitrary qubit can then be created in the electron spin state using microwave manipulation in one of the bases $X_\pm = (1/\sqrt{2})(|0\rangle \pm |1\rangle), Y_\pm = (1/\sqrt{2})(|0\rangle \pm i\,|1\rangle)$ or $Z_{0,1} = (|0\rangle, |1\rangle)$. The qubit can then be transferred to the nuclear spin state using a mapping function, held for a period of time before transfer back through an inverse of the mapping function. The information can finally be measured with the electron spin, using state-selective fluorescence and gives an experimental transfer fidelity of 75%. The time in which the qubit can be faithfully stored is governed by the nuclear T_2 and in this system is shown to be above 20 ms, far greater than that of the electron. The nuclear spin state has also been shown (unlike the electron spin) to decohere slowly under optical excitation which is required for entangling protocol (see 'brokering' Section 1.6). The NV^- proposal also has the advantage that the ^{13}C atoms will be subject to differing hyperfine interactions from the NV^- centres and hence via differing Larmor frequencies be individually addressable. However, present control of the system is poor as it relies on finding NV^- centres proximal to the naturally abundant ^{13}C atoms and hence cannot readily be scaled up to multiple qubit devices.

A different approach to a quantum memory is to encode logical qubits into a part of the Hilbert space that is not affected by environmental decoherence [PSE96]. This

has been demonstrated by Kielpinski *et al.* [KMR01] by transferring information from one r.f trapped $^9Be^+$ ion to another in a decoherence free subspace (DFS). The qubit is represented by two hyperfine states of the ion denoted $|\downarrow\rangle$ and $|\uparrow\rangle$ with detection via fluorescence of the $|\downarrow\rangle$ only. One ion is then used as the 'processing' qubit and is encoded through Raman driven rotations onto the DFS qubit for storage. The DFS is given by a superposition of $|\gamma_-\rangle = (1/\sqrt{2})(|\downarrow\uparrow\rangle - i\,|\uparrow\downarrow\rangle)$ and $|\gamma_+\rangle = (1/\sqrt{2})(|\downarrow\uparrow\rangle - i\,|\uparrow\downarrow\rangle)$ which is invariant under collective dephasing, $|\uparrow\rangle \rightarrow \exp i\zeta\,|\uparrow\rangle$. The experimental data indeed shows that the DFS state appears to have no collective dephasing and a ten fold improvement in dephasing under applied noise compared to a coherent test state. The DFS further shows improved storage time under ambient conditions indicating collective dephasing is the limiting factor. The same system has been improved upon by Langer *et al.* [LOJ05] to give a decoherence time almost 5 orders of magnitude longer than that of the original work. Langer *et al.* uses the DFS Bell states $|\Psi_\pm\rangle$ (see Section 1.4.2) showing a lifetime of 7.3 ± 1.6 s with an error probability of 1.4×10^{-5} for a detection duration of 200 μs (assuming exponential decay). This time is limited by magnetic-field fluctuations and hence could be improved upon[25] using field independent qubits [RLR04], with more recent work showing a universal set of quantum gates in the DFS [MKV09]. The use of DFS has also been shown experimentally for two entangled photons [KBAW00] and four entangled photons which, unlike the two photon system, allows protection of any arbitrary qubit under collective noise [BEG04]. This work reports good immunity to noise with states in a DFS showing error rates[26] typically only 1.5-2% higher under noise. More recently state independent encoding has been shown [TY08] which allows multiphonon entanglement [RidZB09]. In NMR, a logical qubit has been encoded within 3 nuclear spins [VFP01] to give a noiseless subsystem (NS) and a two-logic qubit within four physical qubits to give a DFS [OLK03]. A two-logic qubit DFS has also been constructed using four multiple quantum coherences from the four protons within a CH_3 spin system [WLS05]. This scheme reportedly protects against more types of decoherence than that produced by Ollerenshaw *et*

[25] but is exceptionally long compared to most other systems.

[26] Quantum bit error rate, false events over total events over 4 hours.

al. [OLK03] by virtue of a smaller nuclear spin system. Recent work has looked at the theoretical [TPK07, Bro07] use of DFS states for one-way quantum computation (covered in Chapter 1.6) and has been experimentally shown by Prevedel [PTS07]. This paper used a four photon system to encode a two qubit 'cluster' state into a DFS that is invariant to phase-damping noise and can be used for one-way QC. In contrast, the theoretical paper Brooke [Bro07] is more applicable to spin systems, showing how a DFS could be implemented for an array of dipole-coupled qubits (such as NV^- centres).

In proposals more suitable to quantum communication applications, an atomic quantum memory for a quantum state of light has been shown [JSC04]. This was achieved by interaction of the input pulse and an entangling field with spin-polarised caesium atoms, measuring the light qubit and mapping this onto the atoms using an r.f pulse. This transfer was conducted with a fidelity of 70% to give a quantum memory time of up to 4 ms but only works one way. A similar approach by Chanelire *et al.* [CMJ05] showed storage, transmission and retrieval of a qubit in a cold atomic ensemble. Propagation occurs through a single photon excitation to another remote atomic memory node where it is again stored and can be retrieved as a photon for readout. This forms the basis of quantum network and gave storage times exceeding 10 ms by intensity cross-correlation measurements. More recently this work has led to an entangled quantum memory of two atomic ensembles created by coherent mapping of an entangled state of light [CDLK08]. The efficiency in creating this state is low at 17% and the memory time only 8μs, but it is the first example of the creation of this important resource. This work has been extended to hybrid schemes utilising the solid-state light interface [DRAS08] which has shown entanglement between a phonon and NV^- centre [TCT10]. A very different hybrid scheme has also been subject to recent attention, coupling superconducting qubits and molecular qubits [RDD06, SSG10, SFD10, SBC11] with experimental process showing cavity-spin ensemble coupling [CGB10, KOB10, SSG10]. This is significant given the work to store multiple microwave excitations in a spin ensemble [WGW10], which given the results of this thesis, could lead to a robust multimode nuclear memory.

A less developed scheme involves an ion trap proposal using the 'hyperfine' ground state for a memory qubit and an 'optical' processing qubit. It is therefore similar to that of the NV^- centre but experimentally, although an extrapolated memory time of 6 s has been shown, the swap process has not [BKRB08]. Similarly, a theoretical paper by Witzel and Sarma [WHS07] proposes the use of a quantum nuclear memory in semiconductor nanostructures, similar to the Kane proposal. They theoretically show a T_2 for ^{31}P in natural Si of 9.7 ms and discuss routes to improve this such as the use of isotopically pure ^{28}Si. Furthermore, various theoretical papers exploit the electron and nuclear spin properties in molecular spin qubits such as $N@C_{60}$ [SL02a, Har02, HMW02, JSD07, YXW10, BAB06] as discussed in the previous chapters. These not only use the nuclear spin as a memory but employ the transfer of states to effectively turn on and off inter-qubit coupling (reduce the electron-electron dipolar coupling term to the nuclear -nuclear spin coupling constant). Significantly this thesis will show the experimental implementation of the these theoretical proposals in both Si:P and $^{15}N@C_{60}$, transferring qubit states between electron and nuclear degrees of freedom and recording the nuclear T_2.

1.6 The future of spin based QIP

Discussing the future of spin based QIP one can refer to the proposals evaluated in Section 1.3 with respect to DiVincenzo's criteria.

DiVincenzo's 5th criterion required single spin detection and clearly this has been a major experimental difficulty. A candidate solution is optically detected magnetic resonance (ODMR) where state selective luminescence is observed in a magnetic field. This optical readout has been successfully implemented for single spins using the NV^- centre [JGP04b] and could be applied to cage mediated photoluminescence in $ErSc_2N@C_{82}$ [MTD08]. This could also be applied to other systems by coupling the physical qubit to an alternative optically active qubit. Spin to charge conversion for electrical detected of single spin states appears a very good candidate for

semiconductor schemes, as described in Section 1.3.3. Detection of single electron charges and thus spins has been shown using rf-SETs [FHH04], Si-SETs [MPZ10] and QPCs [EHWvB04], with the latter two doing so with single shot detection. Single shot quantum non-demolition measurements of single nuclear spins have further been reported by Neumann *et al.* [SYSW08, NBS10]. In contrast, EDMR has shown coherent spin oscillations but readout is currently limited to ∼100 spins [MHB06]. EDMR is not confined to semiconductor systems and has been shown for C_{60} [HBS07]; but without good understanding of the mechanism, implementing this with, for example, $N@C_{60}$ may be problematic or even unfeasible. Alternatively, Nano-SQUIDS (superconducting quantum interference devices) can be used and have a sensitivity of around 40 electron spins per root Hertz [GJFD02]. The latest devices may be able to achieve single spin detection but are yet to show this experimentally [CWB06, GPMP10]. This measurement may proceed via a scanning tunnelling microscope (STM) tip, which can also be used in STM assisted EPR. This allows detection of a single spin precessing at the Larmor frequency (due to a magnetic field) via a rf modulation of the tunnelling current [DW02, Dur04] but not state measurement. In a different approach, the magnetic field associated with an electron spin in an NV^- centre has been utilised, but again single spin detection has yet to be achieved [MSH08]. However, magnetic resonance force microscopy (MRFM) has produced direct detection of an individual spin in silicon dioxide. This was achieved by measuring the force exerted by a resonant spin on a sensitive flexible cobalt cantilever but has the disadvantage of being a relatively slow technique [RBMC04].

The review has focused predominately on systems that are controlled in a similar fashion to a classical computer, i.e. using individually addressed gates. However, simpler and more elegant solutions for QIP have been proposed in 'global control' that was noted to be of promise in fullerene systems [BAB06] and relaxes the qubit-qubit control DiVincenzo originally required. Global control was originally suggested by Lloyd [Llo93] for an ABCABC series of 3 globally addressable qubits and was later improved to an ABAB array by Benjamin [Ben01]. The scheme does not require the

switching 'on and off' of qubit-qubit interactions needed to implement gates such as the SWAP or c-NOT. Instead all AB or BA interactions are addressed globally and hence this does not require demanding fabrication, minimum qubit separation or provide decoherence routes associated with gated devices. Global control has been further improved by Raussendorf [Rau05] and Fitzsimons *et al.* [FT06], whom show that not only can qubit-qubit interactions be left on but that only the terminal spins of a spin chain must be individually addressed. This uses a 'mirror-inversion chain' of identical spins which delocalise but later revive at a complementary site at the opposite chain end. The unique environment of terminal spin is then exploited, experimentally shown for a three-spins in a ^{13}C-labeled alanine system, using ensemble NMR [FXBJ07]. The qubits in such a mirror inversion also typically gain some entangling phase, which could be used towards 'one-way computation' [CAJ05].

A very different form of computation was proposed by Raussendorf and Briegel [RB01] in 'one way computation' which is not circuit based. Instead, entangled qubits in a 'cluster' or 'graph' state are utilised to perform an algorithm in an irreversible, 'one-way', manner. The scheme only relies on one-qubit measurement of the graph state resource and has been shown to be universal [RBB03]. The entanglement is destroyed after measurement and hence the scheme proposed recycling of the qubits, to produce a new entangled resource. The first experimental implementation of this computation was achieved by Walther *et al.* [WRR05] using four-qubit cluster state encoded into the photon polarisation and used to perform Grover's algorithm. An advantage of 'one-way' computation is that the generation of entangled states, which is not 100% efficient, can be separated from the processing. Thus, a 'brokering' scheme as described by Benjamin *et al.* [BBFM06] can be employed which uses 'broker' qubits to generate cluster states (can be applied many times) and then transfers to the 'client' qubit for measurement. This is similar to the quantum memory (Section 1.5) with the 'broker' qubit chosen to produce entanglement and the 'client' utilised to give a cluster state with a long decoherence time i.e. a 'memory' qubit. Entanglement and transfer between states can therefore be achieved through use of c-NOT and SWAP gates as

described in Section 1.4 with an electron and nuclear spin as an ideal 'broker' and 'client' respectively. This could be implemented in an NV^- centre system (Section 1.3) using the ^{13}C resource as described by Dutt [DCJ07] and SWAPing back to the electron spin for readout. The 'brokering' scheme is therefore another powerful example of the benefit in transferring information between different resources and the implementation of a quantum memory.

The key criteria to build a quantum computer as outlined in Section 1.2.2 have been evaluated. Progress has been made in producing techniques for single spin detection and the implementation of gates for single and two qubit operations. Using schemes such as global control or one-way computation would certainly make it easier to overcome experimental difficulties, such as those given by qubit-qubit interaction. However, the qubit must still have a long enough decoherence time to perform computation and without relying on extensive error correction, few systems can show this. A crucial experimental area will therefore be the transfer of information to states of longer decoherence times and the implementation of a quantum nuclear memory. Finally, any proposal must be scaled up for a functional QC but little experimental progress has been made to achieve this to date.

2

Introduction to Electron Paramagnetic Resonance (EPR)

Electron paramagnetic resonance is a powerful tool which can be used to give controlled manipulation of the electron spin qubit on the Bloch sphere that was illustrated in Section 1.2.1. A simplified picture was presented in Section 1.3.1 but as EPR forms the primary technique employed in this thesis a more detailed description is now shown. However, for a comprehensive account the reader is directed to the book "Principles of pulsed paramagnetic resonance" by Schweiger and Jeschke [SJ01a]

2.1 Continuous Wave (CW) EPR

The basic principles of EPR can be considered with respect to CW EPR which is primarily employed as a spectroscopic technique and is specifically used in Section 3.2.1. In EPR the magnetic moment (μ) associated with an unpaired spin will align parallel (spin up, $m_s = -1/2$) or anti-parallel (spin down, $m_s = +1/2$) to an applied magnetic field (B_0). In continuous wave (CW) EPR the absorption of the energy resonant with the Zeeman splitting ($g_e \mu_B B_0$, where g_e is the electron g-factor and μ_B is the Bohr magneton) can be detected and thus is used to identify the particular species via g_e. To gain further structural information the interactions of unpaired electrons with other species such a nuclei are considered. The local magnetic field associated with the nuclear spin adds or subtracts to B_0, splitting the resonant absorption points by the hyperfine constant, A. In experimental CW EPR an ensemble of spins is typically placed in a cavity to amplify the reflected signal that is detected[1] whilst sweeping the magnetic field and keeping the mw frequency constant.

2.2 Pulsed EPR

In pulsed EPR, the absorption of energy is not detected but instead the magnetisation given by the vector sum of the magnetic moments. In the applied field, B_0, a torque will act on the magnetic moments such that they will precess according to $\omega_L = g_e \mu_B B_0 / \hbar$, where ω_L is the Larmor frequency and $\hbar$ the reduced Planck's constant. To manipulate the system we apply a time dependent circularly polarised microwave field B_1 of frequency ω_{mw}, perpendicular to the static field B_0 and then move to a rotating frame in order to more easily understand the dynamics. The rotating frame is set to rotate at a frequency ω_{mw} such that when the microwave field is on resonance and $\omega_L = \omega_{mw}$, in the rotating frame the magnetisation will appear stationary. Subsequently, the interaction of the mw field with the magnetisation will act to precess the system

[1] absorption can be directly detected or detection can proceed via the reflected signal, the latter of which is more common in the modern EPR spectrometers used in this thesis.

according to $\omega_1 = g_e\beta_e B_1/\hbar$, with the sinusoidal variation in z-magnetisation known as a Rabi oscillation. In EPR experiments the microwave field is typically linearly polarised rather than circularly, this gives rise to components of twice the resonant frequency which can be neglected in what is known as the rotating wave approximation. The linear polarised microwaves allow control of the axis of rotation due to a phase component (ϕ) which in the rotating frame gives $B_{1,x} = B_1\cos\phi$ and $B_{1,y} = B_1\sin\phi$, where the subscript indicates the axis of rotation. If the phase is set for rotation around the x-axis a selective microwave π pulse or half a Rabi period will rotate the spin from spin up to spin down. Therefore given the phase, duration and power any arbitrary rotation about the x-y plane can be achieved according to $\theta = \mu_B g_e B_1 t_p/\hbar$ where θ is the angle of rotation and t_p the pulse length.

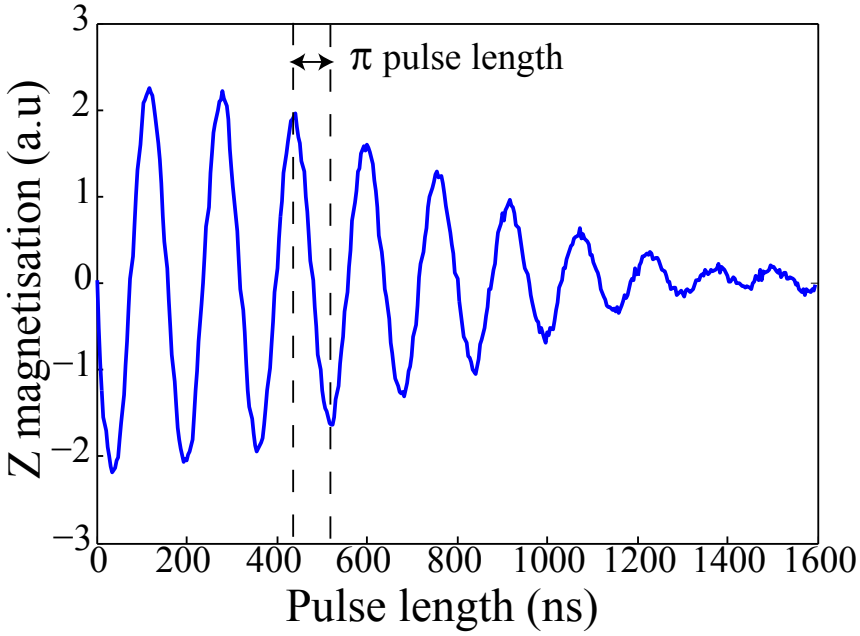

Figure 2.1: A Rabi oscillation for Si:P with a period of 160 ns (using Hahn echo readout), the length of the mw pulse is increased to show the manipulation of the Z-magnetisation. A π pulse is shown equivalent to a pulse length of 80 ns. The decay in the magnetisation is due to the dephasing of the electron spin echo, see Section 2.2.2.

2.2.1 Detection, free induction decay and the echo

To understand the detection of the magnetisation we must move back to a laboratory frame. In the laboratory frame the magnetisation is rotating around the z-axis at the Larmor frequency, ω_L, which will act as a generator to induce microwave signals. Quadrature detection of the x and y components can then be conducted by mixing with a phase shifted reference microwave source, ω_{mw}, to give $\Delta\omega$=ω_L- ω_{mw} where $\Delta\omega$ is the resonance offset frequency. The offset frequency arises as not all spins are on resonance at the the same time. In the rotating frame this will cause the static magnetisation vector to 'fan out' as the individual frequency components precess slightly faster or slower than ω_L. This signal is known as the free induction decay (FID) which is maximised in the x-y plane and is illustrated in Figure 2.2 (c). In EPR we find that it is often convenient to detect an 'echo' which consists of two FIDs back to back. Detecting an echo eliminates the signal loss due to the spectrometer dead time[2] and consists of a transverse mw π pulse which refocuses the FID signal (see Figure 2.2 (d)).

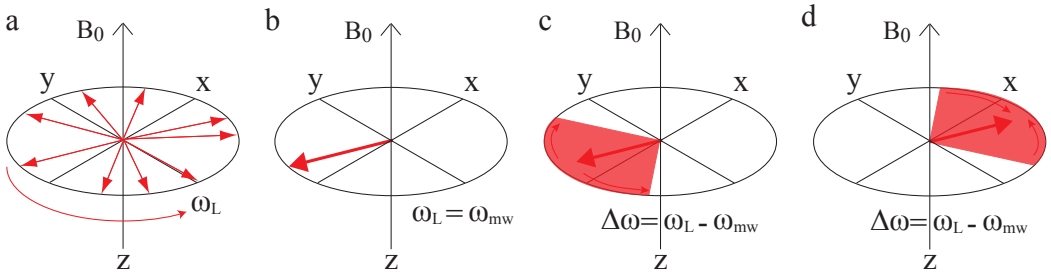

FIGURE 2.2: Graphical representation of the Bloch Sphere showing a) Spin packets precessing in the laboratory frame at the Larmor frequency b) The rotating frame with a static magnetisation vector due to an on resonance field c) The rotating frame with 'fanning out' of the spin packets due to off-resonance effects. d) The effect of π pulse about the y-axis, refocusing the spin packets in a Hahn echo.

[2]The dead time is the time between excitation and detection which is blanked to prevent the cavity ringing, from the high power excitation pulses, blowing the detection circuit.

2.2.2 Relaxation and decoherence: T_1 and T_2

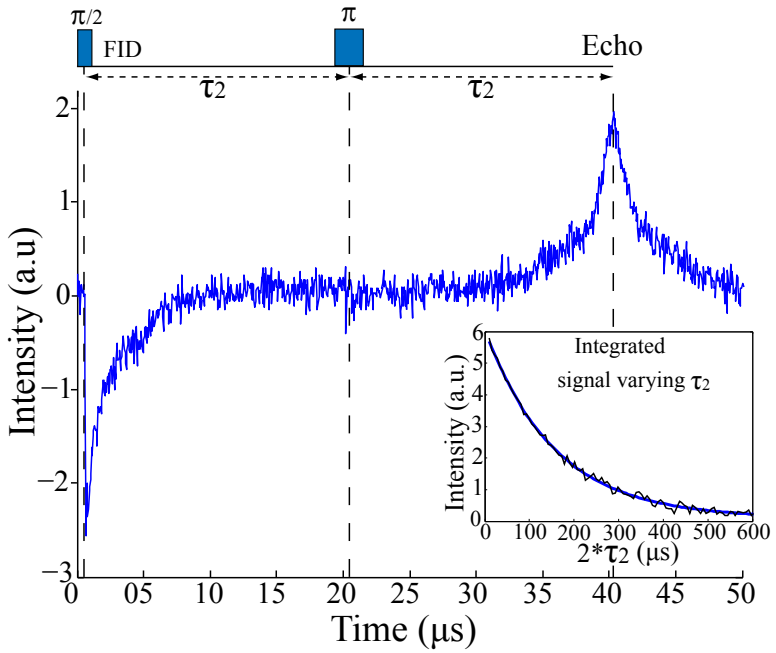

Figure 2.3: A Hahn echo sequence showing an FID and echo for $^{15}N@C_{60}$ where τ_2 is fixed at 20 μs. Incrementing τ_2 and integrating the echo signal T_2 can be extracted, as shown in the inset, with a monexponential decay giving an electron $T_2 = 160\mu$s at 40 K. Alternatively, τ_2 can remain fixed but the delay after a population inversion varied to give T_1.

The system thus far has been considered without the effects of relaxation or decoherence which were introduced in Chapter 1.2.1 and Chapter 1.2.2. The longitudinal relaxation time, T_1, will act to align the magnetisation along the B_0 field and can be measured by inverting the Zeeman population (π pulse) and watching it recover by observation of the FID ($\pi/2$ pulse) for a number of shots. The measurement sequence is subsequently $\pi-\tau_1-\pi/2-$FID or more commonly using the Hahn echo, $\pi-\tau_1-\pi/2-T-\pi-T-echo$, where τ_1 is stepped and T is short and fixed. The transverse dephasing, T_2*, can be measured by observation of the FID decay due to static inhomogenities such that individual spins experience a slightly different magnetic field ($\Delta\omega$). The effect of these inhomogenities can be refocused using the Hahn echo technique to typically give a longer decoherence time known as the T_2, found by incrementing the time between creation and detection of the quantum state. Specifically the T_2 time illustrates the non-reversible loss of quantum information from the system and can be ascertained

using the sequence $\pi/2 - \tau_2 - \pi - \tau_2 - echo$, where τ_2 is varied.

Microwave phase noise can become a problem at $\tau > 0.5$ ms [TMB06] but can be overcome by using single shot magnitude detection, [in-phase^2+quadrature^2]$^{1/2}$. The signal intensity, I, for a monoexponential curve will therefore vary according to Eq. 2.1, for T_1 and T_2, respectively:

$$I(t) = I(t_0)e^{-(\tau_1/T_1)} \qquad\qquad I(t) = I(t_0)e^{-(2\tau_2/T_2)} \tag{2.1}$$

The sequences described are applicable to both EPR and NMR but in order to make these measurements for nuclear spins in the low concentration limit, new sequences must be developed to probe the nuclear spin through electron spin readout as shown in Chapter 5.

2.2.3 Density matrix formalisation and the Hamiltonian

The quantum mechanical state for a single spin, in a pure state where $|0\rangle$ and $|1\rangle$ are the observable eigenstates, is given by:

$$|\psi\rangle = \alpha\,|0\rangle + \beta\,|1\rangle \tag{2.2}$$

where α and β are complex numbers which satisfy the normalisation condition, $|\alpha|^2 + |\beta|^2$=1. However, to describe an ensemble of spins it is convenient to use density matrix formalisation:

$$\rho = \begin{pmatrix} \overline{|\alpha|^2} & \overline{\alpha\beta^*} \\ \overline{\alpha^*\beta} & \overline{|\beta|^2} \end{pmatrix} \tag{2.3}$$

where the bar denotes an ensemble average, $\overline{|\alpha|^2} = \sum_i p_i|\alpha|^2$, such that the density operator $\rho(t)$ is given by a weighted sum of sub-ensembles of states that are in a pure superposition, with the wavefunctions $|\psi_k\rangle$. This is termed a mixed state:

$$\rho(t) = \sum_k p_k\,|\psi_k\rangle\,\langle\psi_k| \tag{2.4}$$

In the density matrix diagonal elements describe state populations (z-magnetisation) and are measured using the S_z Pauli operator (i.e. $Tr[\rho, S_z]$). The off-diagonal elements describe coherences in the system and are measured using the S_x and S_y operators. If we have a coupled electron and nuclear spin state we must consider a specific basis for the density matrix, for instance, given a electron spin S=1/2 and nuclear spin I=1/2 system the diagonal components can be described by (S,I)=[(1/2,1/2),(1/2,-1/2),(-1/2,1/2),(-1/2,-1/2)] to give a matrix:

$$\rho = \begin{pmatrix} \rho_{1,1} & \rho_{1,2} & \rho_{1,3} & \rho_{1,4} \\ \rho_{2,1} & \rho_{2,2} & \rho_{2,3} & \rho_{2,4} \\ \rho_{3,1} & \rho_{3,2} & \rho_{3,3} & \rho_{3,4} \\ \rho_{4,1} & \rho_{4,2} & \rho_{4,3} & \rho_{4,4} \end{pmatrix} \tag{2.5}$$

where *black* represents the populations, *blue* electron coherences, *red* nuclear coherences and *green* electron-nuclear coherences. The coherences in the density matrix can be further categorised according to their coherence order known as p ($p = |\Delta m_{J_1} + \Delta m_{J_2}|$, where m_{J_1} and m_{J_2} are the magnetic quantum numbers of the two states involved in the transition):

$$\rho = \begin{pmatrix} P & SQ^2 & SQ^1 & DQ \\ SQ^2 & P & ZQ & SQ^1 \\ SQ^1 & ZQ & P & SQ^2 \\ DQ & SQ^1 & SQ^2 & P \end{pmatrix} \tag{2.6}$$

where P refers to a population. The single-quantum (SQ) transitions are given when exactly one of the two spins changes its magnetic quantum number by one, such that the coherence order is given as $p = 1$. In the above matrix, SQ^1 are given with $|\Delta m_{J_1}| = 1$, $\Delta m_{J_2} = 0$ and SQ^2 are shown with $\Delta m_{J_1} = 0$, $|\Delta m_{J_2}| = 0$. The zero-quantum coherences (ZQ) are given with $p = 0$ and the double-quantum coherences (DQ) with $p = 2$. Larger spin systems involving coherence orders > 1 are referred to

as multiple quantum coherences.

The full static spin Hamiltonian for a coupled system, such as the one described above, is given by [SJ01a]:

$$\mathcal{H}_0 = \omega_e S_z - \omega_I I_z + \vec{S}A\vec{I} + \vec{S}D\vec{S} + \vec{I}P\vec{I} \tag{2.7}$$

where ω_e and ω_I are the electron and nuclear Zeeman or Larmor (ω_L) frequencies, S_z and I_z are the electron and nuclear Pauli operators and $\vec{S}A\vec{I}$ describes the hyperfine coupling between electron and nuclear spin states (made up of an isotropic term given as $a\vec{S}\vec{I}$, and an anisotropic term, $\vec{S}T\vec{I}$). Spin systems with $S > 1/2$ and non-cubic symmetry introduce a zero field splitting (ZFS) term to the Hamiltonian, described by $\vec{S}D\vec{S}$ and arising from dipole-dipole coupling between electron spins. Finally, though typically weaker, $\vec{I}P\vec{I}$ (also sometimes given as $\vec{I}Q\vec{I}$) denotes the nuclear quadrupole interaction (for nuclei with $I \geq 1$) arising from the interaction of the non-spherical charge distribution of nuclei with the electric field gradient caused by nearby electrons and/or nuclei. The Hamiltonian for two weakly interacting unpaired electrons, S_1 and S_2, can be described by their individual Hamiltonians (given by *Equation* (2.7)) with an additional Heisenberg exchange coupling term, $\vec{S_1}J\vec{S_2}$, and dipole-dipole coupling term, $\vec{S_1}D\vec{S_2}$. Subsequently, from the density matrix and time dependent Hamiltonian we can ascertain the quantum mechanical evolution of the system using the Liouville-von Neumann equation:

$$\frac{d\rho}{dt} = -i[\mathcal{H}(t), \rho(t)] \tag{2.8}$$

with a time-independent Hamiltonian given by:

$$\rho(t) = U(t)^{\dagger}\rho_0 U(t) \tag{2.9}$$

where $U(t) = e^{(-i\mathcal{H}t)}$. This formalisation allows us to model the evolution of coupled electron-nuclear spin systems under relaxation as described further in Section 5.2.2.

3

Electron spin relaxation and decoherence

3.1 Introduction

The introduction to quantum computing introduced two schemes that formed powerful proposals towards QIP: the Kane proposal, using Si:P; and molecular proposals using endohedral fullerenes. Within these proposals investigating and improving the electron spin decoherence times are key requirements, as outlined in DiVincenzo's criteria (Section 1.2.2). Solid state materials such as Si:P offer the advantage of incorporation into existing technologies, contributing to extensive previous studies of their characteristic electron spin properties [Feh59, FG59, WF61, TLAR03, TMB06, ATT10]. However, Si:P suffers from difficulties in controllable qubit placement for larger spin architectures.

This can be overcome using molecular systems with the advantages of self-assembly and a 'chemists toolkit'. Molecular systems are in their relative infancy but N@C_{60} has emerged a 'frontrunner' due to its long T_{2e} times [Har02, MTA06, MTA07], though suffers from low production yields and slow purification. In contrast, metallofullerenes can be produced with 100% yield and are easily purified but have not shown long coherence times. This chapter will therefore discuss relaxation and decoherence in the metallofullerenes species, Y-, Sc- and La@C_{82}, and investigate N@C_{60} in regimes that have yet to be studied.

3.2 Metallofullerene electron spin relaxation and decoherence

3.2.1 Metallofullerene EPR

Several electron paramagnetic resonance (EPR) studies have been conducted on the metallofullerenes Sc-, La- and Y@C_{82} focusing on geometric and electronic properties of the molecules [KSK93, RPS95, IS00, SBD98, KGM98, OOS95, WKD04, MHL05, JGDH08, IWB10]. These, along with x-ray diffraction measurements, have shown the metal atom to be off centre in the cage [NTS00, NTS98, TUN95], with charge transfer to the cage dependent on the metal ion species [NK93]. It is this charge transfer that leads to the unpaired electron that produces the EPR signal, which will be further split by the hyperfine interaction according to the Hamiltonian:

$$\mathcal{H}_0 = \omega_e S_z - \omega_I I_z + a \cdot \vec{S} \cdot \vec{I} \tag{3.1}$$

where $\omega_e = g\beta B_0/\hbar$ and $\omega_I = g_I \beta_n B_0/\hbar$ are the electron and metal atom nuclear Zeeman frequencies, g and g_I are the electron and nuclear g-factors, β and β_n are the Bohr and nuclear magnetons, $\hbar$ is Planck's constant and B_0 is the magnetic field applied along z-axis in the laboratory frame. The species studied are all electron spin S=1/2,

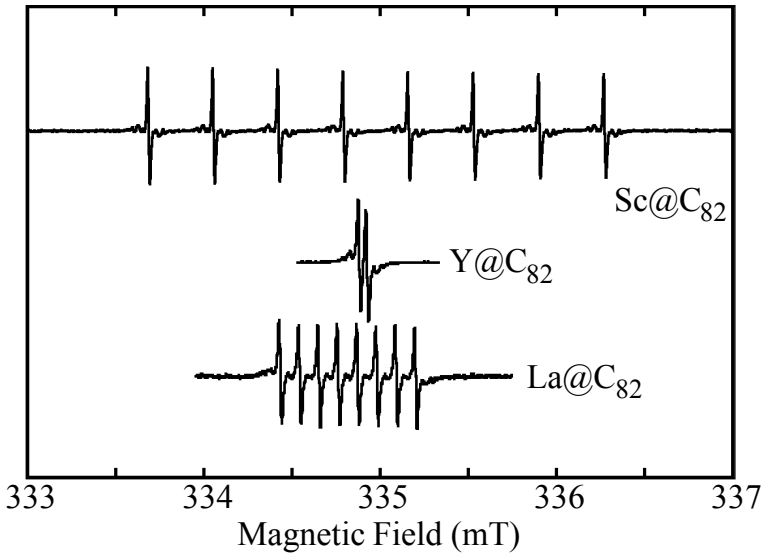

Figure 3.1: CW EPR of the metallofullerenes Y-, Sc- and La@C_{82} in toluene solution at room temperature. The hyperfine splitting is clearly visible for all samples in agreement with previous literature values [SBD98].

with ^{45}Sc and ^{139}La nuclear spin $I = 7/2$, while ^{89}Y has $I = 1/2$ (each of these isotopes has 100% natural abundance). In liquid solution this leads to 8 hyperfine lines for Sc- and La@C_{82} with an EPR doublet for Y@C_{82}, shown in Figure 3.1 for a toluene solution. The hyperfine coupling can then be easily extracted with literature values given as 0.370, 0.114 and 0.048 mT for Sc-, Y- and La@C_{82}, respectively [SBD98]. If one is to decrease the sample temperature, for instance to eliminate relaxation or decoherence mechanisms, frozen solutions are produced which show an anisotropic powder pattern for Y- and La@C_{82} from which individual m_I lines cannot be resolved [KGM98], as shown in Figure 3.2. In Sc@C_{82} the strong hyperfine coupling can be more clearly resolved as previously seen by Morley *et al.* [MHL05]. In contrast, Knorr *et al.* [KGM98] observed a broad background signal with a sharper feature, which we attribute to clustering of metallofullerene species due to an inhomogeneous sample resulting from a 'poor freeze'. We observed similar spectra when the sample did not freeze homogeneously (with the Sc hyperfine coupling still visible) but such conditions were not used to take measurements. The data in Figure 3.2 can be fitted using Easyspin [SS06] to give the anisotropic g-factors, (g_x, g_y, g_z)=(2.0022, 2.0023, 1.9974), (1.9969, 2.0036, 1.9999) and (2.0060, 2.0044, 1.9980) for Y-, Sc- and La@C_{82}, respectively. These are

in good agreement with previous studies. [KGM98, MHL05]. The hyperfine tensor for $Sc@C_{82}$ is found to be A=[15.4, 7.8, 7.3] MHz in agreement with Morley *et al.* [MHL05] but in contrast to Knorr *et al.* [KGM98] where the hyperfine coupling was not resolved. The fitting for $La@C_{82}$ also required some hyperfine terms to give the correct intensity but values could vary significantly and were fixed to A=[0.9, 0.9, 2.1] MHz, as extracted by the analysis of electron spin echo envelope modulation (ESEEM) data in Ref [KGM98].

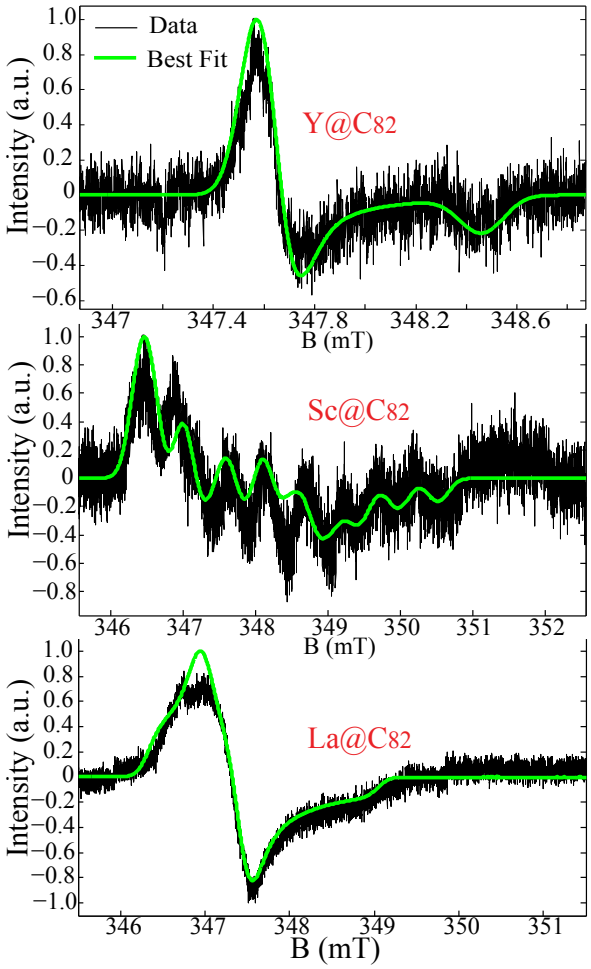

FIGURE 3.2: CW EPR of the metallofullerenes Y-, Sc- and $La@C_{82}$ in a frozen deuterated toluene solution at 40 K. The hyperfine splitting is only resolved for $Sc@C_{82}$. The data is fitted using Easyspin with the fitting parameters reported in the text. The relatively low signal to noise is due to the low concentration of the samples. Modulation frequency 100 kHz, microwave power < 5 μW and modulation amplitude 0.85, 5 and 1 G, respectively.

Previous EPR studies have primarily used CW spectroscopy and as such few T_{2e} times have have been extracted in literature. Using pulsed EPR, Knorr *et al.* report a T_{2e} of 600 ns for Sc@C_{82} (in trichlorobenzene solvent at 2.5 K) but a measured T_{2e} of 4.1 μs in a Y@C_{82} sample was attributed to a 'background' signal [KGM98]. Okabe *et al.* also report a temperature and m_I dependence of T_{1e} and T_{2e} for La@C_{82} (in CS_2) arising from motional effects of anisotropic interactions and coherence times < 1.5 μs, in the range 183–283 K. [OOS95]. The DPhil thesis by Morley [Mor05a] improves significantly on these T_{2e} times with a single temperature measurement for Sc@C_{82} at 20 K in deuterated toluene, giving T_{2e} =13 μs. However, clearly these times are substantially lower than those observed for N@C_{60} of up to 250 μs [MTA06] and thus warrant further attention. Similarly, no temperature dependence studies have been undertaken to understand the mechanisms behind relaxation or decoherence in these systems (at low temperatures), which is crucial in order to maximise and understand how larger architectures will effect these parameters.

3.2.2 Metallofullerene decoherence times in CS_2

To achieve long metallofullerene decoherence times three essential criteria must be fulfilled, the metallofullerene solution or matrix must be: 1) dilute, to avoid dipolar coupling of neighbouring spins which will cause decoherence 2) a good solvent for metallofullerenes and 3) contain few additional spins that can act to cause decoherence such as oxygen, impurities or nuclear spins. In these studies solutions have therefore all been prepared at low concentrations of $10^{-6} - 10^{-7}$ M and freeze-pump thawed several times to remove paramagnetic O_2. An ideal solvent is CS_2 which contains no nuclear spins and has good metallofullerene solubility at low concentrations. The T_{1e} and T_{2e} times for metallofullerenes in CS_2 are shown in Table 3.1 with a maximum T_{2e} of 4.6 μs for Sc@C_{82} at 170 K.

The exact charge transfer from the metal atom to the fullerene cage is open to some debate in literature but is accepted to follow La>Y>Sc [NK93]. Comparing this

Metallofullerene	Room temp.		170 K	
	T_{1e} (μs)	T_{2e} (μs)	T_{1e} (μs)	T_{2e} (μs)
Sc@C_{82}	2.0	1.0	6.0	4.6
Y@C_{82}	0.7	1.0	2.5	2.4
La@C_{82}	-	-	2.9	1.6

Table 3.1: Metallofullerene T_{1e} and T_{2e} times in CS_2 liquid solution at room temperature and 170 K (measurements taken on the $m_I = 1/2$ hyperfine lines).

with the T_{2e} times for the metallofullerene species in CS_2, that follow La<Y<Sc, it indicates that decoherence may be due to motional effects leading to modulation of anisotropic interactions, or spin rotational effects induced by solvent molecule collisions. To achieve longer T_{2e} times in this solvent one must reduce or eliminate such decoherence mechanisms by moving to lower temperatures. Unfortunately CS_2 freezes below ∼160 K forming a poly-crystalline matrix which will result in grain-boundaries and clustering of metallofullerene species, reducing T_{2e} due to dipolar coupling. Previous N@C_{60} studies have used small quantities of S_2Cl_2 which acts as a glassing agent for CS_2, producing a homogeneous matrix [MTA06]. However, adding S_2Cl_2 to a CS_2 metallofullerene solution results in no EPR signal, presumably due to a reaction with the charged metallofullerene cage which yields an EPR silent product[1] e.g. 2M@C_{82}+ $S_2Cl_2 \rightarrow 2$(M@C_{82})S + Cl_2

3.2.3 Metallofullerene decoherence times in toluene

An alternative metallofullerene solvent is toluene which has the benefit of forming a homogeneous glass when flash frozen[2] but contains nuclear spins. The T_{2e} times are again short at higher temperatures but by forming a glass lower temperatures can be probed, as shown for both h-and d-toluene in Figure 3.3 (raw data in appendix). The measurements for these and all subsequent experiments were conducted on the Sc@C_{82} $m_I = 1/2$ line and on the $g_\perp$ peak for Y- and La@C_{82}, with a typical π pulse of 80 ns.

[1] On addition of S_2Cl_2 the solution is immediately flash frozen in an attempt to avoid a reaction. The proposed reaction could be checked by testing for the presence of Cl_2, for instance, by a simple litmus test.

[2] Flash frozen in liquid N_2, it should be noted that toluene does not freeze to give a homogeneous glass every time.

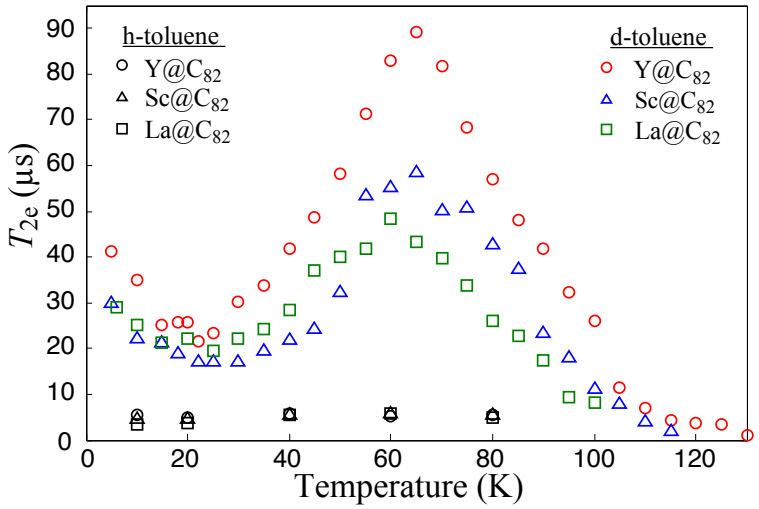

FIGURE 3.3: T_{2e} as a function of temperature for $Y@C_{82}$ (circle), $Sc@C_{82}$ (triangle) and $La@C_{82}$ (square) in deuterated toluene (coloured shape) and h-toluene (black shape, bottom of figure). Raw data in appendix.

T_{2e} in h-toluene is fairly independent of temperature and limited to $< 6\mu$s due to spectral diffusion, a mechanism whereby nuclear spin flips produce a fluctuating local magnetic field that drives electron spin decoherence [KA62, ZS69]. This is identified by a characteristic stretched exponential decay:

$$I(t) = I(t_0)e^{-(t/T_2)^x} \tag{3.2}$$

with $x > 1$. This decoherence mechanism is suppressed for metallofullerenes in d-toluene, due to the much weaker nuclear magnetic moment of deuterium. In this deuterated solvent the measured T_{2e} is longer and a monoexponential decay ($x = 1$) is observed for $T > 40$ K. T_{2e} passes through a maximum around 60–70 K of approximately 50, 60 and 90 μs for $La@C_{82}$ $Sc@C_{82}$ and $Y@C_{82}$ respectively, over an order of magnitude longer than previously published in literature. The longer coherence times of $Y@C_{82}$ can be attributed to the weaker hyperfine coupling and smaller nuclear spin of Y compared to Sc and La.

The decrease in T_{2e} below 60–70 K reflects the emergence of an alternative relaxation mechanism independent of the metal ion species, leading to a similar T_{2e} value for all

three metallofullerenes at around 20 K. A prime candidate is the slow rotation of the toluene solvent methyl group which drives deuterium nuclear spin flips and electron spin decoherence via spectral diffusion [SF97]. The deuterium spin flip rate, W_a, is given by the equation [SF97, BBM99]:

$$W_a = \frac{1}{60}\left(4\pi^2 \Delta A_a^2 \frac{\tau_c}{1+\omega_a^2\tau_c^2}\right) \tag{3.3}$$

where τ_c is the correlation time, ΔA_a is the difference between the hyperfine interactions of the deuterium proton for the two positions exchanged during the rotation and ω_a is the deuterium Larmor frequency (2 MHz in the 0.35 T field used here). This spin flip rate will be maximised at $\omega_a^{-1} = \tau_c$. We assume an Arrhenius temperature dependence for τ_c given by:

$$\tau_c^{-1} = \tau_{\infty,c}^{-1} e^{-\Delta E/kT} \tag{3.4}$$

where k is the Boltzmann constant, ΔE is the energy barrier equivalent to 150–160 K and $\tau_{\infty,c}^{-1} = 10^{12}$ s^{-1} [MWSPK79]. Thus, the maximum spin flip rate, corresponding to a minimum in T_{2e}, will occur at about 14 K (where $\tau_c^{-1} = 1.4 \times 10^7$ s^{-1}) slightly lower than the value of ∼20 K predicted by our measurements.

3.2.4 Metallofullerene decoherence times in othoterphenyl

To improve metallofullerene T_{2e} times further and prove that methyl rotation is the relaxation mechanism in d-toluene below 60–70 K, one can move to a solvent that does not contain a methyl group. Deuterated orthoterphenyl is a suitable solvent as it contains no methyl group (see Figure 3.4, insert) and reproducibly forms a glass at low temperatures. The solvent is actually a solid at room temperature and thus it must be heated to ∼60 K to incorporate metallofullerene species before flash freezing in liquid N_2. Prior to this the sample is degassed by pumping for several hours whilst in a solid powder form.

The T_{2e} times for Y@C_{82} in this solvent and d-toluene are compared in Figure 3.4 (we

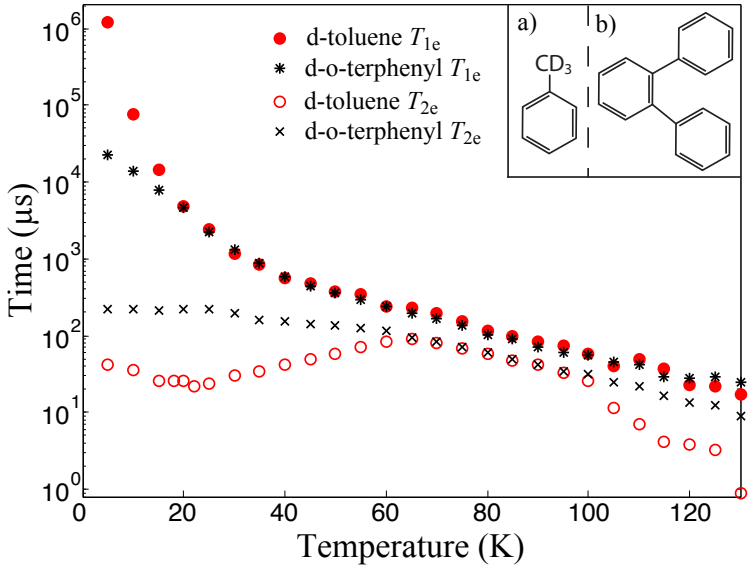

FIGURE 3.4: $Y@C_{82}$ relaxation and coherence times as a function of temperature in deuterated toluene (circle, T_{1e} closed, T_{2e} open) and deuterated o-terphenyl (symbol black, T_{1e} star, T_{2e} cross). T_{1e} is largely the same for both solvents, with a deviation at temperatures below 15 K. Insert: Structural representation of a) d-toluene and b) o-terphenyl.

observed similar results for La and $Sc@C_{82}$). As predicted, the drop in T_{2e} observed in d-toluene as the temperature is reduced below 65 K is not observed in deuterated o-terphenyl, due to the absence of methyl groups in this solvent. In the range $T < 65$ K, T_{2e} rises slowly with decreasing temperature, and fits well to a stretched exponential in which the stretching factor increases from $x = 1$ at 65 K to a limit of $x \approx 1.7$ at low temperatures. We attribute this new limit to the emergence of spectral diffusion from the deuterium nuclear spins in the frozen solvent environment. In the range 65 to 100 K, T_{2e} fits to a monoexponential decay and reveals the same coherence times as d-toluene, which appears to be determined by T_{1e} relaxation, discussed in the next section. Above 100 K, the T_{2e} values of the two solvents again deviate, which can be associated with the different glass transition temperatures (T_g), where $T_g = 117$ K for toluene and 243 K for o-terphenyl.

Under these optimised conditions, we have measured a maximum T_{2e} of 225 ± 7, 245 ± 9 and 204 ± 2 μs for $Y@C_{82}$ $Sc@C_{82}$ and $La@C_{82}$ respectively at 5–10 K, with $x = 1.6$–1.7 (the error in x is $< \pm 0.12$). A typical electron spin echo decay trace is shown in

Figure 3.5, and fits well to a simple stretched exponential, or a decay of the form:

$$I(t) = I(t_0)e^{-(t/T_{2e,\mathrm{int}})-(t/T_{SD})^2} \tag{3.5}$$

from which an intrinsic $T_{2,\mathrm{int}}$ can be extracted, as the T_{SD} term accounts for spectral diffusion [ZS69]. This gives $T_{2e,\mathrm{int}} = 610 \pm 80$ μs, offering an estimate of the decoherence time in the absence of spectral diffusion, i.e. if all environmental nuclear spins were removed ($T_{SD} = 249 \pm 7$ μs). Considering literature on donors in natural silicon the $T_{2e,\mathrm{int}}$ is often quoted as the T_{2e} time as nuclear spins can be removed from the silicon matrix, which would be very difficult in these solvents discussed [TLAR03, MPZ10]. Nevertheless, the stretched exponential T_{2e} times are over two orders of magnitude longer than previously published for metallofullerenes. Given the ability to manipulate spins within tens of nanoseconds, this result puts metallofullerenes in a regime where quantum error correction is feasible [DiV00]. Thus, metallofullerenes can now be considered a suitable qubit candidate for quantum computation and research into larger QIP architectures such as 'peapods' is justified.

3.3 Metallofullerene relaxation times

In contrast to T_{2e}, measurements of T_{1e} appear to be relatively independent of the solvent environment (see Figure 3.4), indicating that over the range 20 to 130 K the glass matrix does not have a dominant effect on relaxation. Figure 3.6 (top) further shows there is a systematic shift in both the magnitude and temperature dependence of T_{1e} which follows the increasing mass of the ions.

In the N@C_{60} fullerene, electron spin relaxation has been found to show an Arrhenius-type temperature dependence corresponding to a two-phonon relaxation process via the vibrational motion of the cage [MTA06]. This has the form:

$$T_1 \propto e^{(\Delta/k_B T)} - 1 \tag{3.6}$$

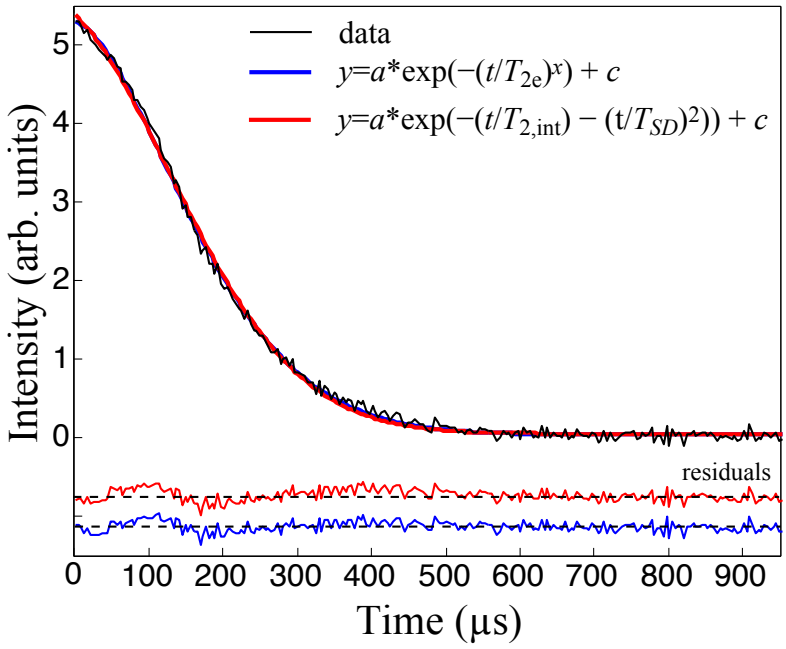

Figure 3.5: Hahn echo decay for La@C_{82} at 10K, data (black) showing spectral diffusion and fit with a stretched exponential decay (blue (dark grey)) and a curve to extract the intrinsic T_{2e} in the limit of no environmental nuclear spins (red (grey)). Curves are similar and thus overlap, the residual to the fits is shown at the bottom of the figure. Oscillations in the residual to the fit are due to ESEEM modulation on the short timescale.

where Δ is the energy of the molecular vibrational mode. The temperature dependence of T_{1e} in Y-, Sc- and La@C_{82} can be described by two such processes over the range of 15 to 100 K, as shown in Figure 3.6 (bottom). The extracted vibrational mode energies (in cm^{-1}) for each of the two processes are shown in Table 3.2. Below 20 K, an additional relaxation mechanism is present arising from the glassy solvent environment, particularly effective in the case of the deuterated o-terphenyl solvent.

Mode	Wavenumber (cm^{-1})		
	Y@C_{82}	Sc@C_{82}	La@C_{82}
ν_1	54 ± 4	59 ± 8	19 ± 5
ν_2	403 ± 214	229 ± 43	125 ± 33

Table 3.2: Extracted molecular vibrational modes from fitting T_{1e} temperature dependence in the range 15–100 K, following Eq. 3.6.

The resonant frequencies can be compared to far infrared (FIR) and Raman studies of metallofullerenes that have shown frequencies $<$ 200–300 cm^{-1} to be characteristic

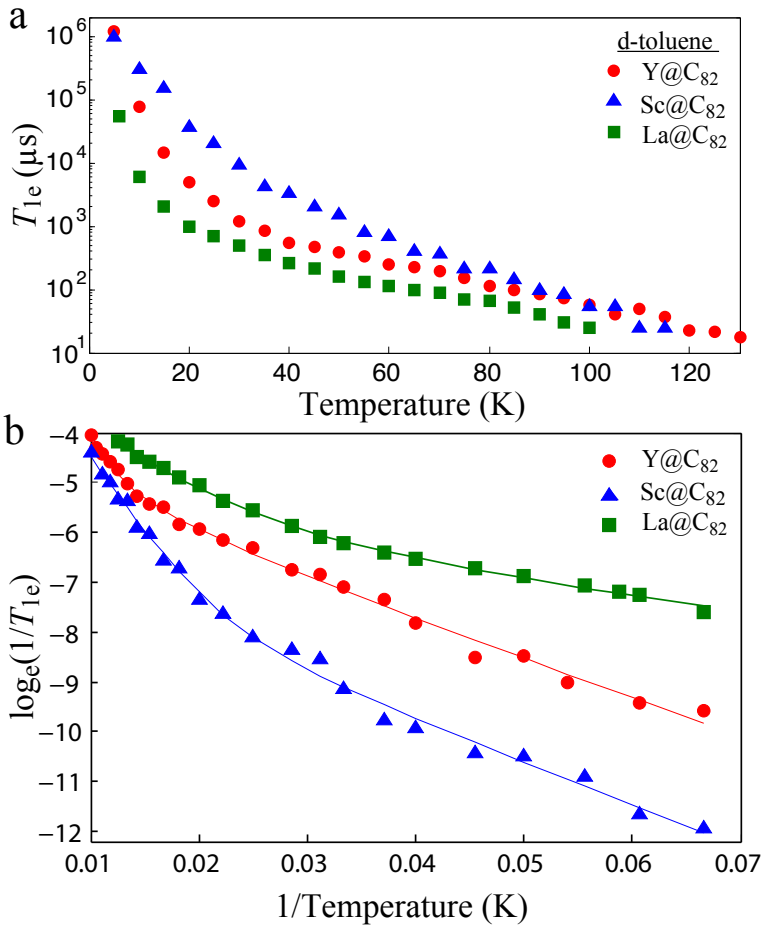

FIGURE 3.6: T_{1e} as a function of temperature for Y@C_{82} (circle), Sc@C_{82} (triangle) and La@C_{82} (square) in deuterated toluene on a) a standard plot and b) an Arrhenius style plot to extract the molecular vibrational modes shown in Table 3.2.

of metal-cage vibrations [LRH98, KK02, KHK00]. If metal-cage motion is considered in terms of a simple linear oscillator model the vibrational frequency (ν) would be proportional to $\mu^{-1/2}$ (where μ is the reduced mass). Thus, one would expect the wavenumber to follow La<Y<Sc as observed for the extracted low frequency mode (ν_1) in Table 3.2. This model is entirely appropriate given Raman data that shows the linear oscillator force constant to be the same for a number of different metallofullerenes, including La and Y@C_{82}, which have the same (+3) oxidation state[3] [LRH98]. The linear dependence of ν and $\mu^{-1/2}$ in the Lebedkin *et al.* manuscript indicates that

[3]whilst the assignment of La and Y@C_{82} to a oxidation state of +3 is widely accepted that of Sc@C_{82} is not. Often given as +2, recent studies have shown a +3 assignment to be correct but with substantially different atom-cage charge transfer to the aforementioned species [MHL05].

the atom mass (and the bonding character) is dominating the metal-cage vibrational frequencies and factors such as the diameter of the atom in the cage have little effect. The experimental data will deviate from this model due to, for instance, charge transfer, which is known to be quite different for the metallofullerenes studied [NK93, KK02]. However, the general trend holds and therefore is a good indicator that ν_1 may be related to metal-cage vibrations.

Lebedkin *et al.* identify a mode for Y@C_{82} at 54 cm^{-1} which they attribute to a 'lateral' metal-cage vibration [LRH98], in good agreement with the Y@C_{82} extracted vibrational mode ν_1. Similar experimental data on La@C_{82} is less conclusive, with a broader mode centered at ∼45–50 cm^{-1} for La@C_{82} [LRH98], though theoretical studies have predicted 'lateral' La-cage modes at 27 and 30 cm^{-1} [KN03], slightly higher than our extracted value. This lateral metal-cage mode in La@C_{82} has also been identified using x-ray powder diffraction maximum entropy method (MEM) analysis [NTS00], where a large charge density distribution was attributed to 'giant motion' (see Figure 1.9). La would therefore be expected to give a significantly lower metal-cage frequency than from the tight distribution observed for Sc and Y in the C_{82} cage [NTS98, TUN95], consistent with our results. It therefore appears that the lower frequency excited state (ν_1) may be due to metal-cage vibrational modes and that this is the dominant cause of T_{1e} relaxation in the system over the temperature range 15–60 K.

Above this temperature, the data can be fit by a higher resonant frequency (ν_2) (Figure 3.6 (bottom)), though this value is harder to interpret as it may derive from a combination of many higher energy cage vibrational modes. However, ν_2 in La@C_{82} could correspond to the 'longitudinal' metal-cage vibrational mode observed at 163cm^{-1} [LRH98]. In addition to the different slopes in the temperature dependence of T_{1e}, the magnitude of T_{1e} follows La>Y>Sc in accordance of the varying extent of charge transfer between the metal and cage [NK93]. This charge transfer would increase the spin orbit coupling to these molecular vibrational modes, giving the observed order of ${T_{1e}}^{-1}$ La>Y>Sc. The T_{1e} times although not indicative of the time to store quantum information are of importance in storing classical information. They also give the fundamental limit

for the storage of quantum information in both the electron spin ($T_{2e} \leq 2\,T_{1e}$) and as we shall see in Chapter 4 the nuclear spin state ($T_{2n} \leq 2\,T_{1e}$, for a electron spin-1/2 system).

3.4 Metallofullerenes in a solid matrix

Instead of suspending metallofullerenes in a solvent system a solid state matrix can be envisaged. This has the advantage that it can be engineered to contain no nuclear spins and does not require a solvent with metallofullerene solubility or the ability to form a glass at low temperatures. A natural matrix is that of empty fullerene cages such as C_{60} or C_{82}, which can be made at higher concentrations (but still with minimal dipolar interaction) than solvent systems which cluster more readily. The results of room temperature measurements on La@C_{82} in both C_{60} and C_{82} matrices, that are predominately held on the EPR tube walls, are shown in Table 3.3. The results are in contrast to cw measurements which suggest C_{82} forms a better matrix, discussed further in Ito *et al.* [IWB10], and unlike solution measurements, distinct bi-exponential behaviour is observed. This reason for the differences between cw and pulsed measurements may be because pulsed methods can be used as a highly sensitive spin environment probe (given the appropriate spin). Measurements can be affected by very small amounts of clustering, impurities or oxygen, the latter of which has been identified in other endohedral fullerene materials [DKKW00]. This sensitivity is confirmed by low temperature measurements on Y@C_{82} which do not show $T_{2\mathrm{e}}$ times greater than 1.6 μs. The short $T_{2\mathrm{e}}$ times may be due to the preparation of the materials and could be improved using a different technique. If a powder sample was produced filling the EPR tube rather than just lining the walls, different behaviour may be observed. Producing larger dispersions of metallofullerenes in C_{82} is not straightforward due to the requirements of large amounts of material and, given the high metallofullerene yield, additional pristine C_{82}. However, N@C_{60} is naturally produced in low yield, ideal for preparation of samples in a C_{60} matrix, as shown in the next section.

Measurement time	Matrix environment and metallofullerene concentration			
	C_{82} 1%	C_{60} 1%	C_{82} 0.1%	C_{60} 0.1%
T_{2e} (μs)	0.39	0.64	0.67	0.84
T_{1e} short (μs)	0.75	0.96	0.87	0.98
T_{1e} long (μs)	10.18	10.72	99.97	136.08

Table 3.3: La@C$_{82}$ T_{1e} and T_{2e} times in C$_{82}$ and C$_{60}$ solid matrices at 1% and 0.1%, measured at room temperature.

3.5 ^{15}N@C$_{60}$ relaxation and decoherence times

3.5.1 ^{15}N@C$_{60}$ EPR

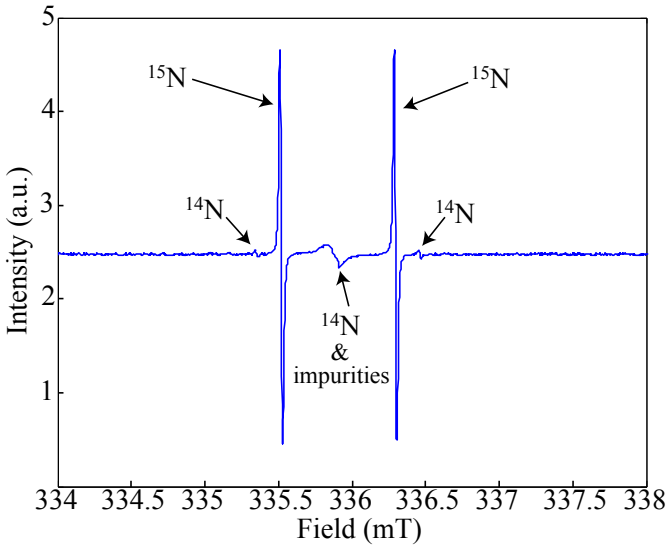

FIGURE 3.7: Continuous wave EPR of a powder ^{15}N@C$_{60}$ in C$_{60}$ matrix sample measured at room temperature (modulation amplitude 0.2 G, modulation frequency 100 kHz, microwave power 0.2 mW). The ^{15}N, impurity and residual ^{14}N peaks are labelled.

The spin relaxation properties of ^{14}N@C$_{60}$ have been previously investigated, predominately in solvent based systems [MTA05b, MTA07, MTA06, Mor05b, Mor05a, DHP99, KDP97, Har02] but also in powder systems [Har02, DKKW00, WKD99][4]. In contrast, ^{15}N@C$_{60}$ has been used to perform experiments showing electron and nuclear pseudoentanglement [MSW04] and dynamic nuclear polarisation [MVTA07] but relaxation

[4]the latter two only report T_{1e}.

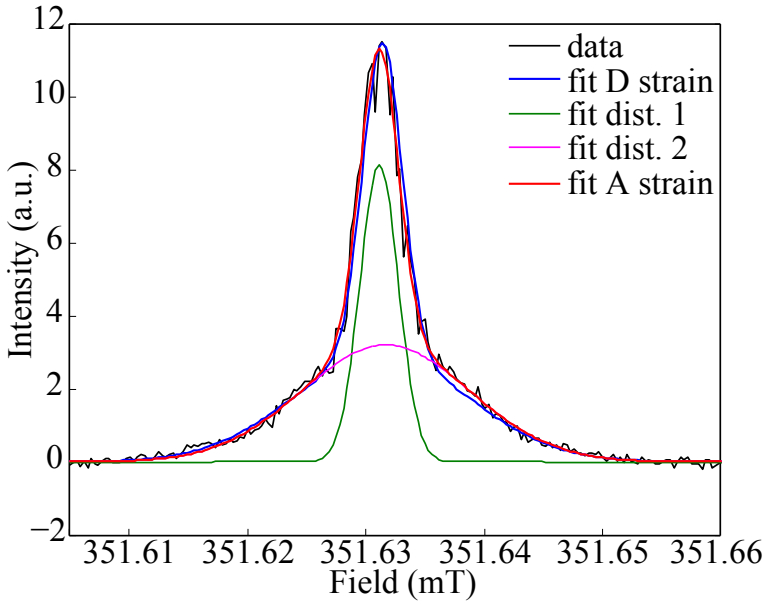

FIGURE 3.8: Echo detected field sweep of a powder $^{15}N@C_{60}$ in C_{60} matrix high field line at 40 K ($\tau = 10$ μs, π pulse= 60ns). The spectrum is fit using Easyspin [SS06] with a zero field splitting, $D = 0.24$ MHz (where the Hamiltonian has an additional $D.S_z^2$ term and $D = \frac{3}{2}D_z$ ($E = 0$)) and a fwhm linewidth of 39 mG (blue). The spectrum can alternatively be fit to 2 Gaussian functions (green, pink) of fwhm linewidth 16.3 and 71.1 mG, respectively. The latter corresponds to an A strain of 0.94 MHz.

has not been extensively studied. T_{2e} times in solid matrix $^{14}N@C_{60}$ and $^{15}N@C_{60}$ systems have been reported as up to 20 and 14 μs, respectively, much shorter than in their solvent based counterparts [Har02]. In this section we will investigate $^{15}N@C_{60}$ in a C_{60} matrix to see if longer decoherence times can be achieved, advantageous for schemes that use multiple isotopes to selectively address qubits and for use in exploiting the nuclear qubit state (see Chapter 4).

$^{15}N@C_{60}$ powders were produced by arc discharge and ion bombardment using 99% enriched ^{15}N. The powder was purified using HPLC to obtain the required concentration and remove unwanted amorphous material, before transferring it to an EPR tube. The sample was then degassed for several hours to remove paramagnetic O_2 before sealing. The transfer stage was crucial in determining the amount of impurities in the powder: contact with air resulted in an increase in the impurity peak. However, impurities did not seem to impact the T_{2e} of the system significantly — though we will show they are important when extracting longer decoherence times — and although it is

believed that degassing may be crucial, pumping times and vacuums did not show any correlation with T_{2e}. Thus, factors beyond our control such as ^{15}N@C$_{60}$:C$_{60}$ packing may be affecting degassing. ^{15}N@C$_{60}$ is an electron spin-3/2, nuclear spin-1/2 system (^{14}N is nuclear spin 1) which gives a doublet EPR spectrum as shown in Figure 3.7. The figure also shows a central peak due to impurities and small outlying peaks arising from the residual ^{14}N@C$_{60}$ triplet splitting ($I = 1$). The impurity concentration is $\sim 1 \times 10^{15}$ spins/cm^3 (from spin counting) which have been cited as arising from fullerene-oxygen radicals [JBM06]. The impurities can be reduced by back-filling with argon after degassing and transferring the powder to the EPR tube under a constant argon flow, also shown in Ref [WLH01]. An echo detected field sweep of the high field line, Figure 3.8, shows evidence of zero field splitting (ZFS), which has previously been reported for similar N@C$_{60}$ powder systems [WKD99, DHP99]. The spectrum has been fitted using Easyspin [SS06] to give a principle D value = 0.24 MHz. Alternatively, the echo detected field sweep can be simulated by two Gaussian functions, one indicative of the intrinsic ^{15}N@C$_{60}$ linewidth and the other broadened due to a distribution of hyperfine constants, given as an A strain of 0.94 MHz. It is also entirely possible that both D and A strain are present, with the impact of these strains discussed in more detail later in this chapter.

3.5.2 ^{15}N@C$_{60}$ decoherence times in a C$_{60}$ matrix: Instantaneous diffusion

The decoherence time for a dilute ^{15}N@C$_{60}$ in C$_{60}$ powder sample was found to be $\sim$50 μs at room temperature but could be extended by decreasing the temperature to a limit of 160–190 μs, over the range 10–70 K. This sample gave the longest T_{2e} time of those produced, can be considered 'best' degassed with few impurities and is used for the data reported in this thesis. A prime candidate for the low temperature T_{2e} limit of this sample is decoherence via electron spin dipolar coupling. This can be observed through the modification of a standard Hahn echo experiment, $\pi/2 - \tau - \theta_2 - \tau -$

echo [SJ01a]. In this experiment the θ_2 pulse (which is typically π) acts to refocus effects such as magnetic field inhomogeneity, as well as other interactions experienced by the spin which are constant on the timescale of τ. However, if the θ_2 pulse flips both the spin that is observed and a dipolar-coupled neighbouring spin, the effect of this interaction is not refocused and the effective $T_{2\mathrm{e}}$ is reduced (this effect is termed instantaneous diffusion). If the θ_2 pulse is shortened it will act to refocus only a sub-set of spins and mimic a homogeneously dilute spin sample [SJ01a, KA62, TLAR03]. The relationship between the effective decoherence time ($T_{2e,\mathrm{ID}}$) and θ_2 for a spin 1/2 system is well known and given by Refs [SJ01b, SDR81]. In the high spin case a scaling factor, κ, needs to be applied to account for a higher spin number. Raitsimring *et al.* have previously used a $\sqrt{S(S+1)}$ weighting [KRT89, KRI91, LRG91] but only when extracted from the κ value for different spin number species and not explicitly calculated or quoted. We have calculated a slightly different scaling factor of $\sqrt{S(S+1)+0.25}$ (for half integer spins), which gives $\kappa = 2$ for a spin 3/2 system in the high temperature limit (Raitsimring would predict 2.24, with a decreasing deviation for increasingly higher spin number systems)[5]. The calculation considers the energy shift of adjacent levels due to the inversion of a neighbouring environmental spin and it is further confirmed by Walstedt and Walker [WW74]. Thus this yields:

$$1/T_{2e,\mathrm{ID}} = \frac{\mu_0 \pi g^2 \mu_B^2 C \kappa}{9\sqrt{3}\hbar} \sin^2(\theta_2/2) \tag{3.7}$$

where μ_0 is the permeability of free space, g is the g-factor, μ_B is the Bohr magneton and C the spin concentration for each hyperfine line. In Figure 3.9, the plot of $1/T_{2\mathrm{e}}$ vs $\sin^2(\theta/2)$ shows that $T_{2\mathrm{e}}$ can be simulated by a contribution from both $^{15}\mathrm{N@C_{60}}$ dipolar coupled spins, and $^{15}\mathrm{N@C_{60}}$ spins that are coupled to impurity spins. The impurity spin behaviour dominates the data at $\sin^2(\theta_2/2) < 0.2$ and is considered later in this section. At $\sin^2(\theta_2/2) > 0.2$ the experimental fitting is dominated by the effect of

[5] a physical interpretation for a spin 3/2 system is as follows, a -1/2:1/2 observer spin acquires phase (causing decoherence) that depends on the state of the neighbouring spins. If the neighbouring spin is in the $\pm 3/2$ levels then phase is accumulated 3 times faster than in the $\pm 1/2$ levels. At high temperatures weighting of the levels is equal and thus $\kappa = (3+1)/2 = 2$ (this would be 3 in the low temperature limit).

^{15}N@C$_{60}$ spins, according to relationship given in Eq.3.7. Using this equation and the slope from Figure 3.9, the spin concentration, C, is calculated as 2.5×10^{15} spins/cm^3 which is entirely consistent with the value obtained from spin counting (2–3 $\times$ 10^{15} spins/cm^3). The dipolar coupling frequency, ν_D, between two spins a and b can be found using:

$$\nu_D = \frac{\mu_0 \mu_B^2 g_a g_b}{4\pi h r_{a,b}^3}(1 - 3\cos^2\theta) \tag{3.8}$$

where $r_{a,b}$ the distance between the two spins and θ the angle between the Zeeman field and the inter-spin axis [SJ01c]. To obtain the mean nearest neighbour distance in a random distribution, $\langle r_{a,b} \rangle$, the spin concentration, C, can be used with Eq. 3.9 given by Bhattacharyya and Chakrabarti (where Γ is the Gamma function) [BC08].

$$\langle r_{a,b}(C) \rangle \sim \frac{\left[\Gamma\left(\frac{3}{2}+1\right)\right]^{1/3}}{\pi^{1/2}} \frac{\Gamma\left(1+\frac{1}{3}\right)}{\Gamma(1)} \left(\frac{1}{C}\right)^{1/3} \tag{3.9}$$

We note that $\langle r_{a,b}^3 \rangle$ (needed to calculate the mean dipolar coupling) diverges, reflecting the fact that dipole-dipole coupling breaks down at very short distances. If a physically motivated exclusion zone is imposed this does not provide a route to overcome this problem, as the coupling will be entirely dependent on the radius of the exclusion zone. Thus, averaging the angular dependence and considering $S = 3/2$, the dipolar coupling frequency at this distance is calculated as 2.5 kHz. It is this dipolar coupling that is limiting the measured T_{2e} of the sample using a standard Hahn echo.

The data where $\sin^2(\theta_2/2) < 0.2$ deviates from the linear $1/T_{2e}$ vs $\sin^2(\theta_2/2)$ dependence due to the effect of impurity spins. The cw spectrum (Figure 3.7) shows impurity spins centred approximately 4 G from the resonant ^{15}N@C$_{60}$ line with a distribution over $\sim$ 4 G and a similar concentration to ^{15}N@C$_{60}$. The initial π pulse in the instantaneous diffusion experiment has a duration of 200 ns, therefore (for instance) from a π to a $\pi/2$ pulse an excitation bandwidth of $\sim$2–6 G will be achieved and an excitation profile over the impurity spins. The impurity spins will have a number of different driving frequencies and an effective modulation amplitude of $B_1^2/(B_1^2 + \delta B^2)$, where B_1 is the microwave field strength and δB the field offset. To simulate the effect of this profile

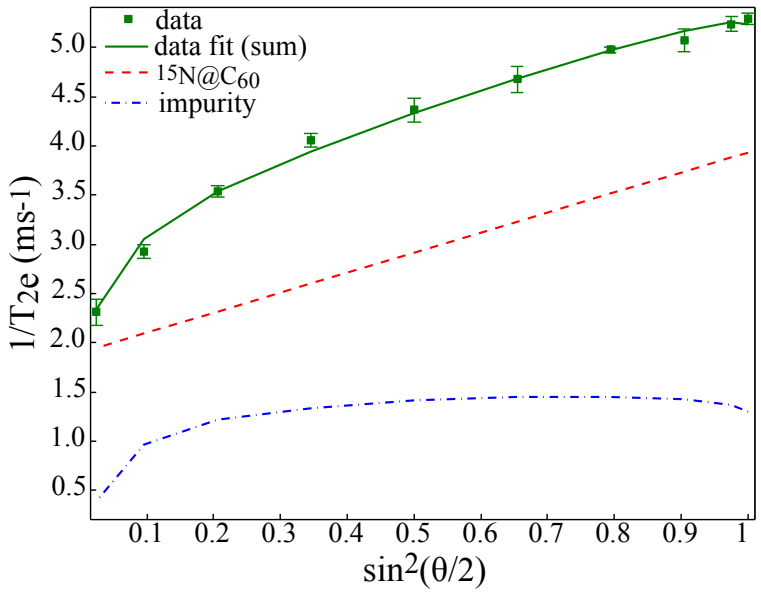

FIGURE 3.9: T_{2e} plotted against varying length of refocusing pulse (θ_2), from the standard Hahn echo sequence. The data (green square) is simulated by the sum (green line) of the contribution from $^{15}N@C_{60}$ spins (red, dashed line) and off-resonance impurity spins (blue, dot-dashed line). The simulation parameters are discussed in the text.

on the $^{15}N@C_{60}$ decoherence time the $\sin^2(\theta_2/2)$ term in Eq. 3.7 must be replaced (for the average frequency distribution of off-resonance spins) by the function [SDR81]:

$$F = \frac{B_1^2}{B_1^2 + \delta B^2} \sin^2(\theta_x/2) \tag{3.10}$$

where $\theta_x = \gamma t_p \sqrt{B_1^2 + \delta B^2}$ and t_p is the duration of the Hahn echo θ_2 pulse. This will give Eq. 3.7 when $\delta B = 0$. The impurity spins can be modelled by a Gaussian distribution and the average frequency distribution found by integrating over the field offset (δB). The simulation in Figure 3.9 is achieved using a distribution centred at an offset of 3.7 G (mean) with a standard deviation of 2 G and a concentration of 24×10^{15} spins/cm^3. The concentration is much higher than that extracted from spin counting which can arise due to a non-homogeneous distribution of impurity spins. Impurity spins could be preferentially found closer to the $^{15}N@C_{60}$ spins and may also be clustered. This is consistent with the observation that $^{15}N@C_{60}$:C_{60} packing may be important and, as shown in the next section, that $^{15}N@C_{60}$ proximity to impurity spins may directly impact the T_{2e}. Nevertheless, Figure 3.9 shows that T_{2e} can be

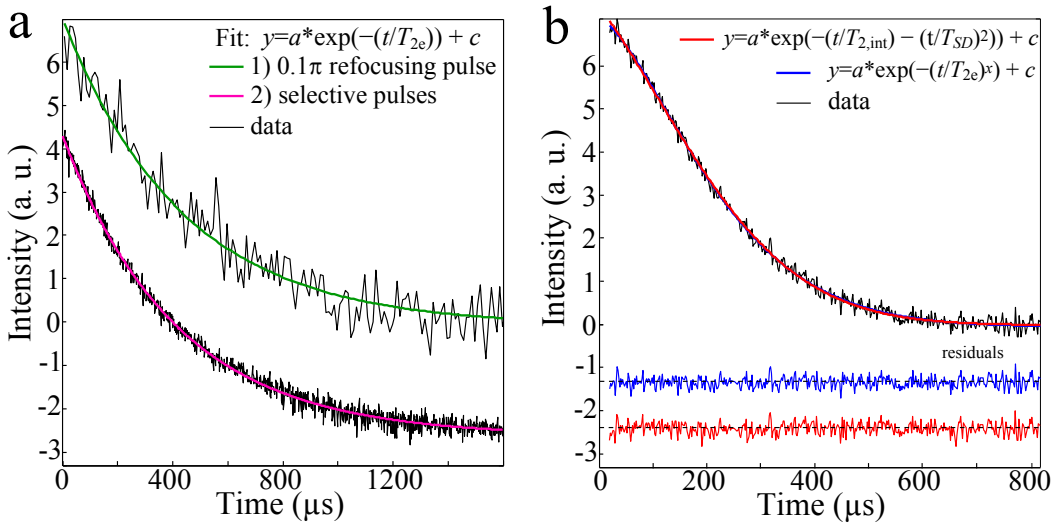

FIGURE 3.10: a) T_{2e} of ^{15}N@C$_{60}$ in a C$_{60}$ matrix with 1) a refocusing pulse of 0.1π and 2) selective 2 μs ($\pi/2$) and 4 μs (π) pulse lengths (axis offset for clarity) b) ^{15}N@C$_{60}$ in a deuterated orthoterphenyl solvent with two different fits to show T_{2e} and the effective T_{2e} if no nuclear spins were present (see text). Residuals to the fits shown offset. All at 40 K.

extended from 190 μs using the standard Hahn echo sequence to an extrapolated $\sim$ 500 μs in the limit $\theta_{2/x} = 0$ (at 40 K), where the material can be considered to be a homogeneously dilute spin system with no dipolar interaction. Considering the experimental data for the lowest turning angle of 0.1π, a T_{2e} of 432.6 ± 26.0 μs is directly shown in Figure 3.10(a,1), the longest T_{2e} recorded, to my knowledge, for a molecular spin system.

3.5.3 ^{15}N@C$_{60}$ decoherence times in a C$_{60}$ matrix: Selective pulses

The long electron decoherence times observed for ^{15}N@C$_{60}$ using a small refocusing angle can be further investigated by using highly selective mw pulses. To give selective narrow frequency excitation, we require long mw pulses that cannot be produced using a travelling wave tube (TWT) amplifier, that is standard on most commercial EPR spectrometers. Using an Amplifier Research 20 W solid state amplifier a mw $\pi/2$ length of 2 μs and a π pulse length of 4 μs can be produced to give a T_{2e} of 413 ± 5.6 μs at 40 K,

as shown in Figure 3.10(a, 2). The long pulses act to excite a statistical distribution of spins (assuming no field gradient is present) and thus mimic a homogeneous dilute sample (sub-ensemble), similar to using a small refocusing angle. The T_{2e} time agrees with the instantaneous diffusion experiment where $\sin^2(\theta/2) < 0.2$, confirming that an alternative decoherence mechanism is also suppressed (to extend T_{2e} by $\sim$100μs). A possible candidate for this mechanism would be the effect of zero field splitting (ZFS), that was shown may be present in the first section of the chapter and Figure 3.8. A fluctuating ZFS will lead to a $D.S_z^2$ term in the Hamiltonian and give rise to two different decoherence contributions given by [CL64, MTA06]:

$$(T_{2e,inner})^{-1} = \frac{4}{5}D^2\left[\frac{\tau_c}{1+\omega_c^2\tau_c^2} + \frac{\tau_c}{4\omega_c^2\tau_c^2}\right] \tag{3.11}$$

$$(T_{2e,outer})^{-1} = \frac{4}{5}D^2\left[\tau_c + \frac{\tau_c}{1+\omega_c^2\tau_c^2}\right] \tag{3.12}$$

where τ_c is the correlation time, ω_c the Lamor frequency, and the subscript *inner* refers to the contribution from the $m_S = +1/2 \leftrightarrow -1/2$ transition and *outer* $m_S = \pm 3/2 \leftrightarrow \pm 3/2$ transition. The contribution from the different coherences have been explored in more detail in the next chapter and it is found that the *outer* levels do not contribute[6] to the Hahn echo signal. This could be due to a fluctuating ZFS term as Eq.3.12 shows that $T_{2e,outer}$ can be limited by this under realistic experimental conditions. However, if a substantial ZFS (static or fluctuating) were present the *outer* levels would not be expected to refocus[7], so the decay of these coherences becomes difficult to ascertain. Therefore, the monoexponential T_{2e} decays observed can be considered due to the *inner* transitions only. The dependence of a fluctuating ZFS term on the *inner* coherence is shown in Eq.3.11. However, at low temperatures the correlation time is long and the contribution to decoherence would be small, therefore, similar to experiments on N@C_{60} in liquid solution (below the fast tumbling limit) [MTA06], ZFS is not expected to have

[6] this could only be shown for $\tau > 70\mu$s due to experimental parameters.

[7] a small proportion could still refocus depending on the Hahn echo τ and ZFS present.

a substantial effect. An alternative mechanism could arise if a distribution of hyperfine parameters was present, as fitted in Figure 3.8, such that the selective pulse excites a homogeneous sub-ensemble of spins with similar hyperfine constants. Kobayashi *et al.* have shown theoretically that modification of the N@C$_{60}$ cage can result in a variation of the hyperfine coupling constant [KND03]. Knapp *et al.* have specifically shown a distribution of isotropic hyperfine parameters in an N@C$_{60}$ powder sample (C$_{60}$ matrix), by comparing the $m_s = 3/2$ and $m_s = 1/2$ ENDOR lines [KWD05]. They attribute this distribution to impurities in the powder sample such as those discussed in the previous section. Therefore, by selecting a narrow hyperfine distribution range through a selective pulse, a homogeneously dilute sub-ensemble of spins can be excited that are not affected by impurity spins, giving a long T_{2e}.

3.5.4 ^{15}N@C$_{60}$ decoherence times in deuterated orthoterphenyl

We can evaluate whether the long ^{15}N@C$_{60}$ decoherence times found in a C$_{60}$ powder effectively give us the intrinsic T_{2e} of the fullerene by preparation of a very different sample using highly purified ^{15}N@C$_{60}$ in a solvent matrix[8]. The section on metallofullerene solvents found deuterated orthoterphenyl to be an excellent solvent: to produce a good glass at low temperatures and probe T_{2e} without the effect of decoherence due to matrix nuclear spins. Preparing a degassed sample in the same way outlined in Section 3.2.4 and measuring the decoherence time a stretched exponential curve, Eq. 3.2, is given indicative of a T_{2e} limited by spectral diffusion due to solvent matrix nuclei. At 40 K a T_{2e} of 249.2$\pm$2.8 μs is found with a stretch factor, x, of 1.5 as shown in Figure 3.10 (b). The decoherence time for an ^{15}N@C$_{60}$ sample in the absence of nuclear spins, such as within a solid state sample, can be found by using an alternative fit shown in Eq. 3.5. Using this equation a $T_{2e,int}$ of 431$\pm$34.5 μs is found where T_{SD} is 366$\pm$14.8 μs at 40 K, also shown in Figure 3.10. This is entirely consistent with the decoherence times found in Section 3.5.2 and Section 3.5.3 in excess of 400 μs, suggesting that we have identified the intrinsic and thus maximum T_{2e} of ^{15}N@C$_{60}$, that can be achieved using standard

[8]this should contain fewer impurities.

characteristic techniques and materials. The fundamental limit for T_{2e} is twice T_{1e}, which is clearly significantly higher than the intrinsic T_{2e}. The limiting mechanism for T_{2e} is unknown but identifying and understanding this could lead to novel techniques or materials in order to reach this higher fundamental limit in the future. Candidate mechanisms could arise from the movement of the nitrogen atom within the cage that could lead to fluctuations in the hyperfine terms of the Hamiltonian. This mechanism is realistic given the next section, where we shall see that atom-cage vibrational modes appear to cause T_{1e} relaxation.

3.5.5 $^{15}N@C_{60}$ relaxation times in a C_{60} matrix

The relaxation times for $^{14}N@C_{60}$ in CS_2 and toluene have been shown to follow an Arrhenius or Orbach two phonon dependence over the temperature range 160–290 K [Mor05b, MTA06, MTA07]. This follows Eq. 3.6 with an energy difference to the excited state (Δ) given by the first and second Raman cage vibrational modes, respectively, for CS_2 and toluene. At lower temperatures long $N@C_{60}$ T_{1e} times have been reported [Mor05b, Mor05a, MTA07, Har02] but relaxation has not been found to follow these vibrational modes and no explanation for this has been given [MTA07]. Figure 3.11 shows the experimental T_{1e} data for our $^{15}N@C_{60}$ in C_{60} sample, plotted with an Arrhenius temperature dependence and yielding an extracted vibrational mode of 74.2 ± 3.7 cm^{-1} over the range 15–80 K.

This is much lower in frequency than the higher temperature vibrational modes previously reported. In Section 3.3 we found that at low temperatures the vibrational modes of metal atoms encapsulated in fullerene cages could describe the Arrhenius temperature dependence of T_{1e}, an observation consolidated by frequency agreement with Raman and x-ray powder measurements. It therefore seems possible that nitrogen atom-cage vibrations may also be the dominant T_{1e} relaxation mechanism at low temperatures. This would be consistent with a simple atom-cage linear oscillator model whereby the vibrational frequency (ν) is proportional to $\mu^{-1/2}$ such that the lighter ^{15}N

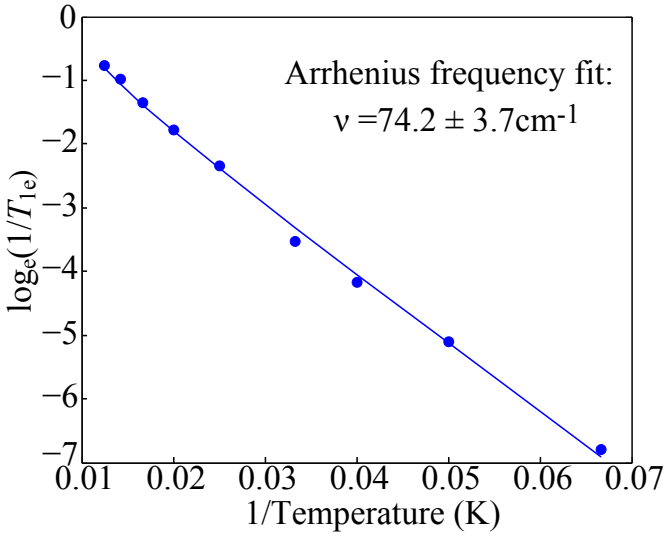

FIGURE 3.11: T_{1e}, in the range 15–80 K, plotted with an Arrhenius style temperature dependence and fitted to Eq. 3.6 with a frequency of 74.2 ± 3.7 cm^{-1}.

atom has a higher vibrational frequency than the much heavier metal atoms in metallofullerenes. Similarly, the charge transfer from the ^{15}N atom to the C$_{60}$ cage is much weaker than in metallofullerenes, again predicting a higher vibrational frequency. The extracted ^{15}N@C$_{60}$ vibrational mode is affected by both higher vibrational modes and relaxation mechanisms, as well as the deviation from an Arrhenius dependence that was found below ∼15 K. This low temperature deviation is not understood but was also observed in metallofullerenes. Adding previously extracted vibrational modes to the T_{1e} fit (i.e. two mechanisms) did not significantly change the extracted frequency. Low temperature Raman data for N@C$_{60}$ is not available in literature[9] so comparison to the extracted vibrational mode is not possible, but density functional theory (DFT) calculations for ^{14}N@C$_{60}$ predicted vibrational modes to be around 50 cm^{-1}, a little lower than that extracted by our data [KM]. It is therefore probable that relaxation at low temperatures is dominated by atom-cage vibrational modes for ^{15}N@C$_{60}$ (in C$_{60}$) as well as metallofullerenes (over ∼15–100 K). This will have a direct impact on the maximum nuclear decoherence time that can be achieved in the N@C$_{60}$ system which we shall investigate in Chapter 4 and Chapter 5.

[9]Nitrogen encapsulated in a fullerene cage is both air and light sensitive so this would be challenging.

4

Coherent transfer between the electron and nuclear spin state

4.1 Introduction

In the previous section we explored the characteristic electron spin times for fullerene based materials. However, many proposals, such as those discussed in Section 1.3.3 and Section 1.3.4, exploit both the electron and nuclear spin properties of the system. The principle advantage of this is that the weaker magnetic moment of a nuclear spin, compared to an electrons spin, can give a longer coherence time. Nuclear magnetic resonance (NMR) can be used to exploit the nuclear spin qubit and extract nuclear

coherence times, but not at low spin concentrations. Using EPR, nuclear spin properties can be probed via the electron spin state at lower spin concentrations, for instance, using ENDOR as described in the next section. However, utilising the nuclear spin to store quantum information is more difficult and requires coherent transfer of electron to nuclear spin states, which has been implemented in only a handful of systems, as discussed in Section 1.5. An ideal material to initially show this transfer is Si:P as the long electron decoherence times (with fast manipulation) can be used for processing and the longer nuclear decoherence times as a memory. The Si:P system has also been relatively well characterised and has a simple electron spin-1/2, nuclear spin-1/2 level structure. The chapter will then explore the coherent transfer in a very different molecular high spin $^{15}N@C_{60}$ system (electron spin-3/2), exploiting the propagation to also turn on and off inter-qubit dipolar interactions.

4.2 Coherent state transfer in Si:P

4.2.1 The Si:P system and ENDOR

The Si:P level structure is shown in Figure 4.1(a) with transitions that can be addressed by resonant rf and mw pulses, to perform gate operations as outlined in Section 1.4.2. The electron spin-1/2 is coupled to the nuclear spin-1/2 via an anisotropic hyperfine constant, $A = 117$ MHz, and at $\sim 0.35\ T$ gives an EPR doublet corresponding to the $m_I = \pm 1/2$ transitions. To achieve high fidelity coherent state transfer we require a Si:P system with narrow spectral features that can be fully excited by the appropriate mw or rf pulses. The experiments therefore use ^{28}Si enriched single crystals with a residual ^{29}Si concentration of 800 ppm. This avoids broadening of the rf lines due to ^{29}Si or biaxial stress induced by use of epilayer samples [ATT10]. The Si:P crystals were produced by decomposing isotopically enriched silane in a recirculating reactor to produce poly-Si rods, followed by floating zone crystallisation, with further details found in Ager *et al.* [ABH05]. To observe the frequency and spectral width of the nuclear transitions

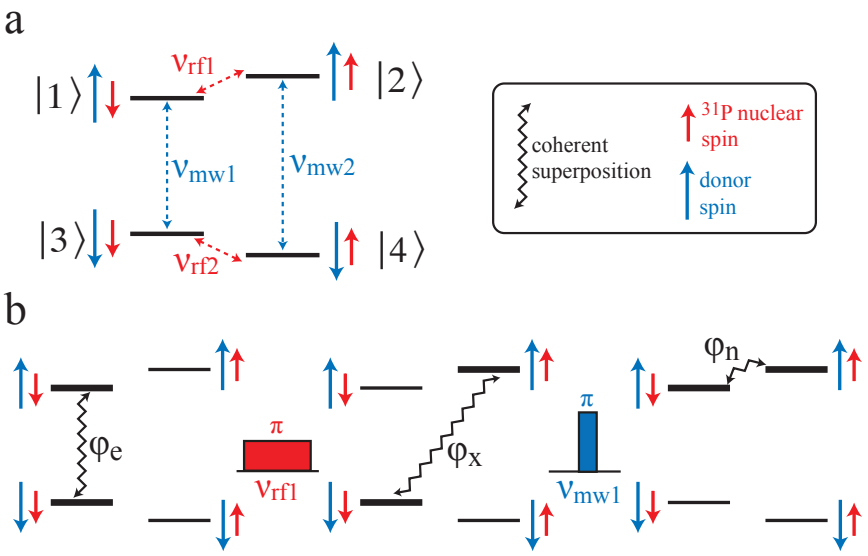

Figure 4.1: a) Energy level diagram for Si:P with the electron spin (1/2) and nuclear spin (1/2) represented by the blue and red arrows, respectively. The rf frequencies under an applied field of $\sim 0.35\ T$ are at approximately 52.4 and 65.1 MHz for the $m_S = -1/2$ and 1/2 transitions, respectively. b) Coherent transfer of an electron spin coherence (represented by the oscillatory line) to a nuclear spin coherence via the mw and rf transitions shown.

electron nuclear double resonance (ENDOR) must be performed. ENDOR sequences probe the nuclear spin via the electron spin state, with Davies ENDOR a particularly suitable scheme for this system (large hyperfine splitting) [SJ01d]. A typical sequence is as follows: $\pi_{mw:1,3} - \pi_{rf:1,2} - \pi/2_{mw:1,3} - \pi_{mw:1,3}$, where the subscript indicates the pulse frequency and the transition it addresses, though typically the rf frequency is swept to find resonance[1]. The initial mw pulse acts to invert the electron spin population with the resonant rf π pulse swapping the population between levels $|1\rangle$ and $|2\rangle$. This results in a reduction in the inverted electron spin echo intensity observed as the $|1\rangle : |3\rangle$ populations are equalised, shown at ~65 MHz in Figure 4.2. If the rf pulse fully excites the transition and all population is swapped between levels $|1\rangle$ and $|2\rangle$, then there will be no population difference between levels $|1\rangle : |3\rangle$ and hence no electron spin echo will be observed. In general ENDOR experiments, the ENDOR efficiency, F_{ENDOR}, is characterised by the change in an observed electron spin echo intensity I_{ESE} resulting

[1]Typically 80 ns mw and 10 μs rf π pulses are used for this and the remaining sequences in this thesis.

from a resonant rf pulse:

$$F_{\text{ENDOR}} = \frac{I_{\text{ESE}}(\text{no rf}) - I_{\text{ESE}}(\text{rf})}{2I_{\text{ESE}}(\text{no rf})} \tag{4.1}$$

Thus, for the experiment described $F_{\text{ENDOR}} = 0.5$ (where F_{ENDOR} ranges from 0 to a maximum value of 1). Re-thermalising the system is crucial for this sequence to work and thus the build up of polarisation in one nuclear subspace due to long $T_{1\text{n}}$ times must be avoided. This can be achieved by either a very long shot repetition time (srt) or more conveniently a $\pi_{rf:1,2}$ pulse at the end of the Davies sequence to 'tidy' the polarisation [TMAL06].

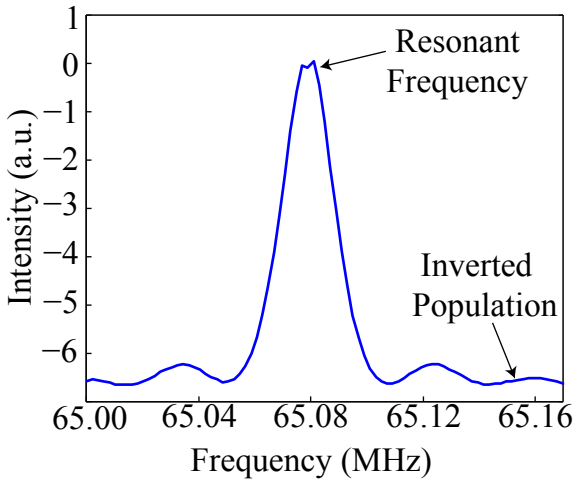

FIGURE 4.2: Si:P Davies ENDOR on the $m_S = 1/2$ transition. The baseline (inverted spin echo) shape reflects the pulse excitation profile. A 'tidy' pulse is used to prevent polarisation build up 'shot-to-shot'.

4.2.2 Directly probing the nuclear spin

Having found the nuclear transitions using ENDOR we can coherently transfer or 'write' electron spin states to the nuclear spin state using the sequence shown in Figure 4.1(b). The initial mw pulse creates an electron coherence ('qubit') of an arbitrary phase φ_e, this is then transferred to a double quantum coherence (DQC)[2], φ_x, using a resonant rf π pulse. A final mw π pulse subsequently transfers the coherence to a

[2]This can also be referred to as a pseudo-entangled state between an electron and nuclear spin.

nuclear spin state, φ_n, where it can be held for the nuclear coherence time T_{2n} as investigated in Chapter 5. In terms of quantum gate operations discussed in Section 1.4.1 and Section 1.4.2 the two π pulses in the 'write' process can be considered as c-NOT gates (with some additional phase that can be ignored). As the π pulses are selective on a manifold these two c-NOT gates then constitute a SWAP gate. To validate the transfer scheme the nuclear spin state can be probed by mapping it to an electron polarisation via an rf $\pi/2$ pulse, similar to a Ramsey fringe experiment. The rf $\pi/2$ pulse can then be swept across the nuclear spin echo in order to achieve state readout as an electron Hahn echo, as shown in Figure 4.3. In this figure the rf frequency has been set off-resonance in order to more clearly see the phase of the recovered echo and additional pulses have been added to refocus the effect of inhomogeneity in the system. By varying the phase of the initial electron state the same phase is recovered from the nuclear spin state, showing that the coherent transfer scheme works.

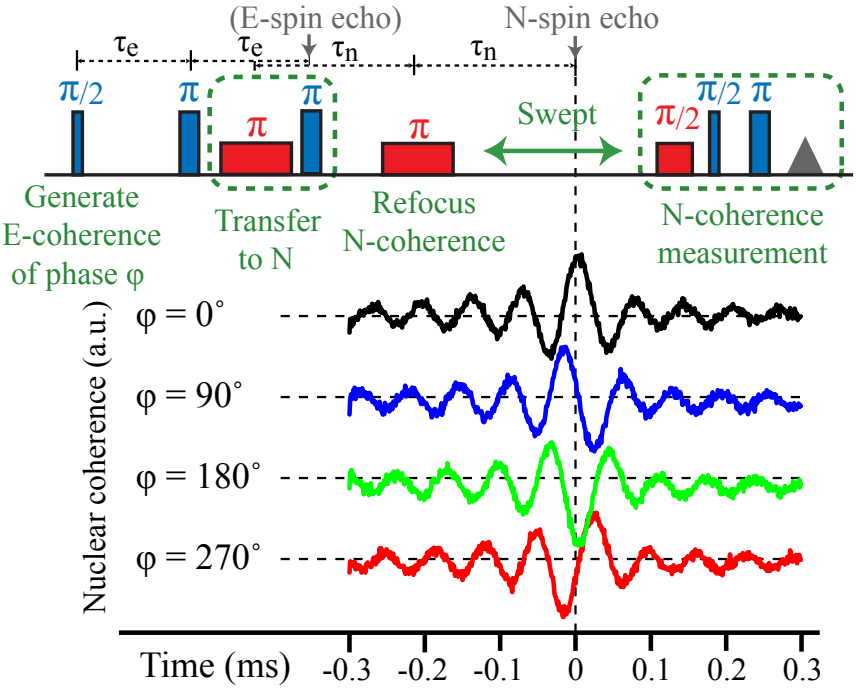

Figure 4.3: Coherent transfer of electron spin states of phase 0°, 90°, 180° and 270°, to the nuclear spin state. The state is directly probed via polarisation transfer to the electron spin and readout using an electron spin echo. The nuclear frequency is set off resonance to observe the state phase more easily. Mw frequency pulses are shown in blue and rf pulses in red.

4.2.3 Transfer of electron to nuclear spin states

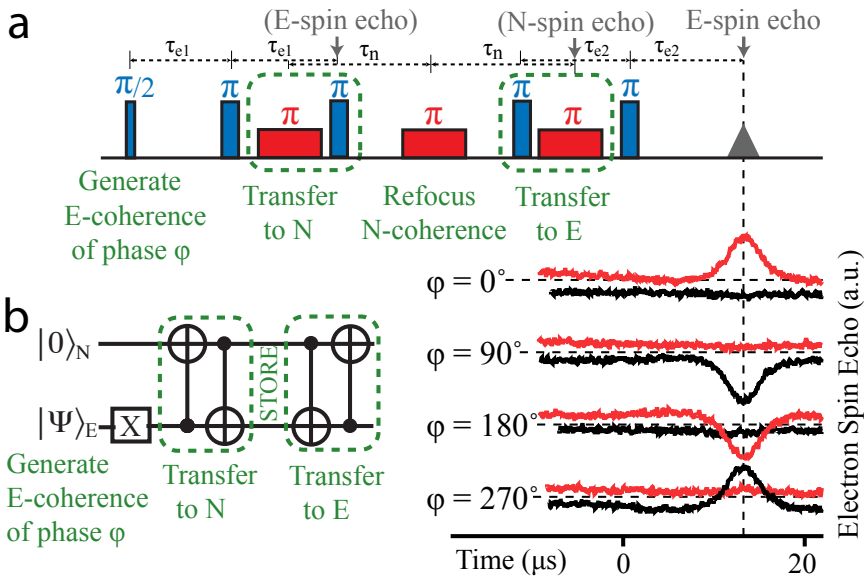

FIGURE 4.4: a) Coherent transfer of electron spin states of phase 0°, 90°, 180° and 270°, to the nuclear spin state and back with readout via an electron spin echo. Inset (b): the quantum logic circuit for the transfer process, two c-NOT gates on a specific nuclear subspace are required to SWAP the qubit state.

Probing the nuclear spin has shown that an electron spin state can be successfully written to a nuclear spin state. However, for this to be useful we need to be able to not only coherently transfer a qubit to the nuclear state but also recover this in a non-destructive way. A pulse scheme can be envisaged which uses the exact opposite of the transfer to the nuclear spin state to return the qubit state for readout using the electron spin, shown in Figure 4.4. The additional refocusing pulses in this sequence can be considered in more detail, being specifically placed to improve the transfer fidelity. The ensemble of spin states will be subject to inhomogeneous broadening as each individual spin is subject to slightly different mw and rf fields, see Chapter 2. Thus, electrons spins will be detuned from the resonant mw frequency by δ_e, whereas nuclear spins are detuned from the rf resonant frequency by δ_n (in the appropriate reference frame). During the time $\tau_{e,1}$ in the sequence the electron spin state will acquire phase δ_e but using a π mw pulse this phase will be 'unwound' during the second $\tau_{e,1}$. Therefore, by placing the mw pulse that writes the coherence fully to the nuclear spin state at

the end of the second $\tau_{e,1}$, a state completely refocused from electronic inhomogeneous broadening is transferred. Before transfer to the nuclear spin state the qubit is held as a DQC which will also acquire phase δ_n (overall $\delta_e + \delta_n$). To remove the phase, δ_n, acquired whilst in the DQC and nuclear spin states, τ_n can be made equal in length either side of an rf refocusing pulse. Thus, the experiment removes the effect of inhomogeneous broadening, where $\pi/\delta_e \approx 2\mu$s and $\pi/\delta_n \approx 100\mu$s. The scheme will also work without π_{mw} refocusing pulses due to the symmetry of the sequence but will be susceptible to magnetic field noise. Figure 4.4 shows that electron spin states of 0°, 90°, 180° and 270° can be faithfully written to the nuclear spin and recovered for electron spin read-out. The success of the scheme can be directly shown by storing the qubit for $\tau_n \gg T_{2e}$, such that all state information recovered must have been held in the nuclear spin subspace. The sequence therefore produces a functioning quantum nuclear memory with the quantum logic circuit shown in Figure 4.4(b, inset).

4.2.4 Transfer fidelity

We have shown that a quantum nuclear memory can be successfully implemented in Si:P. However, ultimately for the memory to be advantageous a high two-way transfer fidelity is required otherwise quantum information will be lost during the transfer process, rendering the memory useless. To achieve a high fidelity: pulses must fully excite the spin transitions requiring careful selection of material as commented upon in Section 4.2.1; the mw and rf sources do not need to be phase locked (as phase differences are cancelled out across the scheme) but they must have high phase stability and dephasing of the system must be refocused, as previously discussed. The fidelity can be assessed by preparing specific quantum states and comparing the recovered state (ρ_1) with a reference state prepared in the same way (ρ_0), as shown in Figure 4.5. The initial states are prepared by: varying the phase of the initial $\pi/2$ mw pulse for $\pm$X and $\pm$Y; application of a π pulse for +Z; a π pulse followed by a wait time of $\ln(2)T_{1e}$ for the Identity and no initial pulse for the $-$Z state. The reference state then uses a Hahn echo readout with the same $\tau = \tau_{e2}$ as the recovered state, which also

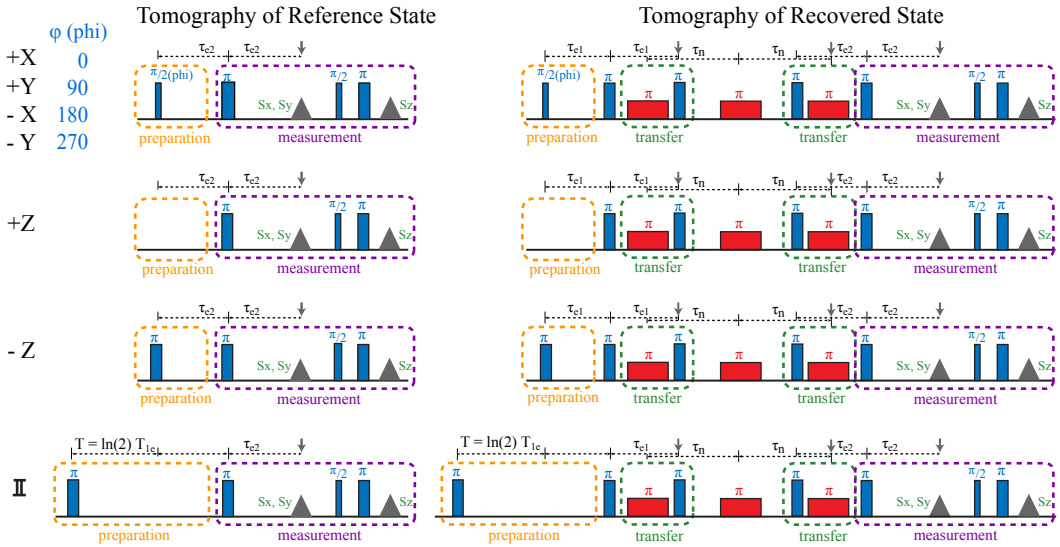

FIGURE 4.5: EPR sequences to generate the states $\pm X, \pm Y, \pm Z$ and $\mathbb{I}$, with readout in the σ_x, σ_y and σ_z basis. The reference sequences use a simple Hahn echo readout and the recovered sequences transfer the states to the nuclear spin manifold and back.

employs storage in the nuclear spin. The two states are assessed by observing the in-phase and quadrature components (σ_x, σ_y basis) from the electron spin echo readout. The σ_z basis is recovered by applying a final $\pi/2$ pulse to return the coherence to a population, followed by a Hahn echo readout. Crucially, this is performed a short time after the σ_x, σ_y basis measurement, with a Hahn echo $\tau \ll T_{1e}$, to prevent any relaxation that would lead to inaccuracies in the final reduced density matrix.

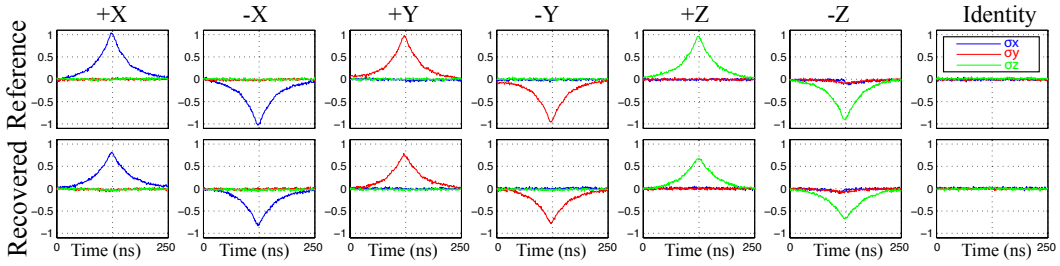

FIGURE 4.6: The reference and recovered echoes from the sequences in Figure 4.5. The σ_x, σ_y echoes occur simultaneously whilst the σ_z echo is superimposed for clarity.

The reference and recovered echoes are shown in Figure 4.14 in the σ_x, σ_y and σ_z basis. The reference states are assumed to be pure and are integrated (to give $A_{x,y,z}$) and normalised. This is used to obtain the state density matrix tomography shown

in Figure 4.7, where the normalisation is given by:

$$\rho = \frac{A_x\sigma_x + A_y\sigma_y + A_z\sigma_z}{2\sqrt{A_x^2 + A_y^2 + A_z^2}} + \mathbb{I}/2 \tag{4.2}$$

The recovered states are not normalised with respect to a pure state but rather compared to the reference states. The fidelity, F, of the transfer process for the seven states can be extracted using the convention $F = \langle\psi|\rho_1|\psi\rangle$, where $\rho_0 = |\psi\rangle\langle\psi|$, which is common in QIP literature [NC00a]. The exact two-way transfer fidelities are shown in Figure 4.7 of approximately 90% for an arbitrary qubit state between the electron and nuclear spin degree of freedom. The loss in fidelity is attributed to pulse error of ∼5% over the seven pulse in the transfer sequence, consistent with previous observations [MTA05a]. The fidelity of the sequence can be improved by replacing each of the microwave pulses with a composite BB1 error correcting microwave pulse [CLJ03, MTA05a]. A π pulse is optimised with the error correcting sequence $\pi(0°)$-$\pi(104.5°)$-$2\pi(313.4°)$-$\pi(104.5°)$, where brackets indicate the axis of rotation in degrees. Applying this to both the reference and full transfer sequence for the +X state, a fidelity of 97% is achieved. If BB1 pulses or other error correcting sequences were to be applied to the rf transitions a similar improvement would be expected, thus giving near perfect fidelity.

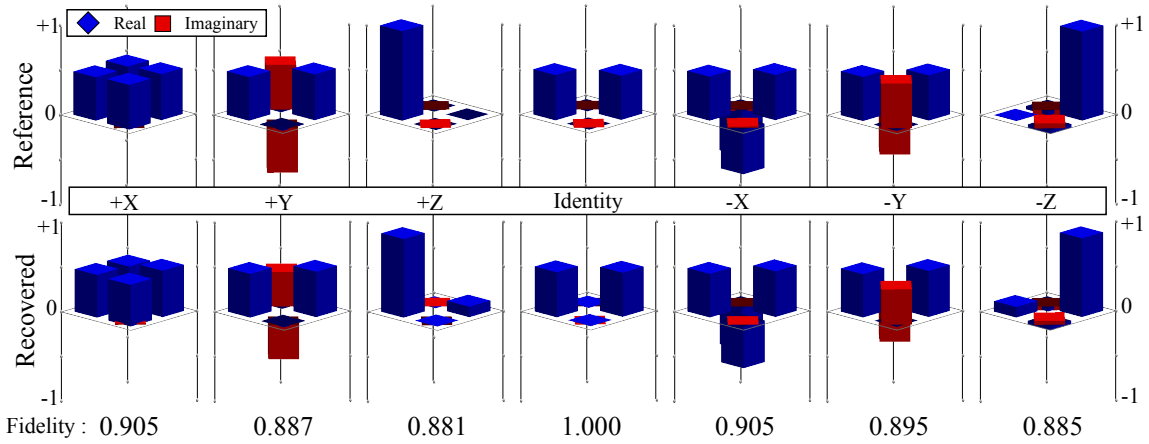

Figure 4.7: The density matrix tomography for the states $\pm X, \pm Y, \pm Z$ and $\mathbb{I}$ in the σ_x, σ_y and σ_z basis before (reference) and after (recovered) storage within the nuclear spin state.

4.2.5 Process tomography

Having assessed the fidelity for the transfer of individual quantum states, one can perform process tomography to obtain a process matrix and fidelity for the transfer scheme [NC00b]. If the states $|\psi_j\rangle$ are prepared, then performing the process operation will give the output $\mathcal{E}(|\psi_j\rangle\langle\psi_j|)$, where $\mathcal{E}$ is the quantum operator. To determine this experimentally a set of operation elements, $\{E_i\}$, can be considered for $\mathcal{E}$, such that $\mathcal{E}(\rho) = \sum E_i \rho E_i^\dagger$. However, experimental results will be numerical rather than operators and thus we can alternatively represent $\mathcal{E}$ using a fixed set of operators $\tilde{E}_i$, where $E_i = \sum_m e_{im}\tilde{E}_m$, and e_{im} is a set of complex quantum numbers. This will then give:

$$\mathcal{E}(\rho) = \sum_{mn} \tilde{E_m}\rho\tilde{E_n}^\dagger \chi_{mn} \tag{4.3}$$

where χ_{mn} is a complex number matrix that can completely describe $\mathcal{E}$ for a fixed set of operators, $\tilde{E}_i$. To obtain the χ matrix for a one qubit operation four operators are required to give the matrices: $\rho'_1 = +\mathrm{Z}$; $\rho'_4 = -\mathrm{Z}$; $\rho'_+ = +\mathrm{X}$ and $\rho'_- = +\mathrm{Y}$, all of which were obtained in the previous section. ρ'_2 and ρ'_3 are then further given by: $\rho'_2 = \rho'_+ - i\rho'_- - (0.5 \times (1-i)(\rho'_+ + \rho'_-)$ and $\rho'_3 = \rho'_+ + i\rho'_- - (0.5 \times (1-i)(\rho'_+ + \rho'_-)$, respectively. Using these the χ matrix can then be extracted according to the equation:

$$\chi = \lambda \begin{bmatrix} \rho'_1 & \rho'_2 \\ \rho'_3 & \rho'_4 \end{bmatrix} \lambda. \tag{4.4}$$

where,

$$\lambda = \frac{1}{2}\begin{bmatrix} \mathbb{I} & \sigma_x \\ \sigma_x & -\mathbb{I} \end{bmatrix}. \tag{4.5}$$

We actually require the process tomography to be compared not to an ideal χ matrix but to an initial or reference χ matrix, similar to Section 4.2.4. This can be found given the reference and recovered χ matrices and solving a series of linear equations. The χ matrix is shown in Figure 4.8, representing the process tomography for the coherent transfer of quantum information between electron and nuclear spin states. The fidelity

of the operation is shown by the element $\langle\hat{\mathbb{I}},\hat{\mathbb{I}}\rangle$, which if the transfer is perfect will be the $\mathbb{I}$ operation (unity). The element shows a fidelity of 84%, compared to a perfect $\mathbb{I}$, a little lower than the individual state fidelities.

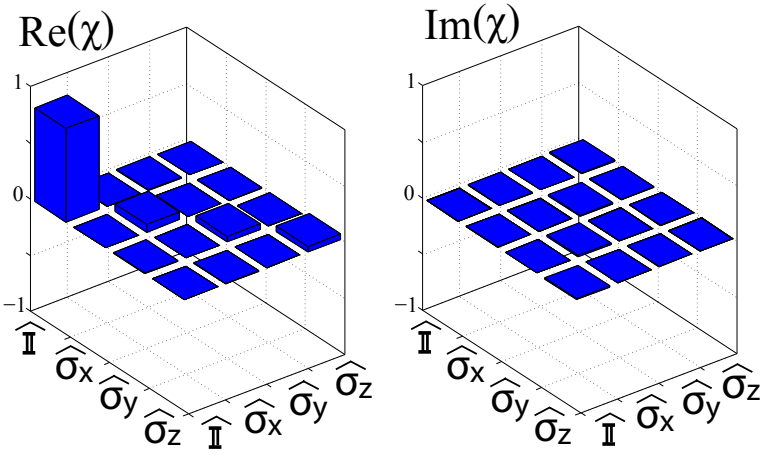

Figure 4.8: Quantum process tomography matrix (χ) for the transfer of a qubit state from the electron to the nuclear degree of freedom and back, in the basis ($\mathbb{I}$, σ_x, σ_y, σ_z). χ is evaluated given reference and recovered matrices and gives a fidelity compared to a perfect $\mathbb{I}$ of 0.84.

4.3 Coherent transfer in $^{15}N@C_{60}$

4.3.1 The $^{15}N@C_{60}$ system

The electron spin properties of $^{15}N@C_{60}$ in a C_{60} matrix were explored in Section 4.3.1 and showed both long T_{2e} and T_{1e} times. In Si:P, these properties allowed the nuclear spin to also be exploited through coherent transfer in a simple four level solid state system. In contrast, $^{15}N@C_{60}$ is a molecular, high-spin, eight level system as shown in Figure 4.9 and therefore requires a different approach. The system consists of an $S = 3/2$ electron spin coupled via an isotropic hyperfine interaction (Eq. 3.1) of 22 MHz to the ^{15}N nuclear spin ($I = 1/2$). Under an applied magnetic field of $\sim 0.35\ T$ this produces a doublet in the electron spin resonance (ESR) spectrum where each line corresponds to a state of m_I [MVTA07]. To first order, the three electron $\Delta m_S = 1$ transitions in each m_I subspace have the same energy and cannot be addressed

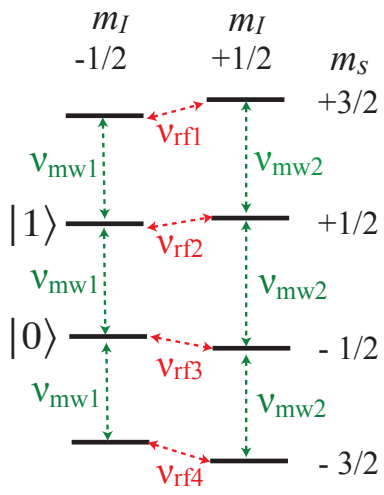

FIGURE 4.9: The coupled electron spin ($S = 3/2$), nuclear spin ($I = 1/2$) system for ^{15}N@C$_{60}$ leads to 8 levels. A qubit can be represented across an electron spin transition where $m_I = -1/2$, $m_S = \pm 1/2$ are denoted states $|0\rangle$ and $|1\rangle$. Transitions can be addressed via resonant microwave (mw) and radiofrequency (rf) pulses (typically π=80 ns and 10 μs, respectively). The rf frequencies under an applied field of ~ 0.35 T are at approximately 9.6, 12.4, 31.6 and 34.5 MHz for the transitions $m_s = 1/2, -1/2, 3/2$ and $-3/2$, respectively.

individually [MTA05b]. Thus a $\pi/2$ ESR pulse (selective on one m_I state) produces coherences across all three pairs of levels (with $\Delta m_S = 1$). For convenience, we will refer to an electron coherence between m_S levels $+1/2 : -1/2$ as an *inner* coherence, and those between m_S levels $\pm 3/2 : \pm 1/2$ as *outer* coherences. A qubit could be represented by any of the pairs of levels in the system but we specifically define the qubit between the *inner* pair of m_S levels, in the subspace of $m_I = -1/2$ (see Figure 4.9).

4.3.2 Coherence transfer ENDOR

To understand the ^{15}N@C$_{60}$ system we need to probe the contributions from the different electron spin levels and find the nuclear spin transition frequencies. Using Si:P, we introduced Davies ENDOR as an appropriate tool to locate the rf resonances but it is found that this is not appropriate for the $m_S = \pm 1/2$ levels in the N@C$_{60}$ system (summarised in Ref [Mor05b]). An alternative scheme utilises a Hahn echo sequence with the addition of resonant rf pulses to remove or impart phase shifts of coherences, known as 'coherence transfer' ENDOR [SJ01e]. A simple sequence is described by

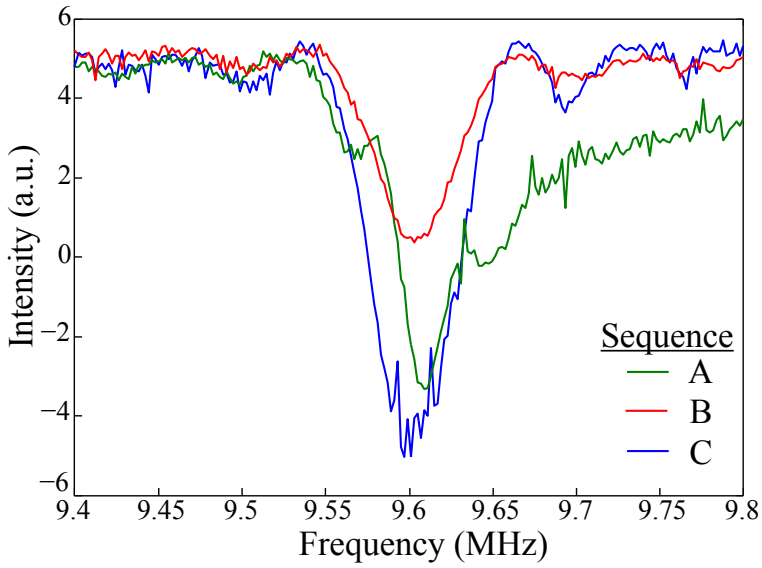

Figure 4.10: Coherence transfer experiments using the sequences outlined in Table 4.1, conducted on the $m_I = +1/2$ transitions at 40 K. Sequence A shows an additional broad feature due to the Bloch-Siegert shift [SJ01e], this is eliminated by using sequence B — typically used to find the rf transition frequency, for instance, as required in the next section.

$\pi/2_{mw} - 2\pi_{rf} - \pi_{mw} - echo$ (Table 4.1 (A)), whereby the rf 2π pulse imparts a π phase shift on an electron spin coherence and the signal (in a electron spin-1/2 system) varies from a relative $+1 \rightarrow -1$ or $F_{\text{ENDOR}} = 1$ (where $F_{\text{ENDOR}} = 1$ is the maximum coherence information available). Thus, by sweeping the rf field the resonant transition can be found. An electron spin-3/2 system differs from a spin-1/2 system as the rf pulse can affect either the *outer* electron coherences, $m_S = \pm 3/2$, or both *outer* and *inner* electron coherences, $m_S = \pm 1/2$. Thus, a series of experiments, shown in Table 4.1, can be envisaged in order to not only find the rf transition but once on resonance, ascertain the contribution from the *outer* coherences to the Hahn echo intensity.

Sequence	RF(i)	RF(ii)
A	$2\pi_x$	0
B	π_x	π_x
C	$\pi_x\pi_y$	$\pi_y\pi_x$

Table 4.1: Coherence transfer experiments using $\pi/2_{mw} - RF(i) - \pi_{mw} - RF(ii) - echo$. In the table the pulse subscript indicates the axis rotation. In experiments (B) and (C) the splitting of the rf pulse, i.e. an rf π pulse before and after the mw refocusing pulse, avoids the Bloch-Siegert shift. In (C) the rf pulses with differing axis of rotation, $\pi_x\pi_y$, act to induce a $\pi/2$ phase shift on the electron spin echo.

Table 4.2 shows the theoretical results of the sequences outlined in Table 4.1 under two scenarios: i) all coherences contribute to the echo observed, and ii) only the *inner* coherence contribute. The experimental results are shown to be entirely consistent with the latter case. Therefore, using any of the sequences and sweeping the rf field, the $m_S \pm 1/2$ transitions can be found (typically sequence B is used with $F_{\mathrm{ENDOR}} = 0.5$) which are required for the coherent transfer sequence to be implemented. It also means that the initial reference echoes generated using a Hahn echo sequence such as in Figure 4.5 (for Si:P) can still be used to compare the fidelity of the transfer process. This is because there cannot be any contribution from *outer* coherences (which are not transferred) to this reference echo, on the timescale of 70 μs, which is less than the Hahn echo τ of 140 μs .

RF resonant	Sequence A (F_{ENDOR})		
(m_S)	all coh.	inner only	Exp.
$\pm 1/2$	0.7	1	0.936(1)
$\pm 3/2$	0.3	0	0.00000(8)
RF resonant	Sequence B (F_{ENDOR})		
(m_S)	all coh.	inner only	Exp.
$\pm 1/2$	0.5	0.5	0.4786(9)
$\pm 3/2$	0.3	0	0.00000(7)
RF resonant	Sequence C (F_{ENDOR})		
(m_S)	all coh.	inner only	Exp.
$\pm 1/2$	0.7(X):0.3(Y)	1	0.990(1)
$\pm 3/2$	0.3(X):0.3(Y)	0	0.00000(6)

Table 4.2: Coherence transfer experiments using the sequences outlined in Table 4.1, conducted on the $m_S = +3/2$ and $+1/2$ transitions ($m_I = +1/2$), are compared with two theoretical scenarios: one in which the observed electron spin echo contains maximum contribution from all coherences ('all coh.') and a second in which only the inner coherences contribute to the echo ('inner only'). Brackets indicate the phase of the signal (split between the X and Y channels of the quadrature detector). The experimental results are consistent with the expected contribution if no *outer* coherence is observed on the timescale of 70 μs.

4.3.3 Transfer of electron to nuclear spin states

Having obtained the $m_S \pm 1/2$ nuclear transition frequencies using coherence transfer ENDOR, electron spin states can be coherently transferred to the $m_S \pm 1/2$ nuclear spin states. A sequence similar to that applied to Si:P can be used but it is complicated by the $S = 3/2$ electron spin, such that the initial $\pi/2$ mw pulse produces both an *inner* coherence and unwanted *outer* coherences, as shown in Figure 4.11.

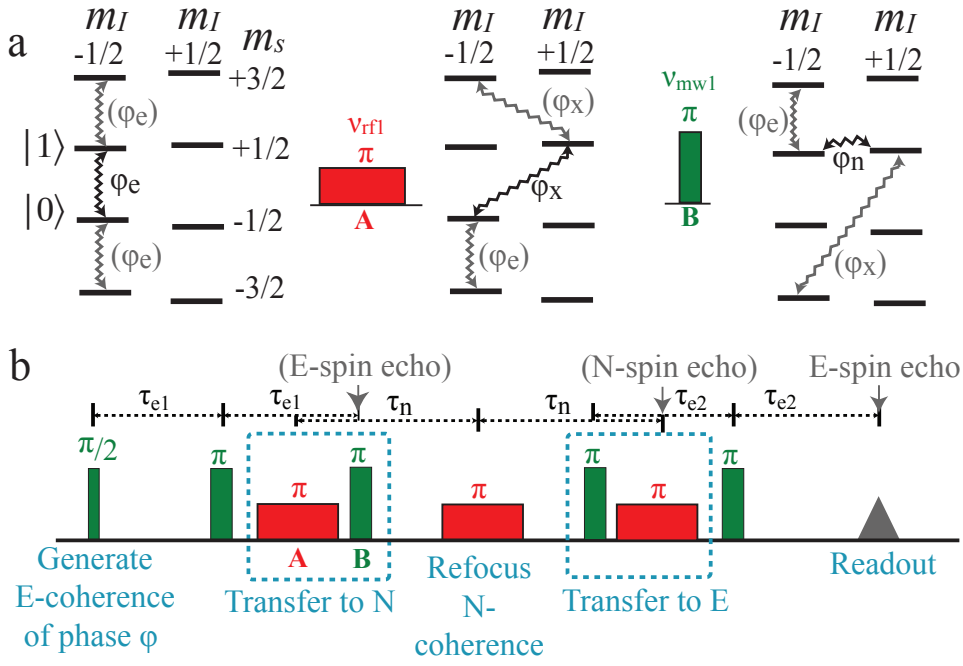

Figure 4.11: a) Transfer of a qubit state from an electron spin degree of freedom to the ^{15}N nuclear spin, within the $m_S = +\frac{1}{2}$ subspace. Coherences are depicted by zig-zag lines and 'unwanted' coherences generated by the initial $\pi/2$ pulse on the $S = 3/2$ electron spin are shown in grey. At the end of the transfer sequence, such coherences will decay on the timescale of T_{2e} or faster, while the stored qubit will lose coherence on the timescale of T_{2n}. b) The full two-way transfer sequence.

The general scheme works in the same way, using an rf π pulse on the $m_S = +1/2$ transition (a c-NOT in quantum gate terminology) then transferring the qubit to an electron-nuclear cross coherence (φ_x). A mw π pulse selective on $m_I = -1/2$ then completes the SWAP operation to produce a nuclear coherence (φ_n). Unwanted *outer* coherences generated during the sequence remain as both electron- and multiple-quantum coherences, which will decay on the timescale of the electron spin decoherence time

(T_{2e}) or faster as shown[3] in Section 4.1. The desired nuclear spin coherence can then be stored for many milliseconds before transfer back to the electron spin via a reverse of the sequence and readout by a conventional electron spin (Hahn) echo.

4.3.4 Labelling the nuclear transition

In the Si:P experiments we showed that coherent transfer sequence worked by directly probing the nuclear spin state, Section 4.2.2. This sequence can not be implemented using high spin $^{15}N@C_{60}$. We must therefore use an alternative method to confirm that the recovered electron spin echo arises solely from a state that was stored in a nuclear spin degree of freedom. One such method is to apply a time-varying phase shift to the nuclear spin and observe a corresponding phase shift in the electron spin echo [Höf96]. To apply this phase we employ a geometric phase gate similar to that of Aharonov-Anandan gate [AA87, SMP88], consisting of two resonant π rf pulses which will be invariant to spin populations. Varying the phase of the second rf pulse relative to the first by $\delta\phi$, the nuclear spin qubit undergoes a path around the Bloch sphere, resulting in a geometric phase. In the basis $(m_S, m_I) = [(1/2, 1/2), (-1/2, 1/2), (1/2, -1/2), (-1/2, -1/2)]$ a π_0 followed by a π_ϕ pulse (where the subscript indicates the phase) applies a phase of 2ϕ to the nuclear coherence, given by the operator:

$$U(\phi) = \begin{pmatrix} e^{i\phi} & 0 & 0 & 0 \\ 0 & 1 & 0 & 0 \\ 0 & 0 & e^{-i\phi} & 0 \\ 0 & 0 & 0 & 1 \end{pmatrix} \tag{4.6}$$

Experimentally this is implemented by applying the two rf pulses immediately after the refocusing rf pulse (see Figure 4.11(b)) and incrementing the phase of the second using a using a Rohde and Schwarz AFQ 100B. A Fourier transform of the phase-incremented

[3]The shorter *outer* decoherence time shown in this section has been refocused in a Hahn echo. The previous chapter showed a ZFS may be present in the sample so it may be that the decoherence times of the *outer* coherence are long but that they cannot be refocused due to shifts in the energy levels. In this case it would be difficult to measure the T_{2e} of these transitions.

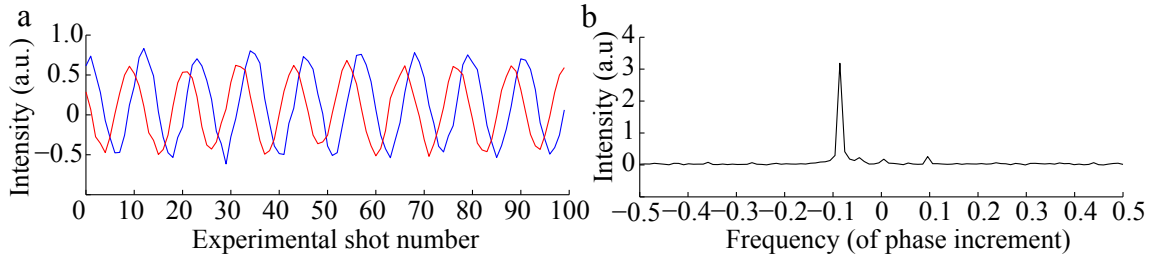

Figure 4.12: (a) Incrementing the phase of a nuclear coherence, with the real channel in blue and imaginary channel in red (b) Fourier transform of the phase increment with a peak corresponding to a nuclear coherence, in this case set to -2ϕ. Additional frequencies are due pulse imperfections.

signal, as shown in Figure 4.12, shows the frequency component corresponding to a signal from a nuclear coherence only, given in this case by -2ϕ. A T_{2n} measurement can be conducted whilst incrementing the phase (such that the x axis gives both decoherence time and phase increment (per point)) to show that this coherence contributes fully to the decaying signal.

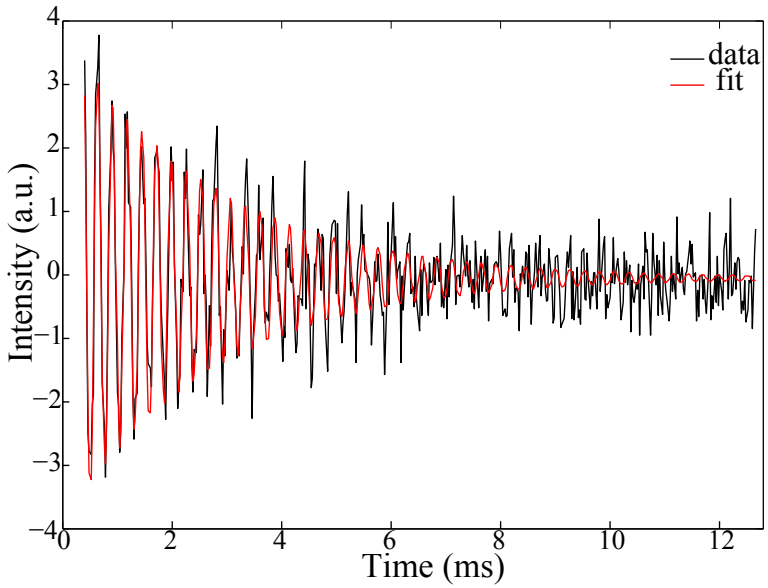

Figure 4.13: Nuclear decoherence curve at 60 K with phase increment (512 points) on the nuclear transition using a geometric phase gate. The data is fit to damped oscillatory function with an increment frequency 2ϕ as expected given a phase increment of ϕ, according to the operator in Equation (4.6).

The oscillating experimental data, Figure 4.13, fits well to a damped oscillatory function, $e^{-t/T_2}\cos(\omega t)$, which at 60 K gives $T_{2n} = 2.75 \pm 0.27$ ms and an increment frequency of 0.089 radians/experimental shot. This is entirely consistent with the T_{2n} given by the standard measurement and is at the expected nuclear coherence frequency ($2\phi = 0.088$ radians/experimental shot). This therefore shows that there is no evidence of any other contribution to the electron spin echo and that the transferred state is held entirely in the nuclear spin degree of freedom.

4.3.5 Transfer fidelity and process tomography

Now that we have shown that the transfer process works we can assess how successful it is by observing the two-way transfer fidelity for arbitrary qubit states. High fidelity measurements can be expected as the full electronic and nuclear transitions are excited. This is made possible by using short pulse lengths, typically 80 ns mw and 10 μs rf π pulses, and the narrow intrinsic sample ESR and NMR linewidths < 0.6 MHz and 15 kHz, respectively. States are prepared in the same way outlined in Section 4.2.4 and Figure 4.5 but the reference states have exactly the same electron spin dephasing time, $\tau = \tau_{e1} + \tau_{e2}$, as the recovered state. The fidelity is shown in Figure 4.15 as ~90%, similar to Si:P, with the loss in fidelity again attributed to pulse error. Using BB1 mw error correcting pulses on the +X state improves the fidelity to 94%, this is a little less than the Si:P system and perhaps indicates slightly worse pulse control in this powder environment, particularly for the rf pulses.

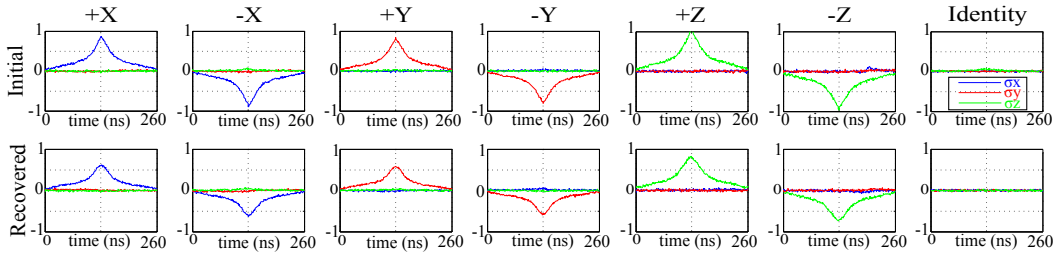

FIGURE 4.14: The reference and recovered echoes from the sequences in Figure 4.5. The σ_x, σ_y echoes occur simultaneously whilst the σ_z echo is superimposed for clarity.

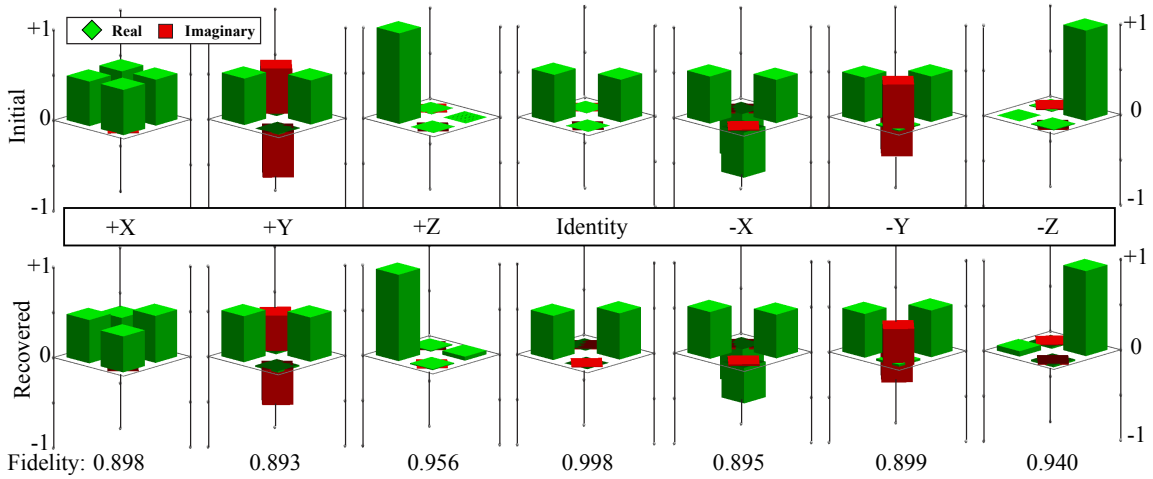

Figure 4.15: Density matrix tomography of the nominal +X, +Y, +Z, -X, -Y, -Z and Identity pseudopure states for the initial state and that recovered after storage in the nuclear spin degree of freedom. The fidelity is calculated using $F=\langle\psi|\rho_1|\psi\rangle$, where $\rho_0 = |\psi\rangle\langle\psi|$.

The robustness of the transfer sequence can also be examined by 'storing' the qubit state in the nuclear spin, returning it to the electron spin and then 're-storing' it in the nuclear spin before readout in the electron spin. Such a sequence gives a 4-way transfer fidelity (expected to be the square of the 2-way fidelity) and allows the storage of the *inner* electron coherence ($m_I = -1/2, m_S = \pm 1/2$ levels) only, as the initial storage acts to completely remove the *outer* unwanted electron coherences. The restore fidelity is given in Figure 4.16 in agreement with the standard transfer sequence (Figure 4.15).

Having shown the storage and retrieval of the +X, +Y and ± Z qubit states in the nuclear spin degree of freedom we can extract the process tomography for the operation. Following the procedure discussed in Section 4.2.5 the χ matrix is shown in Figure 4.17 (a). This has a fidelity, compared to the perfect $\mathbb{I}$, of 88%, similar to that shown by the individual quantum states and actually slightly higher than in Si:P. This is indicative of the slightly higher ±Z state fidelities using $^{15}N@C_{60}$ compared to Si:P, perhaps arising from more careful matching of the electron spin dephasing time between reference and recovered states for $^{15}N@C_{60}$. The χ matrix for the restore process has also been extracted, Figure 4.17 (b), showing a $\sqrt{fidelity}$ of 86% in agreement with the single storage procedure and state tomography data.

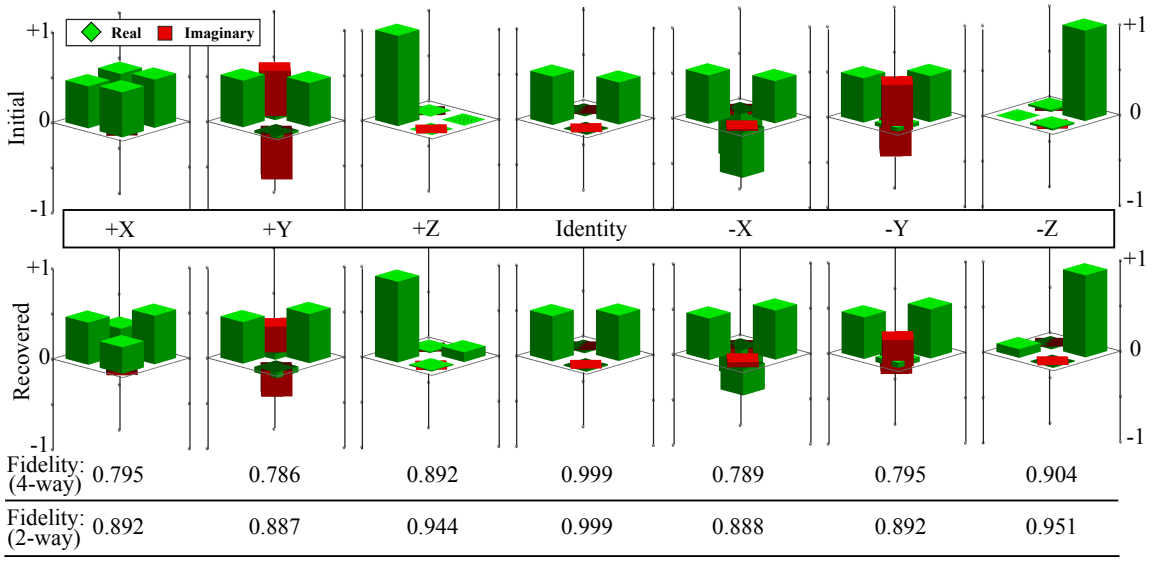

FIGURE 4.16: 'Re-store' fidelity. Density matrix tomography of the nominal +X, +Y, +Z, -X, -Y, -Z and Identity pseudopure states for the initial state and that recovered after storage twice in the nuclear spin degree of freedom. The 4-way fidelity is calculated using $F = \langle\psi|\rho_1|\psi\rangle$, where $\rho_0 = |\psi\rangle\langle\psi|$. The 2-way fidelity is given by the square route of the 4-way fidelity.

4.3.6 Probing the $m_S = \pm 3/2$ rf transitions using Davies ENDOR

In Section 4.1 we probed the $m_S = \pm 1/2$ rf transitions using coherence transfer ENDOR and showed that no *outer* electron coherence is present for τ greater than 70 μs. Therefore one might naïvely expect that it is not possible to probe rf transitions in the $m_S = \pm 3/2$ subspace using Davies ENDOR ($\pi_{mw} - \pi_{rf} - \pi/2_{mw} - \pi_{mw} - echo$ [SJ01d]). However, in fact it can be shown that such a Davies ENDOR signal can be observed via the electron *inner* coherence. If the reduced $m_I = -1/2$ subspace is considered in the electron spin basis [3/2, 1/2, -1/2, -3/2] then an inverted population (π_{mw}) followed by a π_{rf} pulse resonant on the $m_S = +3/2$ level will yield the density matrix:

$$\begin{pmatrix} 3/2 & 0 & 0 & 0 \\ 0 & -1/2 & 0 & 0 \\ 0 & 0 & 1/2 & 0 \\ 0 & 0 & 0 & 3/2 \end{pmatrix}. \tag{4.7}$$

Completing the sequence with a spin echo readout gives:

$$\begin{pmatrix} 3/8 & i\sqrt{3}/8 & -3\sqrt{3}/8 & 3i/8 \\ i\sqrt{3}/8 & 9/8 & -i/8 & -3\sqrt{3}/8 \\ -3\sqrt{3}/8 & i/8 & 9/8 & i\sqrt{3}/8 \\ -3i/8 & -3\sqrt{3}/8 & -i\sqrt{3}/8 & 3/8 \end{pmatrix}. \tag{4.8}$$

Given the results of the previous section, we know the electron spin echo intensity is determined by the *inner* coherence only, characterised by a measurement of S_y(inner):

$$I_{\mathrm{ESE}} = \mathrm{Tr}[\rho.S_y(\mathrm{inner})] = 1/4, \qquad \text{where } S_y(\mathrm{inner}) = \begin{pmatrix} 0 & 0 & 0 & 0 \\ 0 & 0 & -i & 0 \\ 0 & i & 0 & 0 \\ 0 & 0 & 0 & 0 \end{pmatrix}. \tag{4.9}$$

As $I_{\mathrm{ESE}}(\text{no rf}) = -1$ in the Davies ENDOR experiment, this yields $F_{\mathrm{ENDOR}} = 0.625$.

Thus, theoretically one is able to observe the $m_S = \pm 3/2$ ENDOR transitions through the *inner* electron coherence. This result can be understood by examining the nature of a $\pi/2$ pulse in the high spin system. Figure 4.18(a) shows the relative populations of the high spin system (starting from a thermal state) under the influence of a mw pulse of varying length. As expected, a $\pi/2$ pulse acts to equalise the populations, while a π pulse swaps populations. However, in Figure 4.18(b), starting from the state in Equation (4.7) during the Davies ENDOR experiment, the subsequent $\pi/2$ pulse acts to separately equalise both the $m_S = \pm 3/2$ and $m_S = \pm 1/2$ levels. The $m_S = \pm 1/2$ levels (in blue) actually increase in relative population on application of a $\pi/2$ pulse relative to the $m_S = \pm 3/2$ populations. This behaviour gives rise to the observable ENDOR signal which is confirmed experimentally with $F_{\mathrm{ENDOR}} \sim 0.4$, as shown in Figure 4.19. The difference between theoretical and experimental F_{ENDOR} values is due to imperfect pulses. Significantly this means that the full nuclear spin subspace can be exploited even if the *outer* electron coherence times are short (see next section).

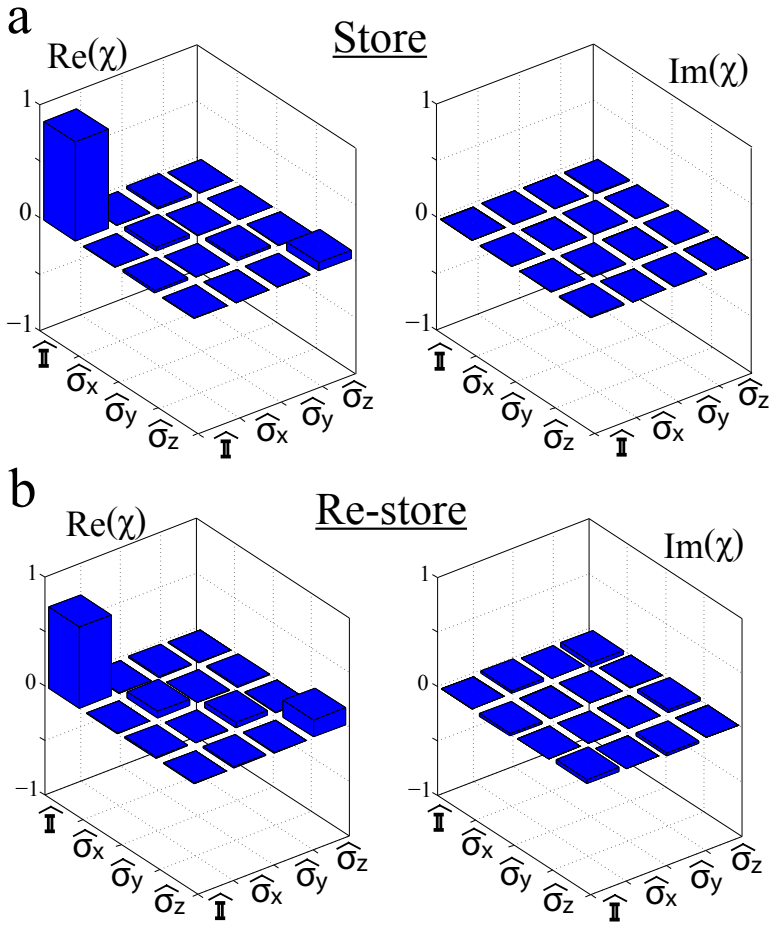

FIGURE 4.17: Quantum process tomography matrix (χ) for the transfer of a qubit state from the electron to the nuclear degree of freedom and back a) once (store) and b) twice (restore), in the basis ($\mathbb{I}$, σ_x, σ_y, σ_z). χ is evaluated given reference and recovered matrices and gives a fidelity compared to a perfect $\mathbb{I}$ of a) 0.88 and b) 0.74 ($\sqrt{fidelity} = 0.86$).

4.3.7 Nuclear coherence in the $m_S = \pm 3/2$ subspace

The previous sections discussed the transfer of qubit states from the electron spin *inner* levels to the nuclear spin $m_S = \pm 1/2$ manifolds. Transfer from of an electron spin *outer* coherence to the nuclear spin is not possible, but the nuclear spin transitions in the $m_S = \pm 3/2$ manifolds could be still used to store quantum information and make greater use of the multi-levelled system. A sequence can be applied to directly probe $T_{2\mathrm{n}}$ of the $m_S = \pm 3/2$ manifolds not possible in the low concentration limit using NMR. The sequence (Figure 4.20) uses an rf $\pi/2$ pulse on the $m_S = +3/2$ manifold to directly generate a nuclear coherence of arbitrary phase (given by φ). The

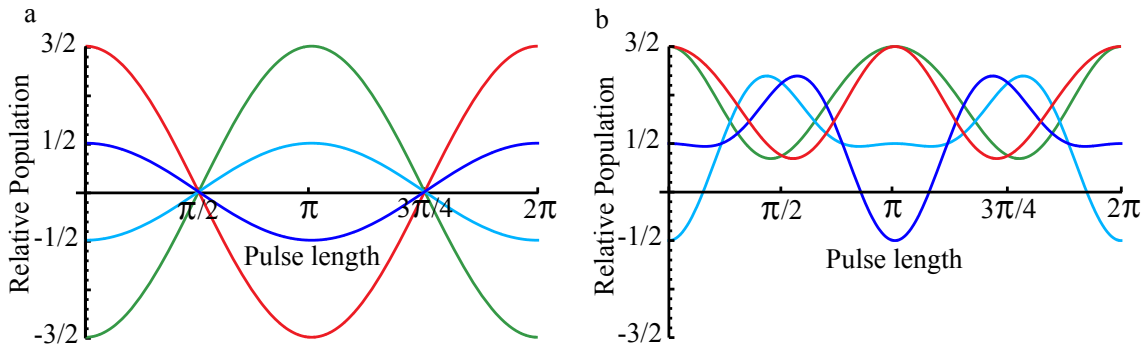

Figure 4.18: Relative population of an electron spin 3/2 system under application of a pulse of varying length a) Starting from an initial S_z or inverted state b) Starting from an inverted state with a π rf pulse resonant on the $m_S = +3/2$ level (as in a Davies ENDOR experiment on the $m_S = +3/2$ line, this state is shown in Equation (4.7)).

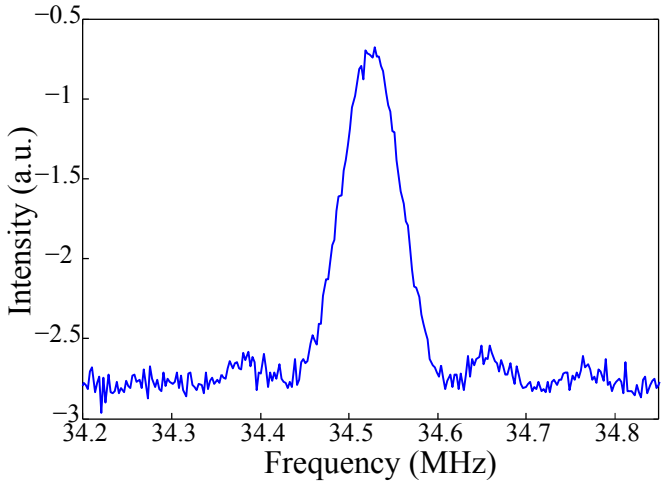

Figure 4.19: $^{15}N@C_{60}$ Davies ENDOR on the $m_S = 3/2$ transition with a 'tidying' pulse (see the section on Si:P ENDOR). The resonance is observed through the *inner* electron coherence, as described in the text.

coherence is then stored for a time ($2\tau_n$) and transferred to a nuclear polarisation via a second rf $\pi/2$ pulse for readout by a selective electron spin echo. The rf frequency in Figure 4.20 is set to 40 kHz off-resonance and the second $\pi/2$ pulse swept to show the fringe pattern of the nuclear coherence, read via the electron spin. The phase varies as expected with the initial coherence generated. The T_{2n} can then be measured with the rf on resonance and the electron spin readout in fixed position, incrementing τ_n. A subtlety of this experiment is that it only allows measurement of T_{2n} in the region where $T_{1e} > T_{2n}$, as it relies on the polarisation given by the electron spin inversion

(initial π mw pulse). Remarkably, as the measurement is effectively of electron spins that have not relaxed, when $T_{1e} \leq T_{2n}$ the nuclear spin shows no decoherence. In the low temperature region we find $T_{1e} > T_{2n}$ and the extracted nuclear coherence times for the $m_S = \pm 3/2$ transitions to be of similar order to those in the $m_S = \pm 1/2$ manifolds, which we explore in the next chapter. This indicates a nuclear decoherence mechanism which acts similarly for all nuclear spin manifolds.

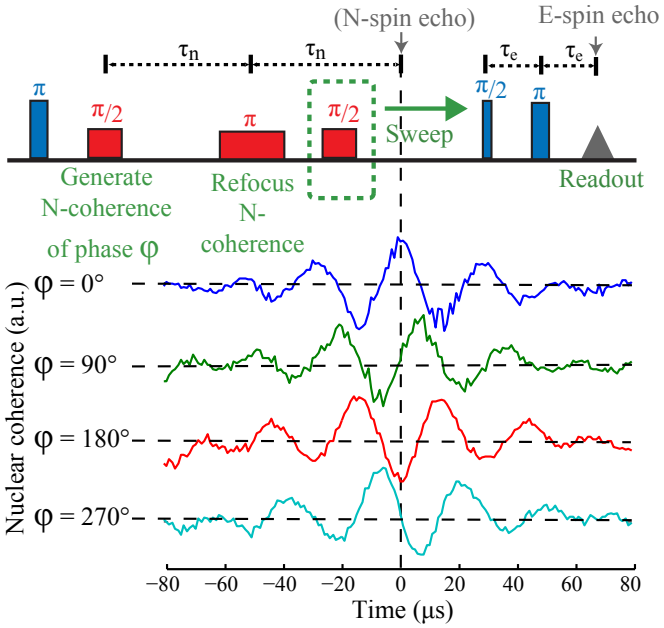

FIGURE 4.20: Sequence to probe the nuclear coherence for $m_S = \pm 3/2$, as described in the text. The initial phase generated in the nuclear spin is faithfully recovered by polarisation transfer and readout using the electron spin. The nuclear coherence is off-resonance in order to more clearly observe the recovered phase.

4.3.8 Controlling interactions through coherent transfer

The work described thus far utilises the coherent transfer from electron to nuclear spin states as a memory element. However, the weaker magnetic moment of the nuclear spin can also be exploited to effectively turn on and off inter-qubit dipolar interactions which are 'always-on'. The theoretical implications of this have been elucidated in a number of molecular proposals [SL02b, HMW02, JSD07, YXW10, BAB06]. These

arise from the generalised Hamiltonian for dipolar interaction, given by:

$$\mathcal{H}_{dip} = \frac{\mu_0}{4\pi r_{j,k}^3}(\boldsymbol{\mu}_j \cdot \boldsymbol{\mu}_k - 3(\boldsymbol{\mu}_j \cdot \boldsymbol{r}_{j,k}) \otimes (\boldsymbol{\mu}_k \cdot \boldsymbol{r}_{j,k})) \tag{4.10}$$

where μ_0 is the permittivity of free-space, $r_{j,k}$ the distance between the two spins and μ the magnetic moment [NC00a]. The magnetic moment of a nuclear spin is typically 3 orders of magnitude weaker than an electron spin and thus inter-qubit dipolar interactions can effectively be turned on and off with a ratio of $\sim 10^6$, by moving between entities. The advantages of a molecular system are the ability to produce larger QIP architectures that can be engineered to control electron dipolar interaction [GRKS10]. The simplest example of this would be a dimer system with a dipolar interaction of two spins, l and m, with the field and dimer axis aligned, this is given by:

$$\mathcal{H}_{dip} = \frac{\mu_0 \gamma_l \gamma_m}{4\pi r^3}(S_{x,l} \otimes S_{x,m} + S_{y,l} \otimes S_{y,m} - 2S_{z,l} \otimes S_{z,m}) \tag{4.11}$$

where γ is the gyromagnetic ratio of the two spins, $r_{l,m}$ the distance between the two spins and S_i the spin matrices. We do not have the control of a dimer system but have previously extracted, in Section 3.5.2, a dipolar coupling of 2.5 kHz between electron spins at the average $N@C_{60}$ separation. Applying the coherent transfer sequence, in the nuclear spin state we would now expect a much weaker inter-qubit dipolar coupling, based on Equation (4.10), on the order of milliHz. The nuclear dipolar coupling can be assessed through the effect on T_{2n} of an 'instantaneous diffusion' experiment, similar to that applied on the electron spin (Section 4.3.1). Using the transfer sequence in Figure 4.11 and varying the time the state is held in the nuclear spin (τ_n), the T_{2n} time can be found. The length of the nuclear refocusing pulse can then be reduced ($0.2 \leq \sin^2(\theta_{rf}/2) \leq 1.0$, see Figure 4.21), showing no appreciable change in T_{2n} at 20 K. Hence, we show the dipolar interaction is $\ll 25$ Hz and effectively 'turned off' between neighbouring nuclear spin qubits. The value of T_{2n} limits the interaction frequency that can be observed such that we can only extract an upper bound for the dipolar

coupling. However, the experiment shows that the coherent state transfer can effectively turn on/off inter-qubit interactions by at least three orders of magnitude and is expected to do this by six orders of magnitude. Therefore, given precision engineered larger architectures, state transfer could be used to control qubit interactions, a key requirements towards quantum information processing [DiV00].

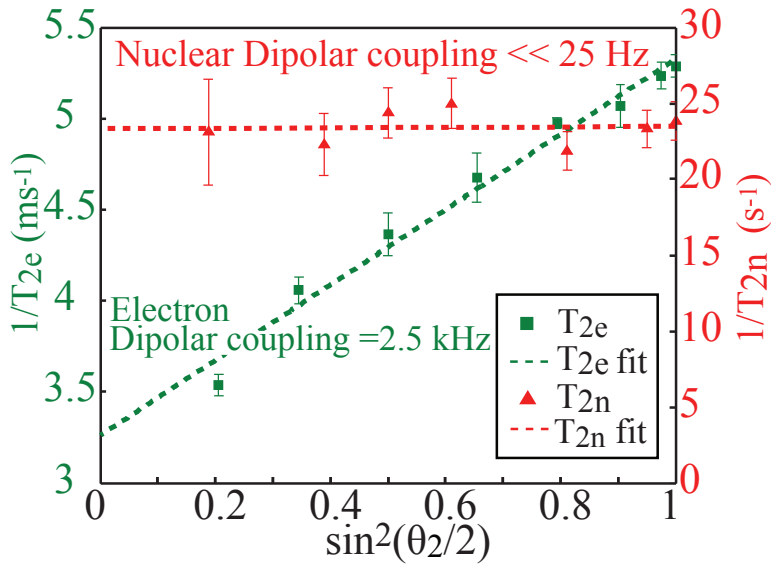

FIGURE 4.21: Dipolar coupling between nuclear (red) and electron (green) spin states can be measured by varying the length of the refocusing pulse θ_2 (see main text), found to be much weaker when they reside in the nuclear spin than in the electron spin (data taken at 20 and 40 K respectively). Due to the limited nuclear spin coherence time, only an upper bound for the nuclear dipolar coupling strength can be extracted. The data for the electron spin excludes the effect of impurity spins, dominant at low turning angles (see Section 3.5.2) for simplicity.

4.4 High purity state production: Entanglement in Si:P

The work described in Section 4.2 and Section 4.3 shows the coherent transfer of pseudo-pure electron starting states, such as $\pm X, \pm Y$ and $\pm Z$, to the nuclear spin and back. However, using EPR and moving to lower temperatures and higher magnetic fields the polarisation available to the electron spin can be increased, resulting in high

purity starting states. A particularly interesting state is that of an pseudo-pure entangled state generated during the coherent transfer process after the application of a $\pi/2_{mw}$ and π_{rf} pulse as shown in Figure 4.1(b), where it is also referred to as a DQC. Pseudo-pure entanglement between electron and nuclear spin states has previously been created in $^{15}N@C_{60}$ by Mehring *et al.* [MSW04], similar to a step in the coherent transfer sequences, Figure 4.11, but using the *outer* levels. Proving entanglement is present is more challenging and requires specific phase labeling of all the coherences through the application of Z-gates, such as geometric phase gates similar to those shown in Section 4.3.4. To produce 'true' entanglement rather than just pseudo-entanglement one must go to low temperatures and high magnetic fields. The system can also be further 'hyperpolarised' by manipulation based on moving populations to one nuclear spin manifold and utilising the faster electron, compared to the nuclear spin, relaxation. Thus, using the 'hyperpolarisation' sequence and at 2.9 K and 3.4 T, we have shown 'true' entanglement in Si:P. This is not the main discussion of this thesis but is described further in Ref [SBR11]. However, the work highlights that high purity initial states could be produced and full tomography of the system used to readout more complex algorithms and procedures, such as interactions of two electron spin qubits using the dipolar interaction in molecular systems, see Section 4.3.8.

5

Nuclear decoherence

5.1 Introduction

The previous section outlined how electron spin states could be coherently transferred to nuclear spin states, and back, with high fidelity. This was conducted for both Si:P and $^{15}N@C_{60}$ samples, with the latter also showing that this transfer could be used to turn on and off dipolar interactions. However, the main advantage of this propagation process is to utilise the anticipated longer nuclear spin decoherence times (T_{2n}), compared to electron spin decoherence times. A longer T_{2n} is expected due to the weak magnetic moment of the nuclear spin, typically three orders of magnitude less than the electron spin, and hence much weaker interaction with the environment. This

chapter will explore if indeed longer nuclear coherence times are observed, how these vary with temperature and the fundamental limits of these times through modelling of the systems.

5.2 Nuclear decoherence times in Si:P

5.2.1 Experimental nuclear decoherence sequence

The nuclear spin decoherence time can be assessed using the standard transfer sequence, illustrated in Figure 4.4, but extending the time in which the state is held in the nuclear spin degree of freedom, τ_n. The recovered electron spin echo state (typically +X) is monitored whilst extending τ_n, with the echo decay giving $T_{2\mathrm{n}}$. During this process all other timings and pulse lengths must stay the same, especially the time in which the state is held in the electron spin degree of freedom. $T_{2\mathrm{n}}$ is found using the low concentration, 1.2×10^{14} P cm^{-3}, single crystal sample that was used to show the high fidelity transfer process. In the range 9–12 K this sample (and other higher concentration samples) show $T_{2\mathrm{n}}$ to be limited by twice $T_{1\mathrm{e}}$. Intuitively, this is perhaps a surprising result as one would expect a spin flip to cause the system to decohere and hence give a limit of $T_{2n} = T_{1e}$. Over 9–12 K $T_{2\mathrm{n}}$ follows the $T_{1\mathrm{e}}$ Arrhenius temperature dependence, increasing exponentially with decreasing temperature according to a two phonon relaxation processes coupled to an excited state [Cas62, TLAR03]. This is known as an Orbach relaxation process, with similar dependence to the analysis described in Section 3.3 and Section 3.5.5, i.e. $T_{1e} \propto e^{(\Delta/k_B T)} - 1$, but where Δ is the energy gap to the excited state involved in the relaxation process, given as $\Delta = 126$ K [TLAR03], rather than to a vibrational mode.

5.2.2 Modelling nuclear decoherence in an electron spin-1/2 system

To understand and prove the experimentally observed limit, $T_{2n} = 2T_{1e}$, the Si:P system can be modelled. The model is constructed using Mathematica to simulate the effect of electron relaxation on a nuclear spin coherence. The model is general in that it could be applied to various nuclear spin-1/2, electron spin-1/2 systems, depending on the parameters set.

The chosen basis, described more fully in terms of the individual matrix elements in Section 2.3, is:

$$(S, I) = \left[\left(\frac{1}{2}, \frac{1}{2}\right), \left(-\frac{1}{2}, \frac{1}{2}\right), \left(\frac{1}{2}, -\frac{1}{2}\right), \left(-\frac{1}{2}, -\frac{1}{2}\right)\right], \tag{5.1}$$

where S represents the electron spin, and I the nuclear spin. The system is initialised at thermal equilibrium and can undergo a series of microwave or radiofrequency pulses, modelled as matrix rotations, to produce the state before relaxation.

Electron relaxation is modelled using a standard master equation in Lindblad form (i.e. the Liouville-von Neumann equation with relaxation terms). In order to represent processes that take the system to thermal equilibrium, both raising and lowering terms are included.

$$\dot{\rho} = -\frac{\gamma}{2}(\rho S^- S^+ + S^- S^+ \rho - 2S^+ \rho S^-) - \frac{\gamma e^{-\beta}}{2}(\rho S^+ S^- + S^+ S^- \rho - 2S^- \rho S^+) - i[\mathcal{H}, \rho] \tag{5.2}$$

where γ is the relaxation rate, $\beta = -\frac{g\mu_B B_0}{kT}$ and S^+ and S^- are the electron spin raising and lowering operators ($S^{\pm} = S_x \pm iS_y$) given in matrix form as:

$$S^+ = \begin{pmatrix} 0 & 1 & 0 & 0 \\ 0 & 0 & 0 & 0 \\ 0 & 0 & 0 & 1 \\ 0 & 0 & 0 & 0 \end{pmatrix}. \qquad S^- = \begin{pmatrix} 0 & 0 & 0 & 0 \\ 1 & 0 & 0 & 0 \\ 0 & 0 & 0 & 0 \\ 0 & 0 & 1 & 0 \end{pmatrix}. \tag{5.3}$$

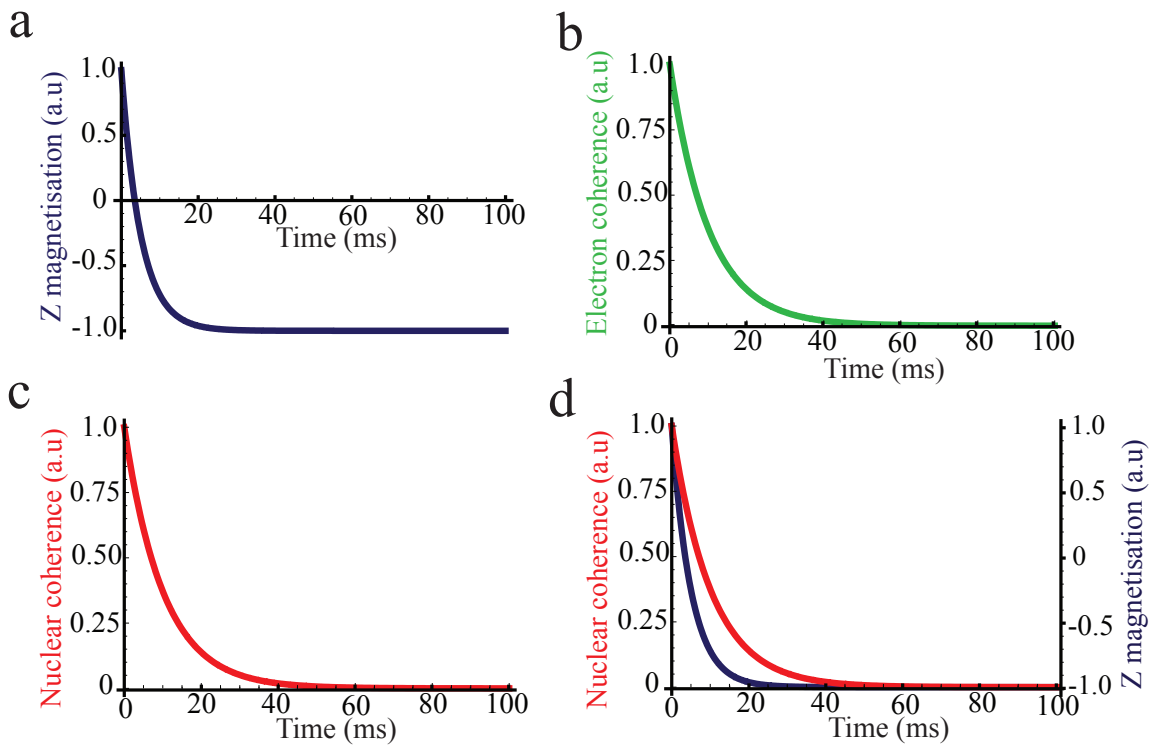

FIGURE 5.1: Figure showing partial traces of systems under electron relaxation, starting with the state corresponding to: a) an electron inversion; b) an electron coherence; c) a nuclear coherence and d) both an electron inversion (blue) and a nuclear coherence (red). The parameters used are representative of phosphorous doped silicon ($A = 100$ MHz, $\gamma = 100$ Hz, $\beta = 0.02$) and when fitted (d) gives $T_{2n} = 2\,T_{1e}$.

The master equation can be simplified by transforming into the rotating frame of the Hamiltonian, taking an Ising approximation ($\mathcal{H}_0 = \omega_e S_z - \omega_I I_z + A \cdot S_z \cdot I_z$). In this frame, $\mathcal{H}$ goes to 0, and we are left only with the relaxation part of Equation (5.2), with S^+ and S^- transformed into the rotating frame. The differential can be solved numerically for each element of the matrix and the result given via a partial trace.

The state before relaxation can be initialised and values set to model the effect on an electron inversion, electron coherence and nuclear coherence, shown in Figure 5.1. Using appropriate parameters for phosphorous doped silicon and fitting the traces for T_{2n} and T_{1e} the simulation reveals, graphically shown in Figure 5.1 (d), that $T_{2n} = 2\,T_{1e}$.

Having shown the relationship through numerical simulation an analytical analysis of

the relaxation process can be performed. Neglecting direct nuclear relaxation ($T_{1n} \rightarrow \infty$) and in the high temperature limit, this yields:

$$\dot{\rho} \simeq -\frac{\gamma}{2}\begin{pmatrix} \rho_{1,1}(t)-\rho_{2,2}(t) & \rho_{1,2}(t) & \rho_{1,3}(t)-e^{-iAt}\rho_{2,4}(t) & \rho_{1,4}(t) \\ \rho_{2,1}(t) & \rho_{1,1}(t)-\rho_{2,2}(t) & \rho_{2,3}(t) & \rho_{2,4}(t)-e^{iAt}\rho_{1,3}(t) \\ \rho_{3,1}(t)-e^{iAt}\rho_{4,2}(t) & \rho_{3,2}(t) & \rho_{3,3}(t)-\rho_{4,4}(t) & \rho_{3,4}(t) \\ \rho_{4,1}(t) & \rho_{4,2}(t)-e^{-iAt}\rho_{3,1}(t) & \rho_{4,3}(t) & \rho_{3,3}(t)-\rho_{4,4}(t) \end{pmatrix}. \tag{5.4}$$

The electron relaxation rate, ($\frac{1}{T_{1e}}$), can be ascertained by observing the appropriate density matrix elements:

$$\dot{\rho}_{1,1}+\dot{\rho}_{3,3} = -\frac{\gamma}{2}(\rho_{1,1}+\rho_{3,3})+\frac{\gamma}{2}(\rho_{2,2}+\rho_{4,4}) = -\frac{\gamma}{2}(\rho_{1,1}+\rho_{3,3})+\frac{\gamma}{2}(1-\rho_{1,1}-\rho_{3,3})$$

Taking $\rho_e = \rho_{1,1}+\rho_{3,3}$ then, $\dot{\rho}_e = -\gamma(\rho_e - 1/2)$. Solving this gives:

$$\rho_e = 1/2e^{-\gamma t}(e^{\gamma t}+2\rho_0-1) \tag{5.5}$$

where ρ_0 is the density matrix at time zero, in this case given as 1. Alternatively, this can be expressed as:

$$\rho_e = 1/2e^{-\gamma t}+1/2 \tag{5.6}$$

Hence, electron relaxation follows $e^{-\gamma t}$ and the electron relaxation time, $T_{1e} = \frac{1}{\gamma}$.

The nuclear coherence is given by $\rho_{nn} = \rho_{3,1}+\rho_{4,2}$. Extracting these terms from Eq. 5.4 yields two coupled differential equations:

$$\begin{pmatrix} \dot{\rho_{3,1}} \\ \dot{\rho_{4,2}} \end{pmatrix} = -\frac{\gamma}{2}\begin{pmatrix} 1 & -e^{iAt} \\ -e^{-iAt} & 1 \end{pmatrix}\begin{pmatrix} \rho_{3,1} \\ \rho_{4,2} \end{pmatrix} \tag{5.7}$$

The time dependence in the 2×2 matrix in this equation can be eliminated by making

a time dependent unitary transformation and solving for new variables $\rho'_{3,1}$ and $\rho'_{4,2}$.

$$\begin{pmatrix} \rho'_{3,1} \\ \rho'_{4,2} \end{pmatrix} = U \begin{pmatrix} \rho_{3,1} \\ \rho_{4,2} \end{pmatrix} = \begin{pmatrix} e^{iAt/2} & 0 \\ 0 & -e^{-iAt} \end{pmatrix} \begin{pmatrix} \rho_{3,1} \\ \rho_{4,2} \end{pmatrix} \tag{5.8}$$

Following this transformation, solving the pair of differential equations gives an eigenvalue problem. In the experiments the hyperfine coupling $A = 117$ MHz and γ ranges from 1 kHz to less than 1 Hz (as a function of temperature), hence we can take the limit $A \gg \gamma$. In this case, both characteristic eigenvalues have a real part of $-\gamma/2$, and therefore any nuclear coherence decays with this rate. Thus $T_{2n} = \frac{2}{\gamma} = 2\,T_{1e}$ as numerically simulated and experimentally observed.

Effect of hyperfine interaction

An interesting feature of the relaxation model is the relationship between A and γ. In the limit of $A \ll \gamma$ the model leads to no relaxation of the nuclear decoherence due to the small hyperfine interaction. However as A approaches γ it leads to oscillations in the nuclear decoherence, maximised at $A = \gamma$ a result that is seen graphically in Figure 5.2. Probing these oscillations using an EPR experiment would prove difficult as the short relaxation times required (to give $A = \gamma$) would not allow the nuclear coherence to be observed (using the sequence shown in the previous chapter). However, it may be possible to probe the nuclear coherence directly using an NMR experiment and a material with a short electron spin relaxation time.

5.2.3 Experimental nuclear decoherence temperature dependence

Modelling the system has shown that the fundamental limit for $T_{2\mathrm{n}}$ is $2\,T_{1\mathrm{e}}$, also shown experimentally above 9 K.

However, below 9 K although $T_{1\mathrm{e}}$ continues to increase exponentially, $T_{2\mathrm{n}}$ becomes

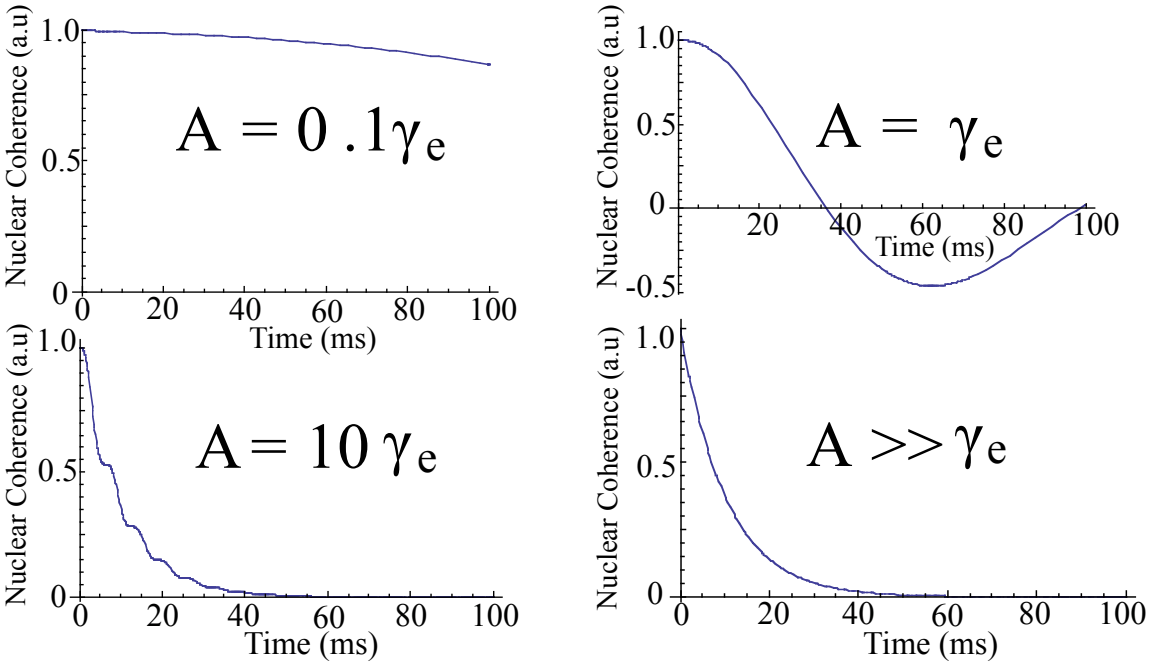

Figure 5.2: A nuclear coherence under electron relaxation, varying the parameter A with γ set to 100 Hz.

limited by an additional decoherence process, shown in Figure 5.3.

The T_{2n} temperature dependence can therefore be fitted as a sum of two rates:

$$T_{2n} = \frac{1}{\frac{1}{T_{lim}} + \frac{1}{2T_{1e}}} \tag{5.9}$$

where T_{lim} is a constant determined experimentally. The fitting for this sample in Figure 5.3 shows a limit of approximately 50 ms using the standard Hahn echo sequence. To improve this time we can dynamically decouple the nuclear spin state from the environment using techniques that have been previously implemented in NMR. The Carr-Purcell (CP) [CP54] and Carr-Purcell-Meiboom-Gill (CPMG) [MG58] sequences apply a series of π_{rf} pulses to refocus the nuclear spin echo, removing the effect of field fluctuations. Experimentally this is implemented by applying up to 1000 π_{rf} pulses whilst the qubit is held in the nuclear state. CP applies pulses around the same axis in which the magnetisation is initially tipped into the plane, whereas CPMG applies the pulse around the orthogonal axis (e.g $\pi_x/2 - [\pi_x]_n$ for CP and $\pi_x/2 - [\pi_y]_n$ for

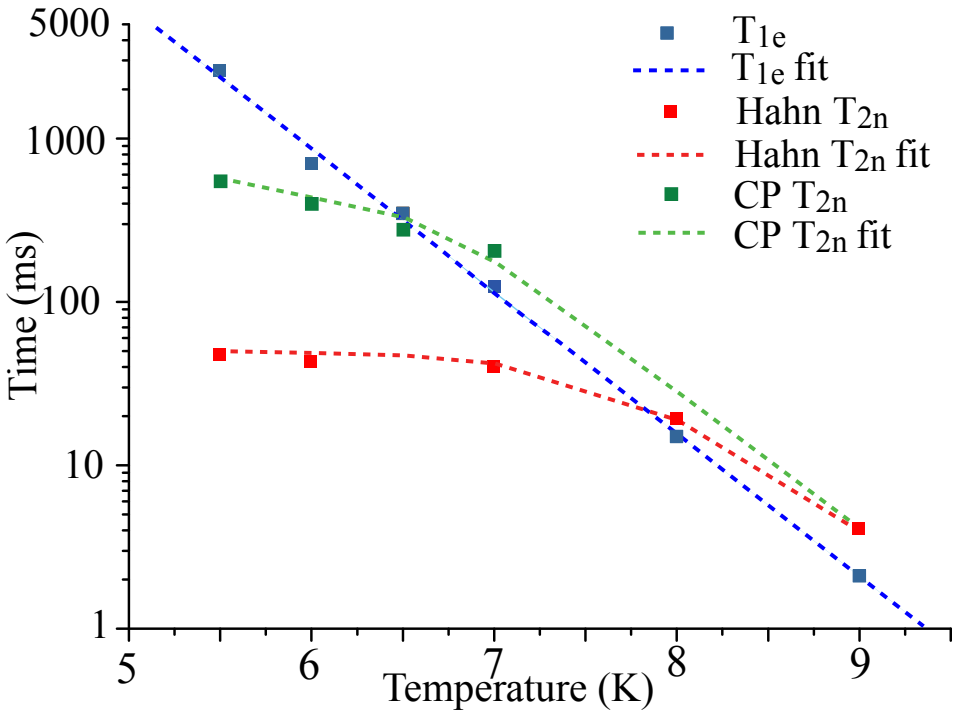

FIGURE 5.3: T_{1e} and T_{2n} standard Hahn echo and CP sequence, as a function of temperature for sample 1. Estimated relaxation rate is modelled as a sum of two rates, twice electron relaxation and a fitted second limiting rate, given by Eq. 5.9.

CPMG, where n is the number of refocusing pulses and the subscript indicates the axis of rotation). Applying the CP sequence to the same sample that a Hahn echo T_{2n} $\sim$ 50 ms limit was observed, a T_{2n} limit of 660 ms is found. Again the temperature dependence is fitted to Equation (5.9) as shown in Figure 5.3. CP is known to be more sensitive to rotational errors than CPMG and thus applying a CPMG sequence with a repetition rate of 1-kHz at 5.5 K we can achieve a T_{2n} of 1.75 s, shown in Figure 5.4. If we compare this time to the T_{2e} time of the sample, given under optimised conditions as 6.5 ms, we show an improvement in the decoherence time of several orders of magnitude. Thus, we show a viable quantum memory using the ^{31}P nuclear spin with a long nuclear coherence time.

As well as showing temperature dependence T_{2n} also reveals sample dependence on the limiting decoherence time, T_{lim}. To understand this a range of samples must be produced, varying parameters such as the dopant concentration, Boron compensation and the ^{29}Si:^{28}Si ratio. However, producing precise samples without varying multiple

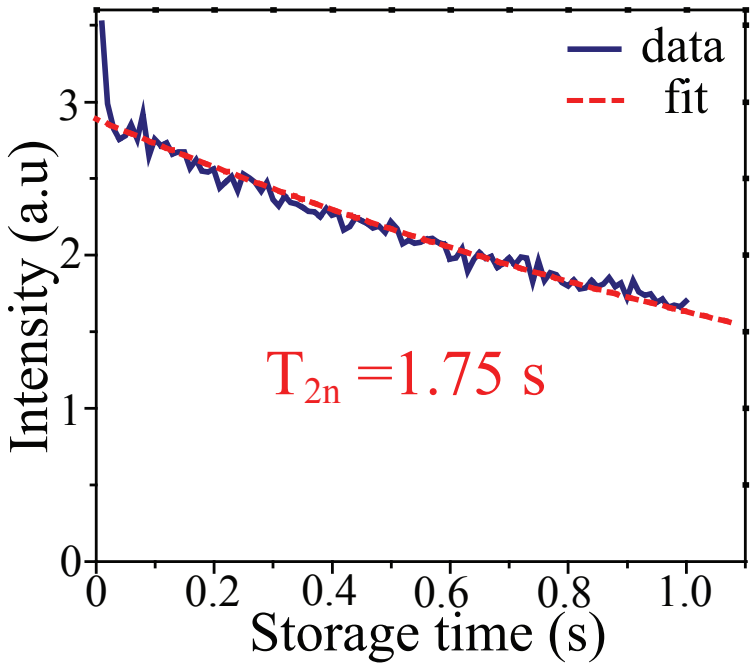

FIGURE 5.4: T_{2n} at 5.5 K using a a CPMG sequence. The data fits to an exponential decay time of 1.75 s, with the spectrometer software limiting the experimental acquisition of data to 1 s.

parameters is difficult, thus, this dependence is yet to be fully understood and is the subject of continual research.

5.3 Nuclear decoherence times in $^{15}N@C_{60}$

5.3.1 Experimental nuclear decoherence times

The nuclear decoherence time for $^{15}N@C_{60}$ can be determined by increasing the shot to shot time quantum information is held within the nuclear spin state and observing the recovered electron spin echo decay, similar to Si:P. This is shown in Figure 5.5 over the range 5–80 K, at 80 K the T_{2e} of the system begins to decrease, making high fidelity transfer difficult above this temperature (weak recovered signal). Over the range 40–80 K the T_{2n} time is found to be limited by T_{1e} of the system. In contrast to the electron spin-1/2 Si:P system, the experimental limit is not found to be twice T_{1e}

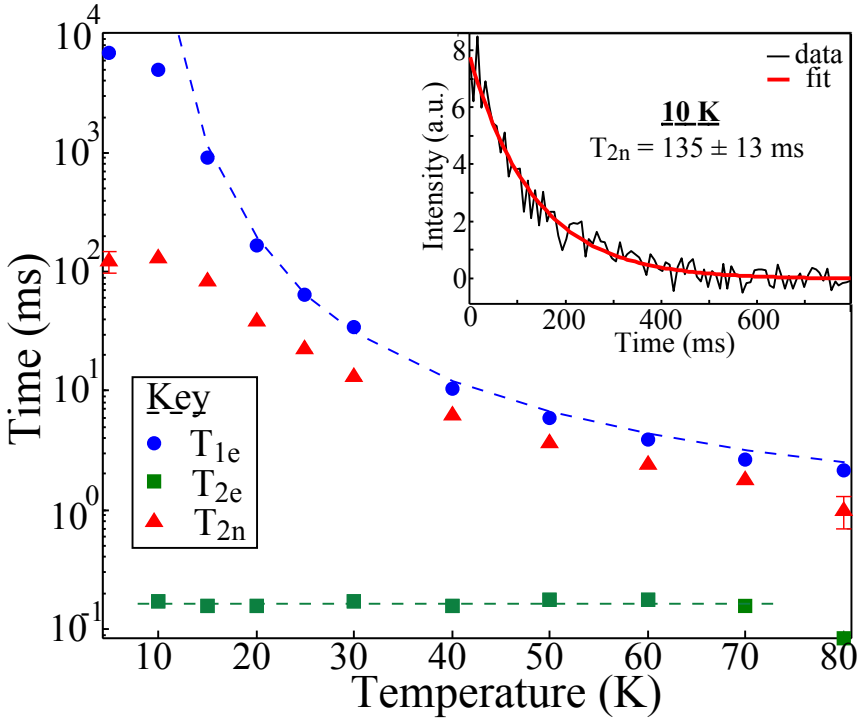

FIGURE 5.5: Relaxation and decoherence times as a function of temperature: T_{1e} (blue, circle), T_{2e} (green, square), T_{2n} (red, triangle), from monoexponential fits with error less than the marker size unless shown. The dashed line is a fit to an Arrhenius temperature dependence for T_{1e}(see Section 5.6). The dotted line for T_{2e} is a guide. Inset, the nuclear decoherence curve with a monoexponential fit to 135 ± 13 ms at 10 K.

but is given as $T_{2n} \sim 0.6\,T_{1e}$, which is modelled in the following section. The Arrhenius temperature dependence of T_{1e} was discussed in Section 5.6 and the same fitting parameters are applied to dashed fit line in Figure 5.5. Decreasing in temperature below ~40 K, T_{1e} continues to increase exponentially whereas the T_{2n} becomes limited by a secondary mechanism to ~130 ms. This behaviour does not give a good fit to the simple analysis based on the sum of two different relaxation rates, one limiting and one due to T_{1e} (i.e.$\sim 0.6\,T_{1e}$), that was used for Si:P, Equation (5.9). This may reflect more complex relationships in the material due to, for instance, the breakdown of the T_{1e} Arrhenius temperature dependence below 15 K or different relaxation rates within the N@C_{60} high spin system. Nevertheless, at 10 K a T_{2n} of 135 ± 13 ms is observed, shown in the inset of Figure 5.5. At this temperature the T_{2e} time is 160 μs and thus the nuclear memory gives almost three orders of magnitude improvement in the decoherence time. The 'intrinsic' T_{2e} for this sample was shown in Section 3.5.4

to be of the order 400 μs and hence under highly optimised conditions this still shows well over two orders of magnitude improvement. In Si:P the T_{2n} limit was improved by using a dynamic decoupling CP or CPMG sequence, however, using $^{15}N@C_{60}$ the addition of such rf pulses causes substantial signal decay. This is indicative of higher rf pulse error in this powder system compared to Si:P, also shown by the limited fidelity improvement using mw BB1 pulses. Overall, both systems show similar improvements in T_{2n}, though $^{15}N@C_{60}$ does so without the use of dynamic decoupling. To investigate the limiting $^{15}N@C_{60}$ decoherence mechanism a higher concentration $^{15}N@C_{60}$ sample was produced that showed a T_{2n} of 5.8 ms at 10 K, but this had a lower T_{2e} and a higher concentration of impurities. Therefore to investigate this fully a series samples must be prepared overcoming the problems of uncontrollable T_{2e} times and factors discussed in Section 3.5.1.

5.3.2 Modelling nuclear decoherence times in an electron spin-3/2 system

To understand the experimentally observed relationship $T_{2n} \sim 0.6\, T_{1e}$, we can model the $^{15}N@C_{60}$ electron spin-3/2 system. A similar approach can be adopted to the spin-1/2 system which we have shown to work but clearly the situation will be complicated by the 8×8 matrix and higher spin relaxation operators. The basis used is:

$$(S, I) = \left[\left(\frac{3}{2}, \frac{1}{2}\right), \left(\frac{1}{2}, \frac{1}{2}\right), \left(-\frac{1}{2}, \frac{1}{2}\right), \left(-\frac{3}{2}, \frac{1}{2}\right), \right.$$
$$\left. \left(\frac{3}{2}, -\frac{1}{2}\right), \left(\frac{1}{2}, -\frac{1}{2}\right), \left(-\frac{1}{2}, -\frac{1}{2}\right), \left(-\frac{3}{2}, -\frac{1}{2}\right) \right]$$

where S is the electron and I the nuclear spin state. The matrix is initialised according to a thermal distribution, before producing the required starting state and applying relaxation via the Lindblad Equation (5.2). The raising and lowering operators for the

spin-3/2 system are given by:

$$S^{+} = \begin{pmatrix} 0 & \sqrt{3} & 0 & 0 & 0 & 0 & 0 & 0 \\ 0 & 0 & 2 & 0 & 0 & 0 & 0 & 0 \\ 0 & 0 & 0 & \sqrt{3} & 0 & 0 & 0 & 0 \\ 0 & 0 & 0 & 0 & 0 & 0 & 0 & 0 \\ 0 & 0 & 0 & 0 & 0 & \sqrt{3} & 0 & 0 \\ 0 & 0 & 0 & 0 & 0 & 0 & 2 & 0 \\ 0 & 0 & 0 & 0 & 0 & 0 & 0 & \sqrt{3} \\ 0 & 0 & 0 & 0 & 0 & 0 & 0 & 0 \end{pmatrix} . \; S^{-} = \begin{pmatrix} 0 & 0 & 0 & 0 & 0 & 0 & 0 & 0 \\ \sqrt{3} & 0 & 0 & 0 & 0 & 0 & 0 & 0 \\ 0 & 2 & 0 & 0 & 0 & 0 & 0 & 0 \\ 0 & 0 & \sqrt{3} & 0 & 0 & 0 & 0 & 0 \\ 0 & 0 & 0 & 0 & 0 & 0 & 0 & 0 \\ 0 & 0 & 0 & 0 & \sqrt{3} & 0 & 0 & 0 \\ 0 & 0 & 0 & 0 & 0 & 2 & 0 & 0 \\ 0 & 0 & 0 & 0 & 0 & 0 & \sqrt{3} & 0 \end{pmatrix} . \tag{5.10}$$

Transforming the master equation into the rotating frame, using the Ising approximation and ignoring direct nuclear relaxation the effect of electron relaxation can be observed. Applying experimental parameters and numerically solving the differential for each element the result is again given by performing a partial trace. The result is shown in Figure 5.6 for the initial starting states of both an electron inversion and nuclear coherence. Fitting these curves, this model gives the numerical result $T_{2\mathrm{n}} \sim 0.3\, T_{1\mathrm{e}}$, which is clearly less than that observed experimentally.

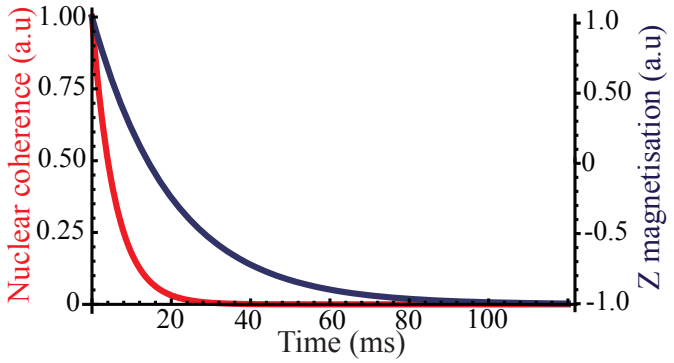

FIGURE 5.6: Figure showing partial traces of the electron spin-3/2 system under electron relaxation, starting from an electron inversion (blue) and a nuclear coherence (red). The parameters used ($A = 22$ MHz, $\gamma = 25$ Hz, $\beta = 0.02$) are representative of $^{15}\mathrm{N@C_{60}}$ and when fitted the curves give $T_{2n} = 0.3\, T_{1e}$.

If an experimentally lower ratio was observed this could be explained by an additional relaxation mechanism but a higher ratio is inconsistent with this model. One could consider that experimentally a combination of two curves are seen, one given by $0.3\,T_{1e}$ and the other by a stimulated echo dependent on T_{1e}, which with the presence of noise could result in a monoexponential decay curve giving $T_{2n} \sim 0.6\,T_{1e}$. However, careful analysis of the sequence and thorough phase cycling show that this is not the case. Additionally the labeling of the nuclear phase via a geometric phase, Section 4.3.4, showed conclusively that the experimentally observed decay is only due to a nuclear component. We therefore must produce a more complex model to understand the dynamics of the system. The relaxation rates (γ) can be modelled as varying between different pairs of levels. In the Lindblad equation γ can therefore be represented by both γ_1, the electron relaxation between the m_s levels $\pm 3/2 \leftrightarrow \pm 1/2$ and γ_2, the relaxation rate between m_s levels $1/2 \leftrightarrow -1/2$. This can be seen visually in Figure 5.7 and leads to a series of separate raising and lowering operators. Evaluating this unfortunately still gave $T_{2n} \sim 0.3\,T_{1e}$ or lower.

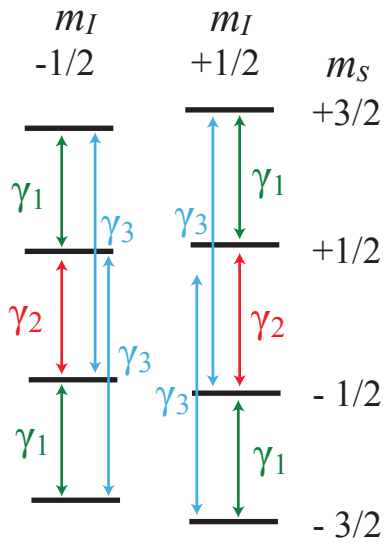

Figure 5.7: The $^{15}N@C_{60}$ level system shown with different relaxation rates, γ, used to model the system.

To understand the system in more detail we can look at the analytical solution to the model[1]. In the high temperature limit the nuclear spin dephasing rate is simply given by the relevant density matrix elements as $\Gamma_n = (3\gamma_1 + 4\gamma_2)$. The relevant observables for an electron polarisation measurement are $\dot{\rho}_{6,6} - \dot{\rho}_{7,7}$, this reduced subspace will give the same result as a trace over all elements but it is shown in Section 4.1 that only this *inner* coherence is measured:

$$\dot{\rho}_{6,6} - \dot{\rho}_{7,7} = 3\gamma_1\rho_{5,5} - (8\gamma_2 + 3\gamma_1)\rho_{6,6} + (8\gamma_2 + 3\gamma_1)\rho_{7,7} - 3\gamma_1\rho_{8,8}$$

and where

$$\dot{\rho}_{5,5} - \dot{\rho}_{8,8} = -3\gamma_1\rho_{5,5} + 3\gamma_1\rho_{6,6} - 3\gamma_1\rho_{7,7} + 3\gamma_1\rho_{8,8}$$

Taking $\dot{x} = \dot{\rho}_{6,6} - \dot{\rho}_{7,7}$, $\dot{y} = \dot{\rho}_{5,5} - \dot{\rho}_{8,8}$, $r_1 = 3\gamma_1$ and $r_2 = 8\gamma_2 + 3\gamma_1$, two coupled differential equations are found, shown in matrix form as:

$$\begin{pmatrix} \dot{x} \\ \dot{y} \end{pmatrix} = \begin{pmatrix} -r_2 & r_1 \\ r_1 & -r_1 \end{pmatrix} \begin{pmatrix} \rho_x \\ \rho_y \end{pmatrix} \tag{5.11}$$

Solving these the electron polarisation is expressed in terms of two parts:

$$P(t) = \alpha e^{-\lambda_- t} + \beta e^{-\lambda_+ t} \tag{5.12}$$

where α and β are prefactors which are a function of γ_1 and γ_2, and the eigenvalues λ are given by:

$$\lambda_\pm = \Gamma_n \pm \sqrt{(3\gamma_1)^2 + (4\gamma_2)^2} \tag{5.13}$$

A bi-exponential $T_{1\mathrm{e}}$ curve might therefore be expected, however the experimental curves shown in Figure 5.8 show a good fit to monoexponential decay. If the monoexponential decay corresponded to the faster decaying component, λ_+, then a minimum fundamental limit of $T_{2\mathrm{n}} \sim 1.7\, T_{1e}$ would be assured, fitting the experimental observation. However, taking the limits $\gamma_1 \gg \gamma_2$, $\gamma_2 \gg \gamma_1$ and $\gamma_1 \sim \gamma_2$, the signal ratio between

[1] a factor $\frac{1}{2}$ in the Lindblad equation has been incorporated into γ for simplicity.

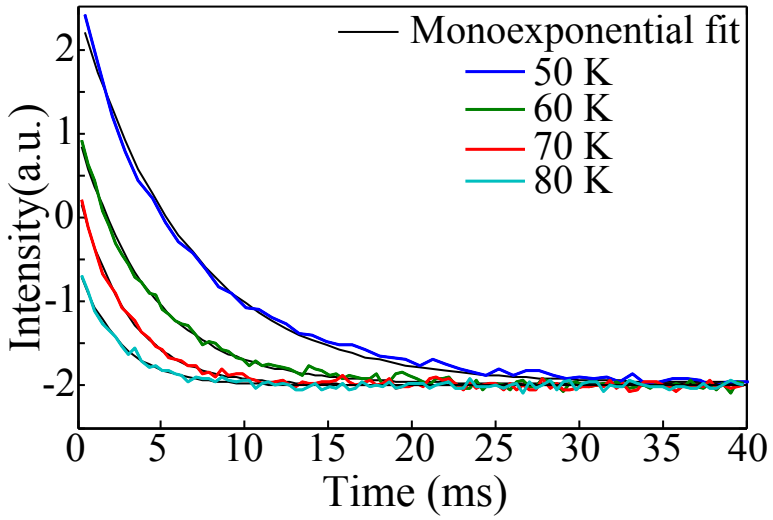

Figure 5.8: T_{1e} from 50–80 K fitted to monoexponential decays. Intensity has been offset for clarity, with fitted times shown in Figure 5.5.

the faster (λ_+) and slower component (λ_-) is 1:4, 1:9 and 1:200, respectively. Therefore, the monoexponential decay cannot correspond to λ_+ and the slower decaying component, λ_-, must be dominant. This gives a maximum ratio of $\lambda_- = \Gamma_e \sim 0.3\,\Gamma_n$ ($T_{2n} \sim 0.3\,T_{1e}$), when $3\gamma_1 = 4\gamma_2$, in accordance with the numerical model. Producing more sophisticated models to include additional pure dephasing and any zero field splitting (ZFS) distribution also resulted in the same limit.

To reconcile this ratio with the experimentally obtained $T_{2n} \sim 0.6\ T_{1e}$ additional relaxation processes must be included in the model, for instance, if γ_3 is given by $m_S = \pm 3/2 \leftrightarrow m_S = \mp 1/2$ (see Figure 5.7) then when $\gamma_1 = \gamma_3 = \gamma_2$ a theoretical T_{2n} of $2/3\ T_{1e}$ can be found (for 90% of the population, the remaining 10% will have an even larger decay time). The model can be expanded to allow transitions between any electron spin states by also adding the relaxation between m_S levels $3/2 \leftrightarrow -3/2$ at a rate of γ_4. The resulting decay gives a mono-exponential curve if $\gamma_1 = \gamma_2 = \gamma_3 = \gamma_4$, with a T_{2n}/T_{1e} ratio of 4/3. These conditions (equal γ rates) are congruent with a process that randomises the electron spin state, consistent with the Arrhenius T_{1e} mechanisms described in Section 3.5.5. Therefore, using additional terms a number of scenarios can be envisaged whereby the experimentally observed ratio will be seen. It would be useful to ascertain the differences in the relaxation rates experimentally, but unfortunately

the short *outer* coherence times (see earlier chapters) and inability to refocus these if any energy levels shifts occur, make this difficult. Nevertheless, this work opens up interesting questions with regards to the storage of quantum information in the nuclear spin states of higher electron spin systems. This could lead to theoretical proposals for materials that are expected to show much longer decoherence times between particular levels, similar to a decoherence free subspace. Possible materials could include those that have high spin impurities contained within a crystal lattice, such as the electron spin-5/2 Mn^{2+} impurity in a ZnO single crystal.

6

Nuclear relaxation

6.1 Introduction

We have shown that nuclear spins can be utilised to store quantum information, governed by T_{2n}, but they could also be used to hold classical information with relaxation times given by T_{1n}. Understanding this parameter allows us to fully characterise the system and although spin coherence times are usually limited by electron spin relaxation times, if these are improved, nuclear spin-lattice relaxation times may be of importance. T_{1n} has been studied extensively in NMR in the high concentration regime but few studies exist on Si:P and N@C_{60} in the low concentration regime, of interest for QIP. These materials have been probed using cw-EPR [FG59, MVTA07] but using

pulsed techniques T_{1n} can be more quickly and accurately extracted, eliminating experimental time dependence [TMAL06]. This chapter not only shows nuclear relaxation but also electron relaxation, which is found to be closely linked. It also makes use of higher frequency measurements and pulsed laser experiments, that can be used to induce relaxation and initialise the system.

6.2 Nuclear relaxation in Si:P

Nuclear relaxation can be measured using a variation of the Davies ENDOR sequence that was described in Section 4.2.1, without the additional π_{rf} pulse to 'tidy' the sequence. Having found the nuclear spin transition and optimised a π_{rf} pulse the nuclear spin relaxation can be observed by varying the shot repetition time of the sequence and monitoring the electron spin echo. Thus, the sequence will be:

$$[\pi_{mw} - \pi_{rf} - \pi/2_{mw} - \pi_{mw} - echo]_n \tag{6.1}$$

where n is the number of shots with a given shot repetition time (srt). If $T_{1n} > srt \gg T_{1e}$ then polarisation will build up as the system cannot fully relax before each shot, resulting in no ENDOR signal. However, in the regime $T_{1n} \sim srt \gg T_{1e}$ increasing the srt will allow the system to relax according to T_{1n}, which can be recorded by observing the subsequent increase in the ENDOR signal. This can be expressed as: $I_{\mathrm{ENDOR}} = 1 - \exp(-srt/T_{1n})$.

T_{1n} and T_{1e} data is shown in Figure 6.2 at both X-band (9-10 GHz) and W-band (94 GHz), for isotopically enriched ^{28}Si, $\sim 10^{15}$ and $\sim 10^{14}$ Pcm^{-1} concentration samples, respectively. The T_{1e} temperature dependence at X-band, above 7 K, is dominated by the Orbach relaxation process, discussed in Section 5.2.1, with relaxation driven by a two phonon mechanism via an excited state [Cas62, TLAR03]. This is shown pictorially in Figure 6.1 with an energy gap of 126 K [TLAR03]. At lower temperatures a 1st order Raman process becomes prominent which has a T^7 temperature dependence [FG59],

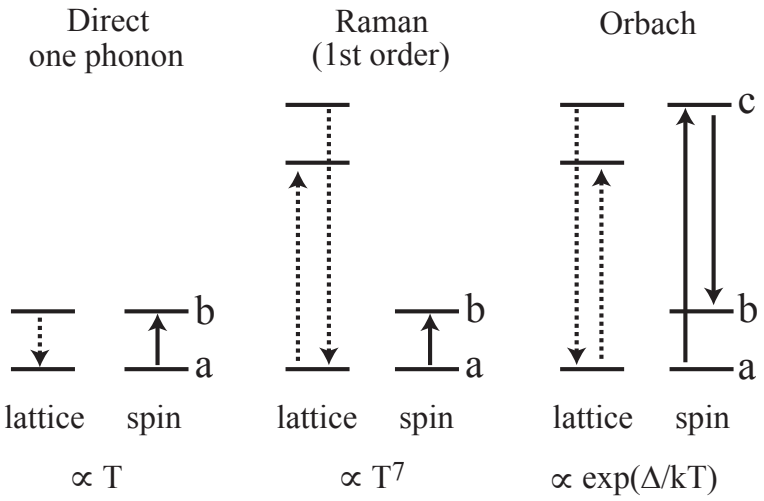

Figure 6.1: Pictorial representation of the direct (one phonon), 1st order Raman and Orbach relaxation mechanisms. Solid lines represent spin transitions and dashed lines lattice transitions. a and b indicate the two electron spin ground state levels between which relaxation occurs and c an excited state. Adapted from [BBL91].

again shown in Figure 6.1. Finally at very low temperatures (>5 K) it is known that a direct one phonon relaxation mechanism becomes significant, which follows a linear temperature dependance [FG59]. Thus, the T_{1e} data can be fitted to the three mechanisms described (as shown in Figure 6.2):

$$\frac{1}{T_{1e}} \propto [e^{(\Delta/k_B T)} - 1]^{-1} + T^7 + T \tag{6.2}$$

Unlike T_{1e}, T_{1n} has not been investigated in Si:P using pulsed experiments, at these low donor concentrations. Figure 6.2 shows that T_{1n} follows T_{1e} but is approximately a factor of 260 times longer and thus nuclear relaxation is similarly dominated by an Orbach relaxation process. This mechanism is not unusual for nuclear spins and has been previously observed for: Co^{59} nuclear spins in a paramagnetic system with an excited spin doublet [GS71]; ^{141}Pr nuclei via an excited crystal field level [SMY80] and ^{27}Al nuclei through an activated paramagnetic impurity [KYC00]. Similarly many examples of direct and Raman relaxation for nuclear spins have been shown [CN81, BP68, YN02, HN67]. However, the same mechanism for the nuclear and electron spin does not appear to have been widely shown. The similarity could be considered as

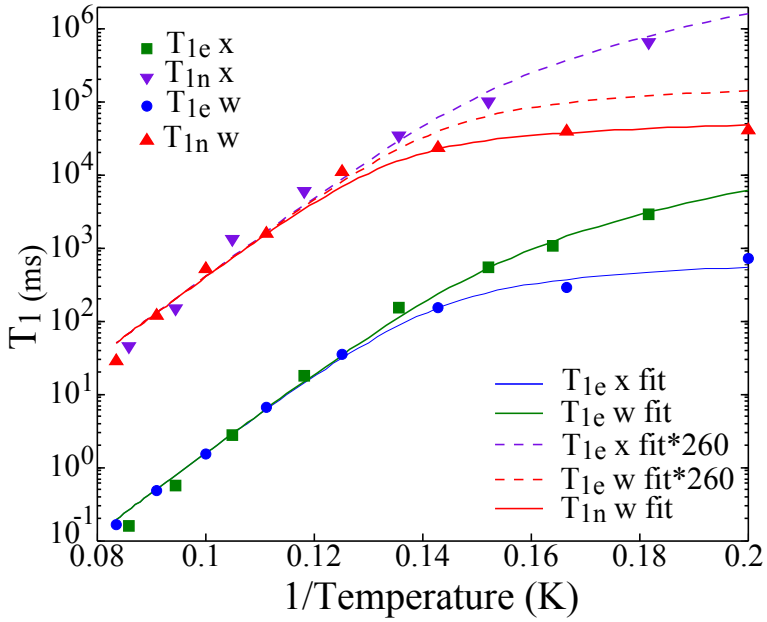

FIGURE 6.2: T_{1n} (purple, red) and T_{1e} (blue, green) data at both X-band (9-10 GHz) and W-band (94 GHz), denoted by 'x' and 'w', respectively. The T_{1e} and W-band T_{1n} data is fit to Eq. 6.2 shown by the solid lines. The dashed lines show the T_{1e} fit $\times 260$. The W-band data deviates slightly from the fixed ratio at low temperature, fitting better to a reduced limit for the one phonon term (solid red line, other parameters the same).

arising from the coupling of the nuclear and electron spin system through the hyperfine interaction. Nuclear relaxation could then occur via a flip-flop process with the electron spin, given by [Abr61a]:

$$\frac{1}{T_{1n}} = \frac{2}{3}A^2 \frac{\tau_e}{1+(\omega_I - \omega_S)^2\tau_e^2} S(S+1), \tag{6.3}$$

where τ_e the electron spin relaxation time. This would be dominated by the large electron Larmor frequency ($\omega_S \gg \omega_I$) resulting in a much slower T_{1n} than the experimentally observed. Alternatively, a nuclear spin flip could occur without an accompanying electron spin flop [Abr61b] but the following section on laser relaxation shows that the processes are not coupled. Therefore, it seems that both electron and nuclear spins are similarly affected by the same relaxation mechanisms but the origins of the T_{1e}/T_{1n} ratio are unknown.

To probe these mechanisms, experiments can be performed at a different mw frequency

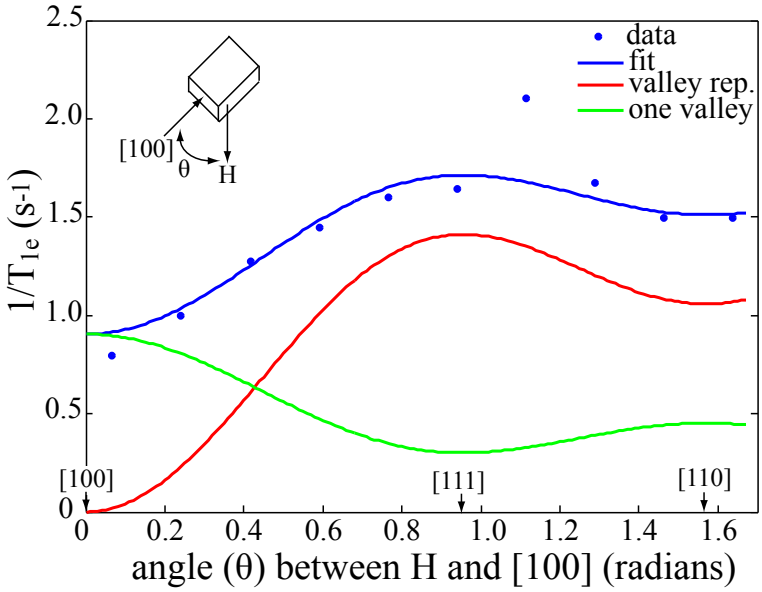

Figure 6.3: Angular dependence of T_{1e} at 5 K and ∼94 GHz. The contribution from a valley repopulation (red, Eq. 6.4) and a one valley (green, Eq. 6.5) mechanisms are shown. These are combined to give the blue fit to the experimental data.

to ascertain if any frequency dependence is present. Performing experiments at W-band (∼94 GHz) a superconducting magnet up to 6 T is used, with the larger Zeeman splitting giving an increase in sensitivity (such that samples are typically smaller but with similar concentration). As the Larmor frequency changes so do the rf resonant frequencies to approximately 116 MHz and 0.5 MHz. The latter of these is too low in frequency to be addressed using the commercial equipment available. Working at W-band introduced a number of difficulties in particular the rf pulse length must be increased tenfold to avoid heating of the sample and give good ENDOR efficiency. The relaxation results for W-band measurements are also shown in Figure 6.2. T_{1e} and T_{1n} show very similar results < 7 K to those at X-band which is not surprising given that the Orbach and Raman relaxation processes are not expected to be frequency dependent. The one phonon process is frequency dependent and was shown to give a T_{1e} limit at X-band of ∼3000 s by Feher and Gere [FG59] (crystal parallel to the [100] direction). In the high temperature limit, $k_BT \gg g\mu_BB_0$, this is expected to scale as B_0^4 [Rot60, Has60, FG59] but in the low temperature limit, $k_BT \ll g\mu_BB_0$, a B_0^5 dependence is predicted, shown in the supplementary material by Morello *et*

al. [MPZ10]. At 5 K we are in the regime $k_BT \sim g\mu_B B_0$ and, with the same crystal direction as Feher and Gere, show a limit of 1.25 s, which falls between the B_0^4 and B_0^5 dependence[1].

A range of relaxation times are actually observed, as shown in Figure 6.3, due to the angular dependence of the one phonon process. This angular dependence was shown at X-band [WF61] and we find it similarly holds at W-band but has a greater effect at higher temperatures, due to the earlier onset of the one phonon limit. The dependence has been shown to arise from two separate contributions: 1) a time dependent valley repopulation effect resulting in modulation of the g-tensor and 2) the modulation of the g shift within one valley [Rot60, Has60, WF61]. These mechanisms are used to fit the angular dependence data in Figure 6.3 and are given by:

$$\frac{1}{T_{1e}}(\text{valley rep.}) \propto \sin^2\theta(1+3\cos^2\theta) \tag{6.4}$$

$$\frac{1}{T_{1e}}(\text{one valley}) \propto \cos^4\theta + \frac{1}{2}\sin^4\theta \tag{6.5}$$

6.3 Nuclear relaxation in ^{15}N@C$_{60}$

The nuclear spin T_1 can be similarly probed using the same sequence outlined for Si:P. This sequence only works to probe the $m_s = \pm 3/2$ nuclear transitions as it is based on the Davies ENDOR sequence. Performing the measurements for the range 20–140 K, as with Si:P, a similar dependence with T_{1e} is seen, Figure 6.4. In this range T_{1e} was shown to follow an Arrhenius temperature dependence based on two phonon relaxation between the ground state and a metal-cage vibration mode, see Section 3.5.5. The data reveals an approximate T_{1n}/T_{1e} ratio of 180, a lower value than that of Si:P. Data at higher temperatures using ^{14}N@C$_{60}$ in liquid solution where T_{1e} is dependent on a cage vibrational mode showed similar results but with a slightly lower ratio of ~ 120 [Mor].

[1] In addition to the B_0 contribution Morello *et al.* also predict an effective increase in the B_0 pre-factor of 4/3 when moving to the low temperature limit.

The ratio and Arrhenius temperature dependence describes the T_{1n} data accurately in the range 60–140 K, deviates slightly with respect to the Arrhenius dependence between 25–60 K (due to deviation in T_{1e} values) and appears to break down at ≤ 20 K. This is consistent with the increasing dominance of an alternative T_{1e} mechanism below this temperature, but there is insufficient data to ascertain if T_{1n} is affected similarly to preserve the ratio or just deviates from the Arrhenius dependence. It is therefore clear that the same relaxation mechanisms are affecting both the nuclear and electron spin state. However, there is no theoretical insight into the exact reasons for the specific ratios found at the present moment.

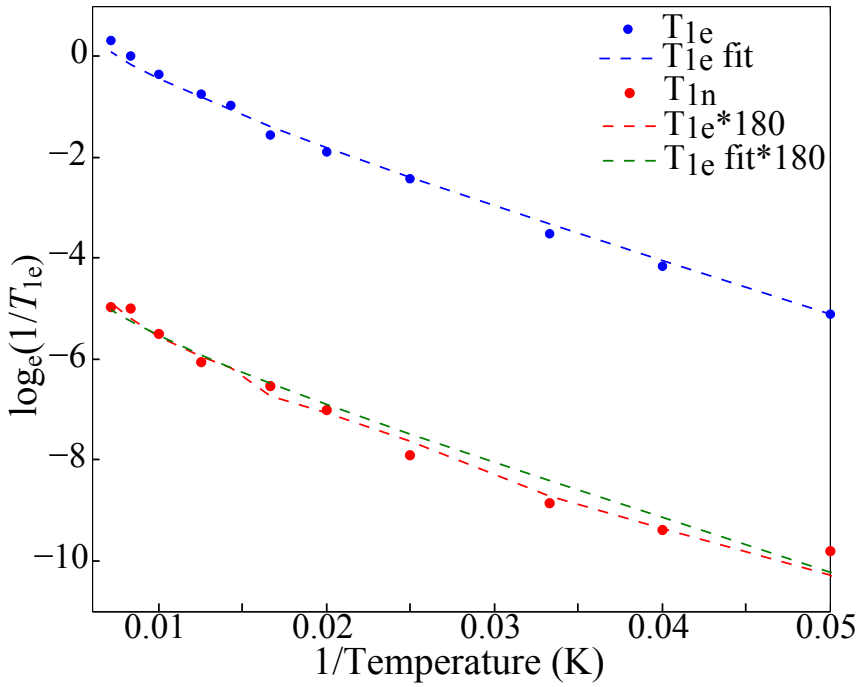

Figure 6.4: T_{1e} and T_{1n}, over the range 20–140 K, shown on an Arrhenius style plot. The T_{1e} data is fitted to an Arrhenius temperature dependence as shown in Section 3.5.5. The T_{1n} data follows the dependence but is approximately a factor 180 times larger, shown with comparison to the T_{1e} fit (green) and T_{1e} directly (red).

6.4 Laser relaxation in Si:P

In the previous sections we showed long relaxation times that are needed for the faithful storage of information. However, these cause problems for the initialisation of the system, a key requirement for QIP [DiV00]. Probing the Si:P system at low temperatures, several seconds are required to allow the electron to relax between experimental shots, to re-thermalise the levels. To produce high purity initial states an excess of population is required in a state such that it is hyperpolarised, as discussed in Section 4.4 and Ref [SBR11]. This can be established given a system whereby the electron spin relaxation time is faster than the nuclear spin relaxation time. However, the initialisation is relatively slow as several T_{1e} are required. To overcome this, light could be used to induce fast electronic relaxation, though this would not be effective if nuclear relaxation was also shown — entirely possible given the coupling of T_1 times shown in the previous sections. Naturally, this section will therefore not only show the effect of light, but if the electron and nuclear spin relaxation processes are coupled[2].

The use of light in Si:P systems has previously been shown to induce faster electronic relaxation [FG59] and more recently to specifically produce electron and nuclear hyperpolarisation [YSS09, MvTMB09]. The manuscript by Feher and Gere showed that above bandgap (1.1eV) light, can reduce T_{1e} from ∼1500 s to 300 s at 1.25 K (7×10^{15} P/cm^3 in natural silicon) [FG59]. The work by McCamey *et al.* [MvTMB09] used broadband white light but focused on nuclear polarisation with relaxation on the order of ∼150 s. Yang *et al.* [YSS09] in contrast showed both nuclear and electron polarisation via optical pumping, however, the photoluminescence detection is too slow to record the relaxation times (stated as < 1 s). The mechanisms works by above bandgap light exciting electrons from the valence to the conduction band, they then interact with the donor electrons causing them to relax. The effectiveness of the mechanism will be dependent on the number of conduction electrons produced and the time in which

[2]This approach can not be used with the N@C$_{60}$ system as it is known to be very light sensitive, however, given the similarities in the systems it is probable that the findings for Si:P will be applicable to N@C$_{60}$.

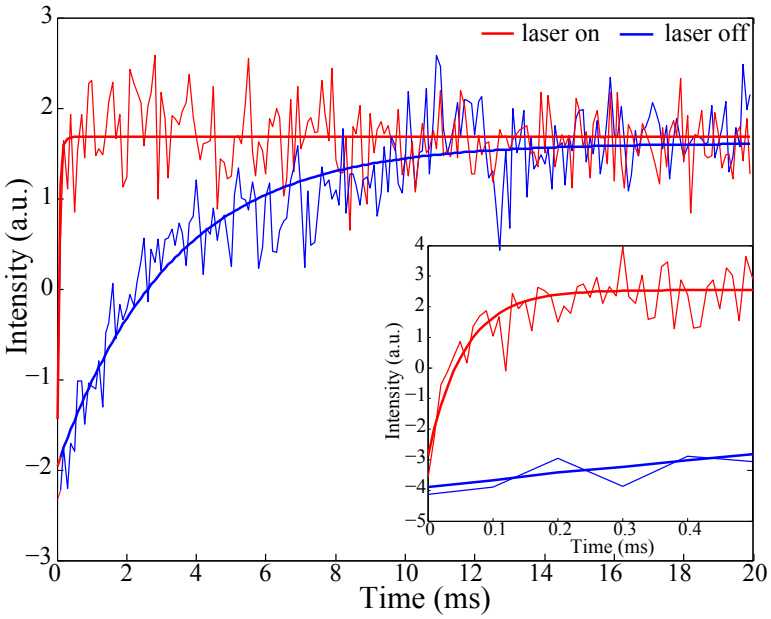

Figure 6.5: T_{1e} at 9 K under standard conditions (no laser) with a monoexponential fit to 3.26 ± 0.38 ms (blue), and with continuous 1060 nm laser illumination (red). The inset shows relaxation over the initial 500 μs from which a T_{1e} under laser illumination of 56 ± 16 μs is extracted.

these can relax the bound electron spin. A probable mechanism involves spin exchange during a collision of a conduction and bound electron, with the conduction electron subsequently undergoing recombination.

We show the direct effect of a 200 mW 1060 nm pulsed laser on the electron and nuclear spin relaxation times of Si:P. The laser is coupled to the sample via a quartz tube aligned with the optical window of the EPR cavity. At 9 K the effect of continuous laser illumination acts to dramatically reduce the electron relaxation time from 3.26 ± 0.38 ms to 56 ± 16 μs, as shown in Figure 6.5. This would improve the initialisation time (at this temperature) by more than a factor of 50, if the nuclear spin is not similarly effected. The nuclear spin can be probed by using a pulsed laser flash of 550 μs, which was found to be more than adequate to produce the rapid relaxation of the electron that is required.

A set of experiments can then be conducted based on Davies ENDOR to ascertain the effect of the laser and also serve to illustrate the need to leave the system in the correct

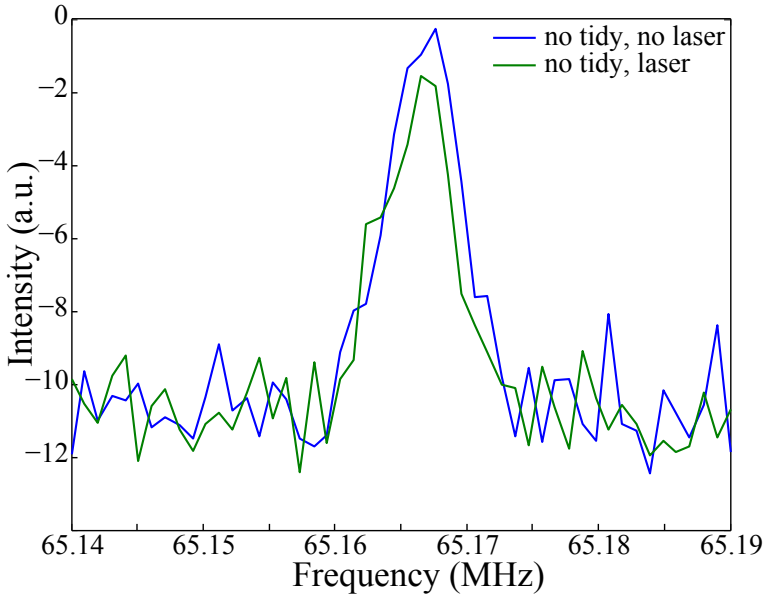

FIGURE 6.6: Davies ENDOR in the regime $T_{1e} \ll T_{1n} \ll$srt with (green) and without (blue) a laser pulse at the end of the sequence. The long srt means that the laser has no effect on the Davies ENDOR spectrum.

configuration to initialise. The latter can be conducted by using a final 'tidy' rf pulse at the end of the sequence, which allows the system to return under T_{1e} relaxation to a thermal state as shown in Ref [TMAL06]. We will refer to this sequence as 'tidy Davies ENDOR', where the 'tidy' pulse occurs sometime between the echo readout and the end of the experimental shot (but is typically at approximately half the shot repetition time (srt)) [MLHS08]. The three experimental timescales to conduct Davies ENDOR and tidy Davies ENDOR both with and without pulsed laser illumination are: 1) $T_{1e} \ll T_{1n} \ll$ srt 2) $T_{1e} <$ srt $< T_{1n}$ and 3) srt$\ll T_{1e} \ll T_{1n}$.

The condition $T_{1e} \ll T_{1n} \ll$ srt can be easily met at 9 K given the experimental T_{1n} data from the previous section. A srt of 2 seconds was found to be sufficient to give a good Davies ENDOR efficiency as shown in Figure 6.6 with the laser having no effect on the resonance. As the srt is longer than T_{1n} it negates the need to 'tidy' the sequence, however, moving to the regime $T_{1e} <$ srt $< T_{1n}$ this must be taken into consideration. Figure 6.7 shows both the standard and tidy Davies ENDOR sequences both with and without a final laser pulse before the end of each shot. The results clearly show that the 'tidy' pulse is required in order to observe Davies ENDOR but that the laser has

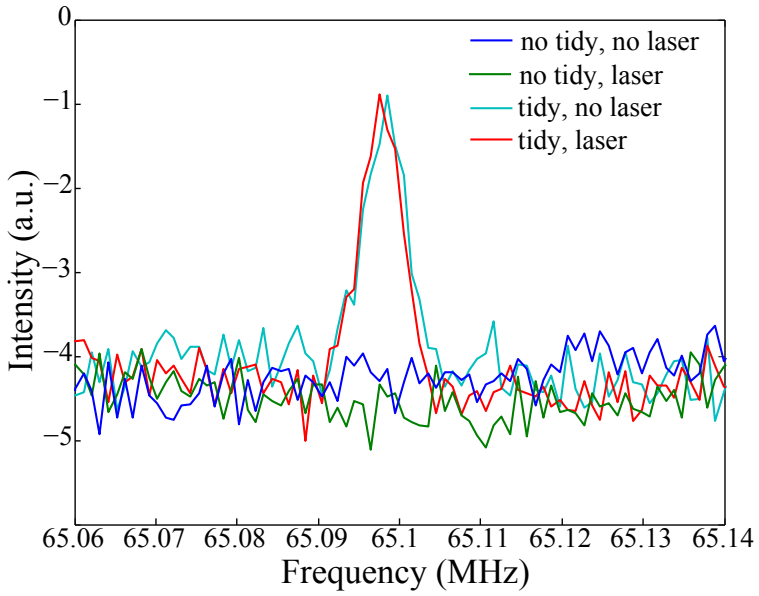

Figure 6.7: Davies ENDOR and tidy Davies ENDOR in the regime $T_{1e} < \text{srt} < T_{1n}$ with (green, red) and without (blue, cyan) a laser pulse at the end of the sequence. The use of the laser with a srt inbetween the electron and nuclear relaxation time shows that the laser has no effect on nuclear relaxation.

no effect on this result. As ENDOR is not visible without a tidy pulse but with the laser pulse, it indicates that the laser is not relaxing the nuclear spin.

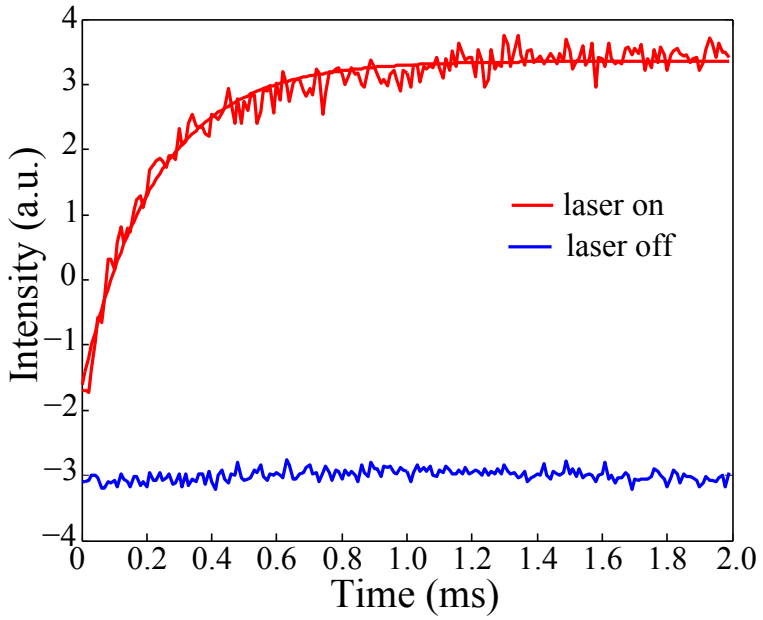

Figure 6.8: T_{1e} at 5.5 K under standard conditions (no laser, blue) and with a 5.5 ms laser 1060 nm pulse before each shot (red). A monoexponential fit to the laser relaxation gives a $T_{1e} = 228 \pm 12\mu$s (an initial very fast drop in intensity is also observed).

To obtain the condition srt$\ll T_{1e} \ll T_{1n}$ the system can be cooled to 5.5 K. At this temperature the effect of the laser on T_{1e} is again assessed in Figure 6.8. It is found that a longer 5.5 ms laser pulse is required to give a laser induced relaxation time of $228\pm12\mu$s, compared to the standard time of $\sim$2.9 s. Davies ENDOR is then performed with 'tidy' and laser variations, as shown in Figure 6.9.

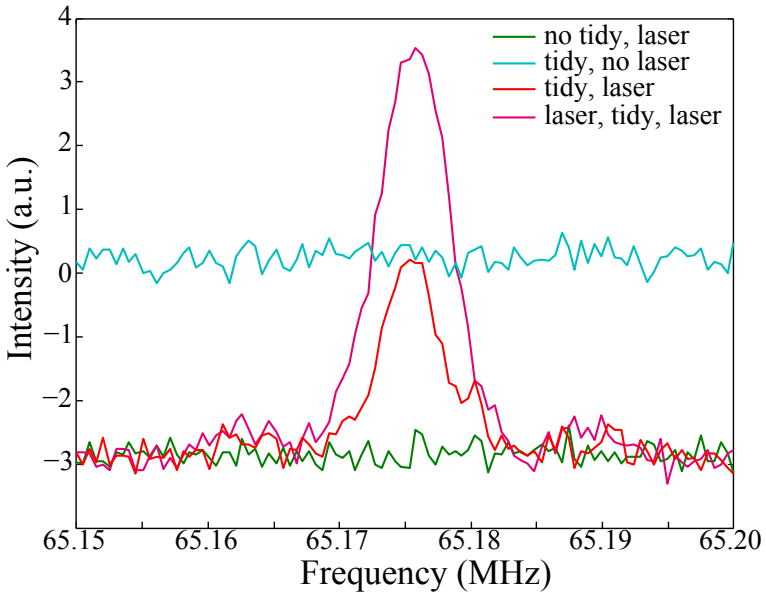

FIGURE 6.9: Davies ENDOR and tidy Davies ENDOR in the regime srt$\ll T_{1e} \ll T_{1n}$ with (green, red) and without (cyan) a laser pulse at the end of the sequence. Both a laser pulse to induce electron relaxation and a 'tidy' pulse to give the effect of nuclear relaxation, are required to give an observable ENDOR signal.

The results show that without both 'tidy' and the laser, no ENDOR signal is observed. This confirms that both the laser is required to relax the electron spin and the 'tidy' pulse to relax the nuclear spin state (when the srt is less than both relaxation times). Using the tidy sequence with the laser (red) both nuclear and electron spin are relaxed and ENDOR is observed with a visibility $F_{\text{ENDOR}} \sim 0.5$. Using a sequence whereby the electron is relaxed before a 'tidy' and final laser pulse are used, an $F_{\text{ENDOR}} \sim 1$ is observed (in the figure laser-tidy-laser (pink)). This arises as the laser relaxation acts to build polarisation in the nuclear manifold that is not at the resonant mw frequency, to give a standard echo readout (as opposed to the zero usually observed).

In conclusion this section shows that although electron and nuclear spins are similarly

affected by the same relaxation mechanisms, they are affected individually and not by coupling of the spin entities.

7

Conclusions

The drive to produce a quantum computer has produced many different qubit candidates and architectural schemes. Spin qubits are just one example but seem a natural extension to computing on the nano-scale, whilst utilising the power of quantum physics. In recent years this has lead to a plethora of literature in this area and although progress has been made, for instance single-shot single-spin detection [MPZ10], a functioning device by most estimates is tens of years away. The most successful implementation of a quantum algorithm to date was performed using nuclear spin qubits [VSB01] within an inherently non-scalable NMR approach. Moving to the the electron spin qubit (and EPR) the issues of scalability can be overcome (see Section 1.3.1) but one

of the major drawbacks of the electron spin system is the comparably short decoherence times[1]. In this thesis the electron spin relaxation and decoherence properties are probed in different molecular systems. Furthermore, a new technique is employed to transfer quantum information to the nuclear spin qubits, for both molecular and solid state schemes, with their properties investigated in the low concentration regime.

In Chapter 3 the electron spin decoherence times of several species of metallofullerene are investigated as a function of temperature and solvent environment. In previous studies, charge transfer from the metal atom to the fullerene cage was thought to limit T_{2e} to a few microseconds. However, using d-toluene T_{2e} has been extended to approximately 50, 60 and 90 μs for La@C_{82}, Sc@C_{82} and Y@C_{82}, respectively, with a limiting low temperature mechanism due to the slow rotation of the toluene solvent methyl group. Thus, using a d-orthoterphenyl solvent, without a methyl group, a T_{2e} of over 200 μs was found for all three metallofullerene species. Crucially, this puts metallofullerenes in a regime where, given the nanosecond manipulation times, quantum error correction is possible and they can be considered as a qubit candidate. Decoherence times $>$ 200 μs have been previously observed in liquid solution N@C_{60} samples but we now show this is also possible for powder ^{15}N@C_{60} samples. Using an instantaneous diffusion experiment, long selective pulses and d-orthoterphenyl samples we also extract an 'intrinsic' T_{2e} of over 400 μs, the longest reported molecular T_{2e} to date. Finally, we report T_{1e} as a function of temperature and find similarly for both metallofullerenes and ^{15}N@C_{60} that relaxation appears to be governed by an Arrhenius dependence due to a two phonon process resonant with atom-cage vibrational modes.

In Chapter 4 having investigated electron spin properties we turn to utilising the nuclear spin. The coherent transfer of quantum information between entities has not been widely illustrated, as shown in Section 1.5. We use an EPR sequence consisting of resonant mw and rf pulses to coherently move an arbitrary qubit from the electron to the nuclear spin degree of freedom and back. The sequence is verified by both directly probing the nuclear spin and by applying a time varying phase shift to the nuclear

[1] though this is offset by faster gate times.

coherence, that is recovered in the electron spin echo. The sequence is employed in two very different systems, a solid state Si:P single crystal and a molecular $^{15}N@C_{60}$ powder, to give a two-way fidelity of around 90% for the states ± X, Y, Z and the Identity. Process tomography has further been performed to obtain the process matrix for the scheme with a fidelity slightly lower than with the individual states. In the $^{15}N@C_{60}$ high spin system the transfer of states was shown for the *inner*, $m_S = +1/2 : -1/2$ levels, but the *outer*, $m_S = \pm 3/2 : \pm 1/2$ transitions, have also been investigated. This has revealed insights, such as the ability to probe the $m_s \pm 3/2$ nuclear spin levels though readout using the *inner* electron spin transition only. The molecular system also showed that the transfer can be used to effectively turn on and off inter-qubit (dipolar) coupling, a key requirement for QIP.

For the coherent transfer to be useful long nuclear T_2 times are required, which we probed in Chapter 5. This chapter showed that experimentally $T_{2\mathrm{n}}$ in both Si:P and $^{15}N@C_{60}$ is fundamentally limited by $T_{1\mathrm{e}}$. In Si:P a fundamental limit of $T_{2n} = 2T_{1e}$ was found and this was proved theoretically by modelling the system using both numerical and analytical approaches. In $^{15}N@C_{60}$, the high spin system gave an experimental limit of $T_{2n} \sim 0.6T_{1e}$, simple modelling of the system suggested the limit $T_{2n} \sim 0.3T_{1e}$ was expected, with the discrepancy reconciled by adding additional relaxation pathways to the model. At lower temperatures additional mechanisms limit $T_{2\mathrm{n}}$, which were improved in Si:P by dynamically decoupling the nuclear spin state to give a $T_{2\mathrm{n}}$ of 1.75 s at 5.5 K. In $^{15}N@C_{60}$, a $T_{2\mathrm{n}}$ up to 130 ms is reported, with both systems showing around three orders of magnitude improvement over the $T_{2\mathrm{e}}$ and thus a viable quantum memory.

In Chapter 6 the nuclear T_1 is investigated in the low concentration regime that cannot be probed using NMR. It is found that in both the Si:P and the $N@C_{60}$ system that $T_{1\mathrm{n}}$ is subject to the same relaxation mechanisms as $T_{1\mathrm{e}}$, dominated by a two-phonon (Orbach) process. In Si:P a constant ratio between $T_{1\mathrm{n}}$ and $T_{1\mathrm{e}}$ of approximately 260 is found which holds not only at X-band (9–10 GHz) but also at W-band (∼94 GHz). In $N@C_{60}$ a ratio of ∼180 is found but theory to explain these relationships has yet

to be produced. Relaxation of Si:P has been also investigated using a pulsed 1060 nm laser and found to substantially decrease the electron spin relaxation time, useful for initialisation of the system. It has been further verified that the laser does not effect the nuclear spin and thus, that the electron and nuclear relaxation mechanisms are not coupled but are independently effected by the same processes.

In summary the thesis shows new results pertaining to the understanding and improvement of electron spin relaxation times in molecular systems. The coherent transfer between electron and nuclear spin qubits has been successfully implemented in both Si:P and $^{15}N@C_{60}$. Furthermore, T_{2n} and T_{1n} times have been reported in the low concentration regime for the first time. These results address some of the fundamental problems of improving and understanding decoherence in spin qubit systems. I report significant steps towards the production of a hybrid quantum computer, illustrating crucial conventional computing requirements such as "memory" elements. However, substantial efforts are still required to produce multiple spin qubit architectures — molecular systems offer the advantage of a 'chemists toolkit', while Si:P architectures benefit from the ability to integrate with existing technology. Spin qubit schemes such as NV^- centres (recently showing two qubit coupling) and ion traps also offer considerable merit, but for any of these systems to produce a truly scalable strategy many 'landmark' experiments will still need to be accomplished.

List of Publications

A list of publications that I have written and contributed to are shown below in reverse chronological order. The thesis draws on some the work contained in these.

R. M. Brown, A. M. Tyryshkin, K. Porfyrakis, E. M. Gauger, B. W. Lovett, A. Ardavan, S. A. Lyon, G. A. D. Briggs and J. J. L. Morton, Coherent state transfer between an electron- and nuclear spin in $^{15}N@C_{60}$, *Phys. Rev. Lett.*, 106 110504, 2011.

S. Simmons, R. M. Brown, H. Riemann, N. V. Abrosimov, P. Becker, H-J. Pohl, M. L. W. Thewalt, K. M. Itoh and J. J. L. Morton, Entanglement in a solid state spin ensemble, *Nature*, 470 69, 2011.

R. M. Brown, Y. Ito, J. Warner, A. Ardavan, H. Shinohara, G. A. D. Briggs and J. J. L. Morton, Electron spin coherence in metallofullerenes: Y, Sc and $La@C_{82}$, *Phys. Rev. B*, 82 033410, 2010.

Y. Ito, J. H. Warner, R. M. Brown, M. Zaka, R. Pfeiffer, T. Aono, N. Izumi, H. Okimoto, J. J. L. Morton, A. Ardavan, H. Shinohara, H. Kuzmany, H. Peterlik and G. A. D. Briggs, Controlling intermolecular spin interactions of $La@C_{82}$ in empty fullerene matrices, *Phys. Chem. Chem. Phys.*, 12 1618, 2010.

J. J. L. Morton, A. M. Tyryshkin, R. M. Brown, S. Shankar, B. W. Lovett, A. Ardavan, T. Schenkel, E. E. Haller, J. W. Ager and S. A. Lyon, Solid state quantum memory using the ^{31}P nuclear spin, *Nature*, 455 1085, 2008.

Appendix: Raw data

Temp.	$Sc@C_{82}$ d-toluene		$La@C_{82}$ d-toluene		$Y@C_{82}$ d-toluene		$Y@C_{82}$ d-o-terphenyl	
(K)	T_{1e}(ms)	T_{2e}(ms)	T_{1e}(ms)	T_{2e}(ms)	T_{1e}(ms)	T_{2e}(ms)	T_{1e}(ms)	T_{2e}(ms)
6	-	-	54118	29.0	-	-	-	-
5	970000	36.3	-	-	1209000	27.0	22997	218.4
10	299000	22.0	6087	23.7	75191	18.0	14095	224.7
15	153000	20.3	2002	17.6	14421	16.3	7760	211.8
16.5	-	18.0	-	-	-	-	-	-
18	-	16.8	-	-	-	-	-	-
20	36000	-	973	18.4	4827	16.9	4558	222.7
22	-	16.1	-	-	-	-	-	-
25	20380	-	686	16.7	2461	14.7	2207	220.8
27	-	-	-	-	-	-	-	-
30	9218	-	503	18.9	1189	18.9	1343	192.0
32	-	15.9	-	-	-	-	-	-
35	4263	-	352	21.4	850	21.4	889	159.9
40	3346	19.8	260.6	27.0	556	32.8	595	152.4
45	2032	28.8	213.8	38.0	470	45.3	449	140.5
50	1532	32.4	158.8	40.6	380	60.8	363	135.0
55	815	57.9	133.0	41.7	340	70.4	293	124.8
60	698	59.0	111.0	48.5	243	79.1	240	115.9
65	412	58.6	99.1	43.4	226	84.7	197	95.9
70	366	50.2	88.4	39.7	195	79.0	163	83.2
75	216	50.7	69.4	33.7	151	68.3	134.4	71.9
80	211	42.6	64.6	26.2	116	57.1	103.4	61.2
85	147	37.3	51.9	22.7	97	48.1	89.2	48.6
90	100	23.5	40.1	17.5	83	41.7	71.1	41.8
95	86	17.9	29.7	9.4	73	32.4	61.0	34.4
100	55	11.1	25.1	8.2	57	26.0	55.8	31.3
105	55	8	-	-	40.8	11.5	46.3	25.0
110	25	4	-	-	49	7.0	41.0	22.2
115	25	2	-	-	37	4.8	29.6	16.5
120	-	-	-	-	23	2.8	27.6	13.7
125	-	-	-	-	21.8	2.3	28.5	12.5
130	-	-	-	-	17.4	0.9	25.0	9.1

Table 1: T_{1e} and T_{2e} times at varying temperatures for $Sc@C_{82}$, $La@C_{82}$ and $Y@C_{82}$ in deuterated toluene (and deuterated ortho-terphenyl for $Y@C_{82}$). Raw data from Figure 3.3, Figure 3.4 and Figure 3.6.

References

[AA87] Y. Aharonov and J. Anandan. Phase change during a cyclic quantum evolution. *Phys. Rev. Lett.*, 58(16):1593–1596, 1987.

[ABH05] J. W. Ager, J. W. Beeman, W. L. Hansen, E. E. Haller, I. D. Sharp, C. Liao, A. Yang, M. L. W. Thewalt, and H. Riemann. High-purity, isotopically enriched bulk silicon. *J. Electrochem. Soc.*, 152:G448–G451, 2005.

[Abr61a] A. Abraham. *The Principles of Nuclear Magnetism*, page 309. The Clarendon Press, Oxford, 1961.

[Abr61b] A. Abraham. *The Principles of Nuclear Magnetism*, page 380. The Clarendon Press, Oxford, 1961.

[ABW07] S. E. S. Andresen, R. Brenner, C. J. Wellard, C. Yang, T. Hopf, C.C. Escott, R. G. Clark, A. S. Dzurak, D. N. Jamieson, and L. C. L. Hollenberg. Charge state control and relaxation in an atomically doped silicon device. *Nano Lett.*, 7(7):2000–2003, 2007.

[AD87] H. Alloul and P. Dellouve. Spin localization in Si:P direct evidence from ^{31}P NMR. *Phys. Rev. Lett.*, 59(5):578–581, 1987.

[AFDC07] S. J. Angus, A. J. Ferguson, A. S. Dzurak, and R. G. Clark. Gate-defined quantum dots in intrinsic silicon. *Nano Lett.*, 7(7):2051–2055, 2007.

[AFDC08] S. J. Angus, A. J. Ferguson, A. S. Dzurak, and R. G. Clark. A silicon radio-frequency single electron transistor. *App. Phys. Lett.*, 92:112103, 2008.

[AMPW96] T. Almeida Murphy, Th. Pawlik, A. Weidinger, M. Höhne, R. Alcala, and J.-M. Spaeth. Observation of atomlike nitrogen in nitrogen-implanted solid C_{60}. *Phys. Rev. Lett.*, 77(6):1075–1078, 1996.

[ATT10] E. Abe, A. M. Tyryshkin, S. Tojo, J. J. L. Morton, W. M. Witzel, A. Fujimoto, J. W. Ager, E. E. Haller, J. Isoya, S. A. Lyon, M. L. W. Thewalt, and K. M. Itoh. Electron spin coherence of phosphorus donors in silicon: Effect of environmental nuclei. *Phys. Rev. B.*, 82(12):121201, 2010.

[BAB06] S. C. Benjamin, A. Ardavan, G. A. D. Briggs, D. A. Britz, D. Gunlycke, J. Jefferson, M. A. G. Jones, D. F. Leigh, B. W. Lovett, A. N. Khlobystov, S. A. Lyon, J. J. L. Morton, K. Porfyrakis, M. R. Sambrook, and A. M. Tyryshkin. Towards a fullerene-based quantum computer. *J. Phys. Condens. Matter*, 18(21):S867–S883, 2006.

[BBC95] A. Barenco, C.H. Bennett, R. Cleve, D.P. DiVincenzo, N. Margolus, P. Shor, T. Sleator, J.A. Smolin, and H. Weinfurter. Elementary gates for quantum computation. *Phys. Rev. A*, 52(5):3457–3467, 1995.

[BBFM06] S. C. Benjamin, D. E. Browne, J. Fitzsimons, and J. J. L. Morton. Brokered graph-state quantum computation. *New J. Phys.*, 8(8):141, 2006.

[BBL91] L. Banci, I. Bertini, and C. Luchinat. *Nuclear and electron relaxation.* VCH Weinheim, Basel, Cambridge, New York, 1991.

[BBM99] A. Barbon, M. Brustolon, A.L. Maniero, M. Romanelli, and L.C. Brunel. Dynamics and spin relaxation of tempone in a host crystal. An ENDOR, high field EPR and electron spin echo study. *Phys. Chem. Chem. Phys.*, 1(17):4015–4023, 1999.

[BC08] P. Bhattacharyya and B. K. Chakrabarti. The mean distance to the nth neighbour in a uniform distribution of random points: an application of probability theory. *European J. Phys.*, 29:639, 2008.

[BCB05] P. Bertet, I. Chiorescu, G. Burkard, K. Semba, C. Harmans, D. P. DiVincenzo, and J. E. Mooij. Dephasing of a superconducting qubit induced by photon noise. *Phys. Rev. Lett.*, 95(25):257002, 2005.

[BDEJ95] A. Barenco, D. Deutsch, A. Ekert, and R. Jozsa. Conditional quantum dynamics and logic gates. *Phys. Rev. Lett.*, 74(20):4083–4086, 1995.

[BdZR02] E. Biolatti, I. d'Amico, P. Zanardi, and F. Rossi. Electro-optical properties of semiconductor quantum dots: Application to quantum information processing. *Phys. Rev. B*, 65(7):075306, 2002.

[BEG04] M. Bourennane, M. Eibl, S. Gaertner, C. Kurtsiefer, A. Cabello, and H. Weinfurter. Decoherence-free quantum information processing with four-photon entangled states. *Phys. Rev. Lett.*, 92(10):107901, 2004.

[BEL00] G. Burkard, H. A. Engel, and D. Loss. Spintronics and quantum dots for quantum computing and quantum communication. *Fortschr. Phys*, 48(9-11):965–986, 2000.

[Ben01] S. C. Benjamin. Quantum computing without local control of qubit-qubit interactions. *Phys. Rev. Lett.*, 88(1):017904, 2001.

[BFBA10] B. B. Buckley, G. D. Fuchs, L. C. Bassett, and D. D. Awschalom. Spin-light coherence for single-spin measurement and control in diamond. *Science*, 330(6008):1212, 2010.

[BFP02] N. Boulant, E. M. Fortunato, M. A. Pravia, G. Teklemariam, D. G. Cory, and T. F. Havel. Entanglement transfer experiment in NMR quantum information processing. *Phys. Rev. A*, 65(2):24302, 2002.

[BKRB08] J. Benhelm, G. Kirchmair, C. F. Roos, and R. Blatt. Experimental quantum-information processing with $^{43}Ca^{+}$ ions. *Phys. Rev. A*, 77(6):62306, 2008.

[BL03] C. Boehme and K. Lips. Theory of time-domain measurement of spin-dependent recombination with pulsed electrically detected magnetic resonance. *Phys. Rev. B*, 68(24):245105, 2003.

[BNT09] G. Balasubramanian, P. Neumann, D. Twitchen, M. Markham, R. Kolesov, N. Mizuochi, J. Isoya, J. Achard, J. Beck, J. Tissler, et al. Ultralong spin coherence time in isotopically engineered diamond. *Nature Mater.*, 8(5):383–387, 2009.

[BP68] D. Beeman and P. Pincus. Nuclear spin-lattice relaxation in magnetic insulators. *Phys. Rev.*, 166(2):359–375, 1968.

[Bro07] P. G. Brooke. Decoherence-free quantum-information processing using dipole-coupled qubits. *Phys. Rev. A*, 75(2):022320, 2007.

[BTS06] F. R. Bradbury, A. M. Tyryshkin, G. Sabouret, J. Bokor, T. Schenkel, and S. A. Lyon. Stark tuning of donor electron spins in silicon. *Phys. Rev. Lett.*, 97(17):176404, 2006.

[BW08] R. Blatt and D. Wineland. Entangled states of trapped atomic ions. *Nature*, 453(7198):1008–1015, 2008.

[CAJ05] S. R. Clark, C. Moura Alves, and D. Jaksch. Efficient generation of graph states for quantum computation. *New J. Phys.*, 7:124, 2005.

[Cas62] T. G. Castner. Direct measurement of the valley-orbit splitting of shallow donors in silicon. *Phys. Rev. Lett.*, 8(1):13–15, 1962.

[CDLK08] K. S. Choi, H. Deng, J. Laurat, and H. J. Kimble. Mapping photonic entanglement into and out of a quantum memory. *Nature*, 452(7183):67–71, 2008.

[CFH97] D. G. Cory, A. F. Fahmy, and T. F. Havel. Ensemble quantum computing by NMR spectroscopy. *Proc. Natl. Acad. Sci*, 94(5):1634–1639, 1997.

[CGB10] I. Chiorescu, N. Groll, S. Bertaina, T. Mori, and S. Miyashita. Magnetic strong coupling in a spin-photon system and transition to classical regime. *Phys. Rev. B*, 82(2):024413, 2010.

[CGJ91] Y. Chai, T. Guo, C. Jin, R. E. Haufler, L. P. Felipe Chibante, J. Fure, L. Wang, M. Alford, and R. E. Smalley. Fullerenes with metals inside. *J. Phys. Chem*, 95(20):7564–7568, 1991.

[Chi06] Childress, L. and Gurudev Dutt, M. V. and Taylor, J. M. and Zibrov, A. S. and Jelezko, F. and Wrachtrup, J. and Hemmer, P. R. and Lukin, M. D. Coherent dynamics of coupled electron and nuclear spin qubits in diamond. *Science*, 314(5797):281–285, 2006.

[CL64] A. Carrington and G. R. Luckhurst. Electron spin resonance line widths of transition metal ions in solution. Relaxation through zero-field splitting. *Mol. Phys.*, 8(2):125–132, 1964.

[CLJ03] H. K. Cummins, G. Llewellyn, and J. A. Jones. Tackling systematic errors in quantum logic gates with composite rotations. *Phys. Rev. A*, 67:042308, 2003.

[CMJ05] T. Chanelière, D. N. Matsukevich, S. D. Jenkins, S.-Y. Lan, T. A. B. Kennedy, and A. Kuzmich. Storage and retrieval of single photons transmitted between remote quantum memories. *Nature*, 438(8):833–836, 2005.

[CN81] Mark S. Conradi and R. E. Norberg. Molecular H_2: Nuclear-spin-relaxation centers for protons in *a*-Si: H. *Phys. Rev. B*, 24(4):2285–2288, 1981.

[CP54] H. Y. Carr and E. M. Purcell. Effects of diffusion on free precession in nuclear magnetic resonance experiments. *Phys. Rev*, 94(3):630–638, 1954.

[CS96] A. R. Calderbank and P. W. Shor. Good quantum error-correcting codes exist. *Phys. Rev. A*, 54(2):1098–1105, 1996.

[CWB06] J.P. Cleuziou, W. Wernsdorfer, V. Bouchiat, T. Ondarçuhu, and M. Monthioux. Carbon nanotube superconducting quantum interference device. *Nat. Nanotechnol.*, 1:53–59, 2006.

[CWR07] L. E. Calvet, R. G. Wheeler, and M. A. Reed. Observation of the linear stark effect in a single acceptor in Si. *Phys. Rev. Lett.*, 98(9):096805, 2007.

[CY95] I.L Chuang and Y. Yamamoto. Simple quantum computer. *Phys. Rev. A*, 52(5):3489–3496, 1995.

[CZ95] J. L. Cirac and P. Zoller. Quantum Computations with Cold Trapped Ions. *Phys. Rev. Lett.*, 74(20):4091–4094, 1995.

[CZ02] Z-B. Chen and Y-D. Zhang. Greenberger-Horne-Zeilinger nonlocality for continuous-variable systems. *Phys. Rev. A*, 65(4B):441021–441024, 2002.

[DCJ07] M. V. Gurudev Dutt, L. Childress, L. Jiang, E. Togan, J. Maze, F. Jelezko, A. S. Zibrov, P. R. Hemmer, and M. D. Lukin. Quantum register based on individual electronic and nuclear spin qubits in diamond. *Science*, 316:1312–1316, 2007.

[Deu85] D. Deutsch. Quantum theory, the church-turing principle and the universal quantum computer. *Phil. Trans. R. Soc. A*, 400:97–117, 1985.

[DHJ03] A. S. Dzurak, L. C. L. Hollenberg, D. N. Jamieson, F. E. Stanley, C. Yang, T. M. Buhler, V. Chan, D. J. Reilly, C. Wellard, A. R. Hamilton, et al. Charge-based silicon quantum computer architectures using controlled single-ion implantation. *Arxiv preprint cond-mat/0306265 (unpublished)*, 2003.

[DHP99] E. Dietel, A. Hirsch, B. Pietzak, M. Waiblinger, K. Lips, A. Weidinger, A. Gruss, and K.P. Dinse. Atomic nitrogen encapsulated in fullerenes: Effects of cage variations. *J. Am. Chem. Soc*, 121(11):2432–2437, 1999.

[DiV00] D. P. DiVincenzo. The physical implementation of quantum computation. *Fortschr. Phys*, 48(9-11):771–783, 2000.

[DKKW00] K.P. Dinse, H. Käß, C. Knapp, and N. Weiden. EPR investigation of atoms in chemical traps. *Carbon*, 38(11-12):1635–1640, 2000.

[DRAS08] H. De Riedmatten, M. Afzelius, M.U. Staudt, C. Simon, and N. Gisin. A solid-state light–matter interface at the single-photon level. *Nature*, 456(7223):773–777, 2008.

[DS96] D.P. DiVincenzo and P.W. Shor. Fault-tolerant error correction with efficient quantum codes. *Phys. Rev. Lett.*, 77(15):3260–3263, 1996.

[Dur04] C. Durkan. Detection of single electronic spins by scanning tunnelling microscopy. *Contemp. Phys.*, 45(1):1–10, 2004.

[DW02] C. Durkan and M. E. Welland. Electronic spin detection in molecules using scanning-tunneling-microscopy-assisted electron-spin resonance. *App. Phys. Lett.*, 80:458, 2002.

[EHWvB04] J. M. Elzerman, R. Hanson, L. H. Willems van Beveren, B. Witkamp, L. M. K. Vandersypen, and L. P. Kouwenhoven. Single-shot read-out of an individual electron spin in a quantum dot. *Nature*, 430(6998):431–435, 2004.

[Feh59] G. Feher. Electron spin resonance experiments on donors in silicon. i. electronic structure of donors by the electron nuclear double resonance technique. *Phys. Rev.*, 114:1219–1244, 1959.

[Fey82] R. P. Feynman. Simulating physics with computers. *Int. J. Theor. Phys*, 21:467, 1982.

[FG59] G. Feher and E. A. Gere. Electron spin resonance experiments on donors in silicon. 2. electronic structure of donors by the electron nuclear double resonance technique. *Phys. Rev*, 114:1245–1256, 1959.

[FHH04] T. Fujisawa, T. Hayashi, Y. Hirayama, H. D. Cheong, and Y. H. Jeong. Electron counting of single-electron tunneling current. *App. Phys. Lett.*, 84(13):2343–2345, 2004.

[FRR07] M. Fuechsle, F.J. Rueß, T.C.G. Reusch, M. Mitic, and M.Y. Simmons. Surface gate and contact alignment for buried, atomically precise scanning tunneling microscopy–patterned devices. *J. Vac. Sci Technol. B*, 25:2562, 2007.

[FRS03] M. Friesen, P. Rugheimer, D.E. Savage, M.G. Lagally, D.W. van der Weide, R. Joynt, and M.A. Eriksson. Practical design and simulation of silicon-based quantum-dot qubits. *Phys. Rev. B.*, 67(12):121301, 2003.

[FT04] M. Feng and J. Twamley. Selective pulse implementation of two-qubit gates for spin-3/2-based fullerene quantum-information processing. *Phys. Rev. A*, 70(3):32318, 2004.

[FT06] J. Fitzsimons and J. Twamley. Globally controlled quantum wires for perfect qubit transport, mirroring, and computing. *Phys. Rev. Lett.*, 97(9):090502, 2006.

[FXBJ07] J. Fitzsimons, L. Xiao, S. C. Benjamin, and J. A. Jones. Quantum information processing with delocalized qubits under global control. *Phys. Rev. Lett.*, 99(3):030501, 2007.

[FYV00] L. Fedichkin, M. Yanchenko, and K. A. Valiev. Coherent charge qubits based on gaas quantum dots with a built-in barrier. *Nanotechnology*, 11(4):387–391, 2000.

[GB58] J. P Gordon and K.D. Bowers. Microwave spin echoes from donor electrons in silicon. *Phys. Rev. Lett.*, 1(10):368–370, 1958.

[GC97] N.A. Gershenfeld and I.L. Chuang. Bulk spin-resonance quantum computation. *Science*, 275(5298):350, 1997.

[GDP06] T. Gaebel, M. Domhan, I. Popa, C. Wittmann, P. Neumann, F. Jelezko, J.R. Rabeau, N. Stavrias, A.D. Greentree, S. Prawer, et al. Room-temperature coherent coupling of single spins in diamond. *Nature Phys.*, 2(6):408, 2006.

[GJFD02] J. Gallop, P. W. Josephs-Franks, J. Davies, L. Hao, and J. Macfarlane. Miniature dc SQUID devices for the detection of single atomic spin-flips. *Physica C*, 368(1-4):109–113, 2002.

[GLYY00] J. R. Goldman, T. D. Ladd, F. Yamaguchi, and Y. Yamamoto. Magnet designs for a crystal-lattice quantum computer. *App. Phys. A.*, 71(1):11–17, 2000.

[GOD06] A.D. Greentree, P. Olivero, M. Draganski, E. Trajkov, J.R. Rabeau, P. Reichart, B.C. Gibson, S. Rubanov, S.T. Huntington, D.N. Jamieson, et al. Critical components for diamond-based quantum coherent devices. *J. Phys.: Condens. Matter*, 18(21):825, 2006.

[GPMP10] F. Giazotto, J. T. Peltonen, M. Meschke, and J. P. Pekola. Superconducting quantum interference proximity transistor. *Nature Phys.*, 6(4):254–259, 2010.

[GRKS10] G. Gil-Ramírez, S. D. Karlen, A. Shundo, K. Porfyrakis, Y. Ito, G. A. D. Briggs, J. J. L. Morton, and H. L. Anderson. A cyclic porphyrin trimer as a receptor for fullerenes. *Org. Lett.*, 12(15):3544–3547, 2010.

[Gro99] L. K. Grover. Quantum Search on Structured Problems. *Chaos Solitons and Fractals*, 10(10):1695–1705, 1999.

[GS71] B. Gregory and G. Seidel. Nuclear relaxation via a two-phonon process in a paramagnetic system. *Phys. Rev. B*, 4(3):725–730, Aug 1971.

[GWR10] R. E. George, W. Witzel, H. Riemann, N. V. Abrosimov, N. Nötzel, M. L. W. Thewalt, and J. J. L. Morton. Electron spin coherence and electron nuclear double resonance of Bi donors in natural Si. *Phys. Rev. Lett.*, 105(6):067601, 2010.

[Höf96] P. Höfer. Multiple quantum pulsed endor spectroscopy by time proportional phase increment detection. *Appl. Magn. Reson.*, 11(3):375–389, 1996.

[Har02] W. Harneit. Fullerene-based electron-spin quantum computer. *Phys. Rev. A*, 65(3):032322, 2002.

[Has60] H. Hasegawa. Spin-lattice relaxation of shallow donor states in ge and si through a direct phonon process. *Phys. Rev.*, 118(6):1523–1534, 1960.

[HBS07] W. Harneit, C. Boehme, S. Schaefer, K. Huebener, K. Fostiropoulos, and K. Lips. Room temperature electrical detection of spin coherence in C_{60}. *Phys. Rev. Lett.*, 98(21):216601, 2007.

[HDW04] L. C. L. Hollenberg, A. S. Dzurak, C. Wellard, A. R. Hamilton, D. J. Reilly, G. J. Milburn, and R. G. Clark. Charge-based quantum computing using single donors in semiconductors. *Phys. Rev. B.*, 69(11):113301, 2004.

[HFE08] F. E. Hudson, A. J. Ferguson, C. C. Escott, C. Yang, D. N. Jamieson, R. G. Clark, and A. S. Dzurak. Gate-controlled charge transfer in Si:P double quantum dots. *Nanotechnology*, 19(19):195402, 2008.

[HH86] M. J. Hirsch and D. F. Holcomb. NMR study of Si:As and Si:P near the metal-insulator transition. *Phys. Rev. B*, 33(4):2520–2529, 1986.

[HHG08] H. Huebl, F. Hoehne, B. Grolik, A. R. Stegner, M. Stutzmann, and M. S. Brandt. Spin echoes in the charge transport through phosphorus donors in silicon. *Phys. Rev. Lett.*, 100(17):177602, 2008.

[HHG10] F. Hoehne, H. Huebl, B. Galler, M. Stutzmann, and M. S. Brandt. Spin-dependent recombination between phosphorus donors in silicon and Si/SiO_2 interface states investigated with pulsed electrically detected electron double resonance. *Phys. Rev. Lett.*, 104(4):046402, 2010.

[HHJ09] J. P. Home, D. Hanneke, J. D. Jost, J. M. Amini, D. Leibfried, and D. J. Wineland. Complete methods set for scalable ion trap quantum information processing. *Science*, 325(5945):1227, 2009.

[HMW02] W. Harneit, C. Meyer, A. Weidinger, D. Suter, and J. Twamley. Architectures for a spin quantum computer based on endohedral fullerenes. *physica status solidi (b)*, 233(3):453–461, 2002.

[HN67] J. B. Horak and A. W. Nolle. Electronic and nuclear magnetic relaxation in crystals with fluorite structure containing Eu^{2+} or Mn^{2+}. *Phys. Rev.*, 153(2):372–378, 1967.

[HOZ85] J. Heath, S. C. O'Brien, Q. Zhang, Y. Liu, R. F. Curl, H. W. Kroto, F. K. Tittel, and R. E. Smalley. Lanthanum complexes of spheroidal carbon shells. *J. Am. Chem. Soc.*, 107(25):7779–7780, 1985.

[IAB99] A. Imamoglu, D. D. Awschalom, G. Burkard, D. P. DiVincenzo, D. Loss, M. Sherwin, and A. Small. Quantum information processing using quantum dot spins and cavity QED. *Phys. Rev. Lett.*, 83(20):4204–4207, 1999.

[IS00] M. Inakuma and H. Shinohara. Temperature-dependent epr studies on isolated scandium metallofullerenes: Sc@C82 (I, II) and Sc@C84. *J. Phys. Chem. B*, 104(32):7595–7599, 2000.

[IWB10] Y. Ito, J.H. Warner, R. Brown, M. Zaka, R. Pfeiffer, T. Aono, N. Izumi, H. Okimoto, J.J.L. Morton, A. Ardavan, et al. Controlling intermolecular spin interactions of La@C82 in empty fullerene matrices. *Phys. Chem. Chem. Phys.*, 12(7):1618–1623, 2010.

[JBM06] M.A.G. Jones, D.A. Britz, J.J.L. Morton, A.N. Khlobystov, K. Porfyrakis, A. Ardavan, and G.A.D. Briggs. Synthesis and reactivity of N@C60O. *Phys. Chem. Chem. Phys.*, 8(17):2083–2088, 2006.

[JGDH08] P. Jakes, A. Gembus, K.P. Dinse, and K. Hata. Electron paramagnetic resonance investigation of metalloendofullerene derived carbon nanotube peapods. *J. Chem. Phys.*, 128:052306, 2008.

[JGP04a] F. Jelezko, T. Gaebel, I. Popa, M. Domhan, A. Gruber, and J. Wrachtrup. Observation of coherent oscillation of a single nuclear spin and realization of a two-qubit conditional quantum gate. *Phys. Rev. Lett.*, 93(13):130501, Sep 2004.

[JGP04b] F. Jelezko, T. Gaebel, I. Popa, A. Gruber, and J. Wrachtrup. Observation of Coherent Oscillations in a Single Electron Spin. *Phys. Rev. Lett.*, 92(7):76401, 2004.

[Joz98] R. Jozsa. *The Geometric Universe*. Oxford University Press, 1998.

[Joz03] R. Jozsa. On the role of entanglement in quantum-computational speed-up. *Proceedings of the Royal Society A: Mathematical, Physical and Engineering Sciences*, 459(2036):2011–2032, 2003.

[JPT05] A. C. Johnson, J. R. Petta, J. M. Taylor, A. Yacoby, M. D. Lukin, C. M. Marcus, M. P. Hanson, and A. C. Gossard. Triplet-singlet spin relaxation via nuclei in a double quantum dot. *Nature*, 435(7044):925–928, 2005.

[JSC04] B. Julsgaard, J. Sherson, J. I. Cirac, J. Fiuráek, and E. S. Polzik. Experimental demonstration of quantum memory for light. *Nature*, 432:482–486, 2004.

[JSD07] C. Ju, D. Suter, and J. Du. Two-qubit gates between noninteracting qubits in endohedral-fullerene-based quantum computation. *Phys. Rev. A*, 75(1):12318, 2007.

[JYH05] D. N. Jamieson, C. Yang, T. Hopf, S. M. Hearne, C. I. Pakes, S. Prawer, M. Mitic, E. Gauja, S. E. Andresen, F. E. Hudson, et al. Controlled shallow single-ion implantation in silicon using an active substrate for sub-20-keV ions. *App. Phys. Lett.*, 86:202101, 2005.

[KA62] J. R. Klauder and P. W. Anderson. Spectral diffusion decay in spin resonance experiments. *Phys. Rev.*, 125(3):912–932, 1962.

[Kan98] B. E. Kane. A silicon-based nuclear spin quantum computer. *Nature*, 393:133–137, 1998.

[KBAW00] P. G. Kwiat, A. J. Berglund, J. B. Altepeter, and A. G. White. Experimental verification of decoherence-free subspaces. *Science*, 290(5491):498–501, 2000.

[KBW04] A.N. Khlobystov, D.A. Britz, J. Wang, S.A. O'Neil, M. Poliakoff, and G.A.D. Briggs. Low temperature assembly of fullerene arrays in single-walled carbon nanotubes using supercritical fluids. *J. Mater. Chem.*, 14(19):2852–2857, 2004.

[KDP97] C. Knapp, K.P. Dinse, B. Pietzak, M. Waiblinger, and A. Weidinger. Fourier transform EPR study of N@C_{60} in solution. *Chem. Phys. Lett.*, 272(5-6):433–437, 1997.

[KGM98] S. Knorr, A. Grupp, M. Mehring, U. Kirbach, A. Bartl, and L. Dunsch. Pulsed ESR investigations of anisotropic interactions in M@C_{82} (M= Sc, Y, La). *App. Phys. A*, 66(3):257–264, 1998.

[KHK00] M. Krause, M. Hulman, H. Kuzmany, P. Kuran, L. Dunsch, TJS Dennis, M. Inakuma, and H. Shinohara. Low-energy vibrations in Sc2@C84 and Tm@C82 metallofullerenes with different carbon cages. *J. Mol. Struct.*, 521(1-3):325–340, 2000.

[KK02] M. Krause and H. Kuzmany. *Raman and infrared spectra of endohedral fullerenes*, page 169. Kluwer Academic Pub, 2002.

[KM] Ilya Kuprov and John J. L. Morton. Private Communication.

[KMR01] D. Kielpinski, V. Meyer, M. A. Rowe, C. A. Sackett, W. M. Itano, C. Monroe, and D. J. Wineland. A decoherence-free quantum memory using trapped ions. *Science*, 291(5506):1013–1015, 2001.

[KMW02] D. Kielpinski, C. Monroe, and D.J. Wineland. Architecture for a large-scale ion-trap quantum computer. *Nature*, 417(6890):709–711, 2002.

[KN03] K. Kobayashi and S. Nagase. Theoretical calculations of vibrational modes in endohedral metallofullerenes: La@C82 and Sc2@C84. *Mol. Phys.*, 101(1):249–254, 2003.

[KND03] K. Kobayashi, S. Nagase, and K.-P. Dinse. A theoretical study of spin density distributions and isotropic hyperfine couplings of N and P atoms in N@C60, P@C60, N@C70, N@C60(CH2)6, and N@C60(SiH2)6. *Chem. Phys. Lett.*, 377(1-2):93 – 98, 2003.

[KOB10] Y. Kubo, F. R. Ong, P. Bertet, D. Vion, V. Jacques, D. Zheng, A. Dréau, J.-F. Roch, A. Auffeves, F. Jelezko, J. Wrachtrup, M. F. Barthe, P. Bergonzo, and D. Esteve. Strong coupling of a spin ensemble to a superconducting resonator. *Phys. Rev. Lett.*, 105(14):140502, 2010.

[KRI91] V. V Kurshev, A. M Raitsimring, and T. Ichikawa. Spatial distribution of free radicals in. gamma.-irradiated alcohol matrixes determined by the 2+ 1 electron spin echo method. *J. Phys. Chem.*, 95(9):3564–3568, 1991.

[KRT89] V. V. Kurshev, A. M. Raitsimring, and Y. D. Tsvetkov. Selection of dipolar interaction by the 2+ 1 pulse train ESE. *J. Magn. Reson.*, 81(3):441–454, 1989.

[KSE07] L.J. Klein, D.E. Savage, and M.A. Eriksson. Coulomb blockade and Kondo effect in a few-electron silicon/silicon-germanium quantum dot. *App. Phys. Lett.*, 90:033103, 2007.

[KSK93] T. Kato, S. Suzuki, K. Kikuchi, Y. Achiba, D.A. Gibson, E.A. Carter, P. Boulas, F. D'Souza, C.C. Henderson, P.A. Cahill, et al. ESR study of the electronic structures of metallofullerenes: a comparison between lanthanum fullerene (La@C82) and scandium fullerene (Sc@C82). *J. Phys. Chem.*, 97(51):13425–13428, 1993.

[KWD05] C. Knapp, N. Weiden, and K. P. Dinse. Comparative EPR study of Cu@C60 and N@C60 endofullerenes. *Mag. Reson. Chem.*, 43(S1):S199–S204, 2005.

[KYC00] I. G. Kim, T. H. Yeom, S. H. Choh, K. S. Hong, Y. M. Yu, and E. S. Choi. 27Al NMR relaxation studies of an emerald single crystal. *Solid State Commun.*, 114(6):311–314, 2000.

[LANL] Los Alamos National Laboratory. http://qist.lanl.gov/qcomp_map.shtml.

[LBKF99] N. Linden, H. Barjat, Ē. Kupče, and R. Freeman. How to exchange information between two coupled nuclear spins: the universal SWAP operation. *Chem. Phys. Lett.*, 307(3-4):198–204, 1999.

[LD98] D. Loss and D. P. DiVincenzo. Quantum computation with quantum dots. *Phys. Rev. A.*, 57(1):120–126, 1998.

[LJP03] W. Lu, Z. Ji, L. Pfeiffer, KW West, and AJ Rimberg. Real-time detection of electron tunnelling in a quantum dot. *Nature*, 423(6938):422–425, 2003.

[LKK02] J. Lee, H. Kim, S.-J. Kahng, G. Kim, Y.-W. Son, J. Ihm, H. Kato, Z.W. Wang, T. Okazaki, H. Shinohara, and Y. Kuk. Bandgap modulation of carbon nanotubes by encapsulated metallofullerenes. *Nature*, 415(6875):1005–1008, 2002.

[Llo93] S. Lloyd. A Potentially Realizable Quantum Computer. *Science*, 261(5128):1569–1571, 1993.

[Llo99] S. Lloyd. Quantum search without entanglement. *Phys. Rev. A*, 61(1):10301, 1999.

[LOJ05] C. Langer, R. Ozeri, J. D. Jost, J. Chiaverini, B. DeMarco, A. Ben-Kish, R. B. Blakestad, J. Britton, D. B. Hume, W. M. Itano, D. Leibfried, R. Reichle, T. Rosenband, T. Schaetz, P. O. Schmidt, and D. J. Wineland. Long-lived qubit memory using atomic ions. *Phys. Rev. Lett.*, 95(6):060502, 2005.

[LRG91] Z. Levi, A. M Raitsimring, and D. Goldfarb. ESR and electron spin-echo studies of MnAlPO5. *J. Phys. Chem.*, 95(20):7830–7838, 1991.

[LRH98] S. Lebedkin, B. Renker, R. Heid, H. Schober, and H. Rietschel. A spectroscopic study of M@C82 metallofullerenes: Raman, far-infrared, and neutron scattering results. *Appl. Phys. A*, 66(3):273–280, 1998.

[LRW08] G. P. Lansbergen, R. Rahman, C. J. Wellard, I. Woo, J. Caro, N. Collaert, S. Biesemans, G. Klimeck, L. C. L. Hollenberg, and S. Rogge. Gate-induced quantum-confinement transition of a single dopant atom in a silicon FinFET. *Nature Phys.*, 4(8):656–661, 2008.

[LWS03] X. Li, Y. Wu, D. Steel, D. Gammon, T. H. Stievater, D. S. Katzer, D. Park, C. Piermarocchi, and L. J. Sham. An all-optical quantum gate in a semiconductor quantum dot. *Science*, 301(5634):809–811, 2003.

[Lyo06] S. Lyon. Spin-based quantum computing using electrons on liquid helium. *Phys. Rev. A*, 74(5):052338, 2006.

[MEH09] A. Morello, C. C. Escott, H. Huebl, L. H. Willems van Beveren, L. C. L. Hollenberg, D. N. Jamieson, A. S. Dzurak, and R. G. Clark. Architecture for high-sensitivity single-shot readout and control of the electron spin of individual donors in silicon. *Phys. Rev. B.*, 80(8):81307, 2009.

[MG58] S. Meiboom and D. Gill. Compensation for pulse imperfections in Carr–Purcell NMR experiments. *Rev. Sci. Inst*, 29(8):688–691, 1958.

[MHB06] D. R. McCamey, H. Huebl, M. S. Brandt, W. D. Hutchison, J. C. McCallum, R. G. Clark, and A. R. Hamilton. Electrically detected magnetic resonance in ion-implanted Si:P nanostructures. *App. Phys. Lett.*, 89(18):182115, 2006.

[MHL05] G. W. Morley, B. J. Herbert, S. M. Lee, K. Porfyrakis, T. J. S. Dennis, D. Nguyen-Manh, R. Scipioni, J. van Tol, A. P. Horsfield, A. Ardavan, et al. Hyperfine structure of Sc@C82 from ESR and DFT. *Nanotechnology*, 16(11):2469–2473, 2005.

[MKV09] T. Monz, K. Kim, A. S. Villar, P. Schindler, M. Chwalla, M. Riebe, C. F. Roos, H. Häffner, W. Hänsel, M. Hennrich, and R. Blatt. Realization of universal ion-trap quantum computation with decoherence-free qubits. *Phys. Rev. Lett.*, 103(20):200503, 2009.

[MLHS08] J. J. L. Morton, N. S. Lees, B. M. Hoffman, and S. Stoll. Nuclear relaxation effects in Davies ENDOR variants. *J. Magn. Reson.*, 191(2):315–321, 2008.

[MMK95] C. Monroe, D. M. Meekhof, B. E. King, W. M. Itano, and D. J. Wineland. Demonstration of a fundamental quantum logic gate. *Phys. Rev. Lett.*, 75(25):4714–4717, 1995.

[MMM10] M. H. Mohammady, G. W. Morley, and T. S. Monteiro. Bismuth qubits in silicon: The role of EPR cancellation resonances. *Phys. Rev. Lett.*, 105(6):067602, 2010.

[MMS03] M. Mehring, J. Mende, and W. Scherer. Entanglement between an electron and a nuclear spin 1 / 2. *Phys. Rev. Lett.*, 90:153001, 2003.

[MMS08] G. W. Morley, D. R. McCamey, H. A. Seipel, L.-C. Brunel, J. van Tol, and C. Boehme. Long-lived spin coherence in silicon with an electrical spin trap readout. *Phys. Rev. Lett.*, 101(20):207602, 2008.

[Mor] J. J. L. Morton. Private discussion.

[Mor05a] G. W. Morley. Designing a quantum computer based on pulsed electron spin resonance, DPhil Thesis, 2005.

[Mor05b] J. J. L. Morton. Electron spins in fullerenes as prospective qubits, DPhil Thesis, 2005.

[Mor10] A. Morello. Symposium Oxford University. 2010.

[MPC08] M. Mitic, K. D. Petersson, M. C. Cassidy, R. P. Starrett, E. Gauja, A. J. Ferguson, C. Yang, D. N. Jamieson, R. G. Clark, and A. S. Dzurak. Bias spectroscopy and simultaneous single-electron transistor charge state detection of Si:P double dots. *Nanotechnology*, 19(26):265201, 2008.

[MPZ10] A. Morello, J. J. Pla, F. A. Zwanenburg, K. W. Chan, K. Y. Tan, H. Huebl, M. Möttönen, C. D. Nugroho, C. Yang, J. A. van Donkelaar, et al. Single-shot readout of an electron spin in silicon. *Nature*, 467(7316):687–691, 2010.

[MSH08] J. R. Maze, P. L. Stanwix, J. S. Hodges, S. Hong, J. M. Taylor, P. Cappellaro, L. Jiang, M. V. G. Dutt, E. Togan, A. S. Zibrov, et al. Nanoscale magnetic sensing with an individual electronic spin in diamond. *Nature*, 455(7213):644–647, 2008.

[MSW04] M. Mehring, W. Scherer, and A. Weidinger. Pseudoentanglement of spin states in the multilevel $^{15}N@C_{60}$ system. *Phys. Rev. Lett.*, 93(20):206603, 2004.

[MTA05a] J. J. L. Morton, A. M. Tyryshkin, A. Ardavan, K. Porfyrakis, S. A. Lyon, and G. A. D. Briggs. High fidelity single qubit operations using pulsed electron paramagnetic resonance. *Phys. Rev. Lett.*, 95:200501, 2005.

[MTA05b] J. J. L. Morton, A. M. Tyryshkin, A. Ardavan, K. Porfyrakis, S. A. Lyon, and G. A. D. Briggs. A new mechanism for electron spin echo envelope modulation. *J. Chem. Phys.*, 122:174504, 2005.

[MTA06] J. J. L. Morton, A. M. Tyryshkin, A. Ardavan, K. Porfyrakis, S. A. Lyon, and G. A. D. Briggs. Electron spin relaxation of N@C_{60} in CS_2. *J. Chem. Phys.*, 124(1):014508, 2006.

[MTA07] J. J. L. Morton, A. M. Tyryshkin, A. Ardavan, K. Porfyrakis, S. A. Lyon, and G. A. D. Briggs. Environmental effects on electron spin relaxation in N@C_{60}. *Phys. Rev. B*, 76(8):085418, 2007.

[MTD08] J. J. L. Morton, A. Tiwari, G. Dantelle, K. Porfyrakis, A. Ardavan, and G. A. D. Briggs. Switchable $ErSc_2N$ rotor within a C_{80} fullerene cage: An EPR and photoluminescence excitation study. *Phys. Rev. Lett.*, 101(1):13002, 2008.

[MVTA07] G.W. Morley, J. Van Tol, A. Ardavan, K. Porfyrakis, J. Zhang, and G.A.D. Briggs. Efficient dynamic nuclear polarization at high magnetic fields. *Phys. Rev. Lett.*, 98(22):220501, 2007.

[MvTMB09] D. R. McCamey, J. van Tol, G. W. Morley, and C. Boehme. Fast nuclear spin hyperpolarization of phosphorus in silicon. *Phys. Rev. Lett.*, 102(2):027601, 2009.

[MWS10] G. W. Morley, M. Warner, A. M. Stoneham, P. T. Greenland, J. van Tol, C. W. M. Kay, and G. Aeppli. The initialization and manipulation of quantum information stored in silicon by bismuth dopants. *Nature Mater.*, 9(9):725–729, 2010.

[MWSPK79] W. Müller-Warmuth, R. Schüler, M. Prager, and A. Kollmar. A nuclear relaxation and neutron scattering study of the rotational states of methyl groups in solids with low hindering barriers. *J. Magn. Reson.*, 34(1):83–95, 1979.

[NBS10] P. Neumann, J. Beck, M. Steiner, F. Rempp, H. Fedder, P.R. Hemmer, J. Wrachtrup, and F. Jelezko. Single-shot readout of a single nuclear spin. *Science*, 329(5991):542, 2010.

[NC00a] M. A. Nielsen and I. L. Chuang. *Quantum computation and quantum information*. CUP, Cambridge, 2000.

[NC00b] M. A. Nielsen and I. L. Chuang. *Quantum computation and quantum information*, page 389. CUP, Cambridge, 2000.

[NIS04] E. Nishibori, K. Iwata, M. Sakata, M. Takata, H. Tanaka, H. Kato, and H. Shinohara. Anomalous endohedral structure of Gd@C_{82} metallofullerenes. *Phys. Rev. B*, 69(11):113412, 2004.

[NK93] S. Nagase and K. Kobayashi. Metallofullerenes M@C82 (M= Sc, Y, and La). A theoretical study of the electronic and structural aspects. *Chem. Phys. Lett.*, 214(1):57–63, 1993.

[NKN10] P. Neumann, R. Kolesov, B. Naydenov, J. Beck, F. Rempp, M. Steiner, V. Jacques, G. Balasubramanian, M. L. Markham, D. J. Twitchen, et al. Quantum register based on coupled electron spins in a room-temperature solid. *Nature Phys.*, 6(4):249–253, 2010.

[NMR08] P. Neumann, N. Mizuochi, F. Rempp, P. Hemmer, H. Watanabe, S. Yamasaki, V. Jacques, T. Gaebel, F. Jelezko, and J. Wrachtrup. Multipartite entanglement among single spins in diamond. *Science*, 320(5881):1326, 2008.

[NTS98] E. Nishibori, M. Takata, M. Sakata, M. Inakuma, and H. Shinohara. Determination of the cage structure of Sc@ C82 by synchrotron powder diffraction. *Chem. Phys. Lett.*, 298(1-3):79–84, 1998.

[NTS00] E. Nishibori, M. Takata, M. Sakata, H. Tanaka, M. Hasegawa, and H. Shinohara. Giant motion of La atom inside C82 cage. *Chem. Phys. Lett.*, 330(5-6):497–502, 2000.

[OATT02] K. Ono, D. G. Austing, Y. Tokura, and S. Tarucha. Current rectification by pauli exclusion in a weakly coupled double quantum dot system, 2002.

[OLK03] J.E. Ollerenshaw, D.A. Lidar, and L.E. Kay. Magnetic Resonance Realization of Decoherence-Free Quantum Computation. *Phys. Rev. Lett.*, 91(21):217904, 2003.

[OOS95] N. Okabe, Y. Ohba, S. Suzuki, S. Kawata, K. Kikuchi, Y. Achiba, and M. Iwaizumi. Fourier transform EPR studies of metallofullerene (La@C82) in CS2 solution. *Chem. Phys. Lett.*, 235(5-6):564–569, 1995.

[OPW03] J. L. O'Brien, G. J. Pryde, A. G. White, T. C. Ralph, and D. Branning. Demonstration of an all-optical quantum controlled-NOT gate. *Nature*, 426(6964):264–7, 2003.

[Orb61] R. Orbach. On the theory of spin-lattice relaxation in paramagnetic salts. *Proc. Phys. Soc.*, 77:821–826, 1961.

[OSS01] J. L. O'Brien, S. R. Schofield, M. Y. Simmons, R. G. Clark, A. S. Dzurak, N. J. Curson, B. E. Kane, N. S. McAlpine, M. E. Hawley, and G. W. Brown. Towards the fabrication of phosphorus qubits for a silicon quantum computer. *Phys. Rev. B*, 64(16):161401, Sep 2001.

[PdGHM07] J. H. Plantenberg, P. C. de Groot, C. J. P. M. Harmans, and J. E. Mooij. Demonstration of controlled-NOT quantum gates on a pair of superconducting quantum bits. *Nature*, 447(7146):836, 2007.

[PJT05] J. R. Petta, A. C. Johnson, J. M. Taylor, E. A. Laird, A. Yacoby, M. D. Lukin, C. M. Marcus, M. P. Hanson, and A. C. Gossard. Coherent manipulation of coupled electron spins in semiconductor quantum dots. *Science*, 309(5744):2180–2184, 2005.

[PLB10] S.-Y. Paik, S.-Y. Lee, W. J. Baker, D. R. McCamey, and C. Boehme. T_1 and T_2 spin relaxation time limitations of phosphorous donor electrons

near crystalline silicon to silicon dioxide interface defects. *Phys. Rev. B*, 81(7):075214, Feb 2010.

[PLF09] E. Prati, R. Latempa, and M. Fanciulli. Microwave-assisted transport in a single-donor silicon quantum dot. *Phys. Rev. B*, 80(16):165331, 2009.

[Pre98] J. Preskill. Reliable quantum computers. *Royal Society of London Proceedings Series A*, 454(1969), 1998.

[PSE96] G. M. Palma, K. A. Suominen, and A. K. Ekert. Quantum computers and dissipation. *Proc. R. Soc. London Ser. A*, 452:567, 1996.

[PTS07] R. Prevedel, M. S. Tame, A. Stefanov, M. Paternostro, M. S. Kim, and A. Zeilinger. Experimental demonstration of decoherence-free one-way information transfer. *Phys. Rev. Lett.*, 99(25):250503, 2007.

[Rau05] R. Raussendorf. Quantum computation via translation-invariant operations on a chain of qubits. *Phys. Rev. A*, 72(5):052301, 2005.

[RB01] R. Raussendorf and H. J. Briegel. A one-way quantum computer. *Phys. Rev. Lett.*, 86(22):5188–5191, 2001.

[RBB03] R. Raussendorf, D.E. Browne, and H.J. Briegel. Measurement-based quantum computation on cluster states. *Phys. Rev. A*, 68(2):22312, 2003.

[RBMC04] D. Rugar, R. Budaklan, H. J. Mamin, and B. W. Chul. Single spin detection by magnetic resonance force microscopy. *Nature*, 430(6997):329–332, 2004.

[RDD06] P. Rabl, D. DeMille, J. M. Doyle, M. D. Lukin, R. J. Schoelkopf, and P. Zoller. Hybrid quantum processors: Molecular ensembles as quantum memory for solid state circuits. *Phys. Rev. Lett.*, 97(3):033003, 2006.

[RidZB09] M. Rådmark, M. Żukowski, and M. Bourennane. Experimental test of fidelity limits in six-photon interferometry and of rotational invariance

properties of the photonic six-qubit entanglement singlet state. *Phys. Rev. Lett.*, 103(15):150501, 2009.

[RLR04] C. F. Roos, G. P. T. Lancaster, M. Riebe, H. Häffner, W. Hänsel, S. Gulde, C. Becher, J. Eschner, F. Schmidt-Kaler, and R. Blatt. Bell states of atoms with ultralong lifetimes and their tomographic state analysis. *Phys. Rev. Lett.*, 92(22):220402, 2004.

[Rot60] L.M. Roth. g factor and donor spin-lattice relaxation for electrons in germanium and silicon. *Phys. Rev.*, 118(6):1534–1540, 1960.

[RPR07] F. J. Ruess, W. Pok, T. C. Reusch, M. J. Butcher, K. E. Goh, L. Oberbeck, G. Scappucci, A. R. Hamilton, and M. Y. Simmons. Realization of atomically controlled dopant devices in silicon. *Small*, 3:563–567, 2007.

[RPS95] M. Rübsam, M. Plüschau, P. Schweitzer, K.P. Dinse, D. Fuchs, H. Rietschel, RH Michel, M. Benz, and MM Kappes. 2D EPR investigation of endohedral La@ C82 in solution. *Chem. Phys. Lett.*, 240(5-6):615–621, 1995.

[RWB07] R. Rahman, C. J. Wellard, F. R. Bradbury, M. Prada, J. H. Cole, G. Klimeck, and L. C. L. Hollenberg. High precision quantum control of single donor spins in silicon. *Phys. Rev. Lett.*, 99(3):036403, 2007.

[SBC11] D. I. Schuster, Lev S. Bishop, I. L. Chuang, D. DeMille, and R. J. Schoelkopf. Cavity QED in a molecular ion trap. *Phys. Rev. A*, 83(1):012311, 2011.

[SBD98] G. Seifert, A. Bartl, L. Dunsch, A. Ayuela, and A. Rockenbauer. Electron spin resonance spectra: geometrical and electronic structure of endohedral fullerenes. *App. Phys. A*, 66(3):265–271, 1998.

[SBH06] A.R. Stegner, C. Boehme, H. Huebl, M. Stutzmann, K. Lips, and M.S. Brandt. Electrical detection of coherent ^{31}P spin quantum states. *Nature Phys.*, 2(12):835–838, 2006.

[SBR11] S. Simmons, R. M. Brown, H. Riemann, N. V. Abrosimov, P. Becker, H. J. Pohl, M. L. W. Thewalt, K. M. Itoh, and J. J. L. Morton. Entanglement in a solid state spin ensemble. *Nature*, 470:69–72, 2011.

[SDK03] A. J. Skinner, M. E. Davenport, and B. E. Kane. Hydrogenic spin quantum computing in silicon: A digital approach. *Phys. Rev. Lett.*, 90(8):87901, 2003.

[SDR81] K. M. Salikhov, S. A. Dzuba, and A. M. Raitsimring. The theory of the ESE signal decay resulting from dipole-dipole interaction between paramagnetic centers in solids. *J. Mag. Res.*, 42:255, 1981.

[SF97] S. Saxena and J.H. Freed. Two-dimensional electron spin resonance and slow motions. *J. Phys. Chem. A*, 101(43):7998–8008, 1997.

[SFD10] D. I. Schuster, A. Fragner, M. I. Dykman, S. A. Lyon, and R. J. Schoelkopf. Proposal for manipulating and detecting spin and orbital states of trapped electrons on helium using cavity quantum electrodynamics. *Phys. Rev. Lett.*, 105(4):040503, 2010.

[Sho94] P. Shor. Algorithms for quantum computation: Discrete logarithms and factoring. *Proceedings of the 35th Annual Symposium on Foundations of Computer Science*, pages 124–134, 1994.

[Sho95] P.W. Shor. Scheme for reducing decoherence in quantum computer memory. *Phys. Rev. A*, 52(4):2493–2496, 1995.

[SJ01a] A. Schweiger and G. Jeschke. *Principles of Pulse Electron Paramagnetic Resonance*. Oxford University Press, Oxford, UK ; New York, 2001.

[SJ01b] A. Schweiger and G. Jeschke. *Principles of Pulse Electron Paramagnetic Resonance*, page 216. Oxford University Press, Oxford, UK ; New York, 2001.

[SJ01c] A. Schweiger and G. Jeschke. *Principles of Pulse Electron Paramagnetic Resonance*, page 414. Oxford University Press, Oxford, UK ; New York, 2001.

[SJ01d] A. Schweiger and G. Jeschke. *Principles of Pulse Electron Paramagnetic Resonance*, page 360. Oxford University Press, Oxford, UK ; New York, 2001.

[SJ01e] A. Schweiger and G. Jeschke. *Principles of Pulse Electron Paramagnetic Resonance*, page 384. Oxford University Press, Oxford, UK ; New York, 2001.

[SKHR03] F. Schmidt-Kaler, H. Haeffner, M. Riebe, S. Gulde, G.P.T. Lancaster, T. Deuschle, C. Becher, C.F. Roos, J. Eschner, and R. Blatt. Realization of the Cirac-Zoller controlled-NOT quantum gate. *Nature*, 422(6930):408–411, 2003.

[SKR04] F. Simon, H. Kuzmany, H. Rauf, T. Pichler, J. Bernardi, H. Peterlik, L. Korecz, F. Fülöp, and A. Jánossy. Low temperature fullerene encapsulation in single wall carbon nanotubes: synthesis of N@C_{60}@SWCNT. *Chem. Phys. Lett.*, 383(3-4):362–367, 2004.

[SKS10] C. B. Simmons, T. S. Koh, N. Shaji, M. Thalakulam, L. J. Klein, H. Qin, H. Luo, D. E. Savage, M. G. Lagally, A. J. Rimberg, R. Joynt, R. Blick, M. Friesen, S. N. Coppersmith, and M. A. Eriksson. Pauli spin blockade and lifetime-enhanced transport in a Si/SiGe double quantum dot. *Phys. Rev. B*, 82(24):245312, 2010.

[SL02a] D. Suter and K. Lim. Scalable architecture for spin-based quantum computers with a single type of gate. *Phys. Rev. A*, 65(5):052309, 2002.

[SL02b] D. Suter and K. Lim. Scalable architecture for spin-based quantum computers with a single type of gate. *Phys. Rev. A*, 65(5):052309, 2002.

[SM08] W. Scherer and M. Mehring. Entangled electron and nuclear spin states in $^{15}N@C_{60}$: Density matrix tomography. *J. Chem. Phys.*, 128(5):052305, 2008.

[SML99] B.W. Smith, M. Monthioux, and D.E. Luzzi. Carbon nanotube encapsulated fullerenes: a unique class of hybrid materials. *Chem. Phys. Lett.*, 315(1-2):31–36, 1999.

[SMP88] D. Suter, K. T. Mueller, and A. Pines. Study of the Aharonov-Anandan quantum phase by NMR interferometry. *Phys. Rev. Lett.*, 60(13):1218–1220, 1988.

[SMY80] R. M. Shelby, R. M. Macfarlane, and C. S. Yannoni. Optical measurement of spin-lattice relaxation of dilute nuclei: LaF_3:Pr^{3+}. *Phys. Rev. B*, 21(11):5004–5011, 1980.

[SS06] S. Stoll and A. Schweiger. EasySpin, a comprehensive software package for spectral simulation and analysis in EPR. *J. Magn. Reson.*, 178(1):42–55, 2006.

[SSG10] D. I. Schuster, A. P. Sears, E. Ginossar, L. DiCarlo, L. Frunzio, J. J. L. Morton, H. Wu, G. A. D. Briggs, B. B. Buckley, D. D. Awschalom, and R. J. Schoelkopf. High-cooperativity coupling of electron-spin ensembles to superconducting cavities. *Phys. Rev. Lett.*, 105(14):140501, 2010.

[SST08] N. Shaji, C. B. Simmons, M. Thalakulam, L. J. Klein, H. Qin, H. Luo, D. E. Savage, M. G. Lagally, A. J. Rimberg, R. Joynt, et al. Spin blockade and lifetime-enhanced transport in a few-electron Si/SiGe double quantum dot. *Nature Phys.*, 4:540–544, 2008.

[Ste96] A. M. Steane. Error correcting codes in quantum theory. *Phys. Rev. Lett.*, 77(5):793–797, 1996.

[Ste97] A. M. Steane. The ion trap quantum information processor. *App. Phys. B.*, 64(6):623–643, 1997.

[Ste07] A. M. Steane. How to build a 300 bit, 1 Giga-operation quantum computer. *Quantum Inf. Comput.*, 7(3):171–183, 2007.

[STHL10] S. Shankar, A. M. Tyryshkin, Jianhua He, and S. A. Lyon. Spin relaxation and coherence times for electrons at the Si/SiO_2 interface. *Phys. Rev. B*, 82(19):195323, 2010.

[STR09] C. B. Simmons, Madhu Thalakulam, B. M. Rosemeyer, B. J. Van Bael, E. K. Sackmann, D. E. Savage, M. G. Lagally, R. Joynt, Mark Friesen, S. N. Coppersmith, and M. A. Eriksson. Charge sensing and controllable tunnel coupling in a Si/SiGe double quantum dot. *Nano Lett.*, 9(9):3234–3238, 2009. PMID: 19645459.

[SW95] T. Sleator and H. Weinfurter. Realizable Universal Quantum Logic Gates. *Phys. Rev. Lett.*, 74(20):4087–4090, 1995.

[SWK98] R. J. Schoelkopf, P. Wahlgren, A. A. Kozhevnikov, P. Delsing, and D. E. Prober. The radio-frequency single-electron transistor (RF-SET): A fast and ultrasensitive electrometer. *Science*, 280(5367):1238, 1998.

[SYSW08] M. Sarovar, K. C. Young, T. Schenkel, and K. B. Whaley. Quantum nondemolition measurements of single donor spins in semiconductors. *Phys. Rev. B.*, 78(24):245302, 2008.

[TCT10] E. Togan, Y. Chu, A. S. Trifonov, L. Jiang, J. Maze, L. Childress, M. V. G. Dutt, A. S. Sørensen, P. R. Hemmer, A. S. Zibrov, and M. D. Lukin. Quantum entanglement between an optical photon and a solid-state spin qubit. *Nature*, 466(7307):730–734, 2010.

[THWH07] M. J. Testolin, C. D. Hill, C. J. Wellard, and L. C. L. Hollenberg. Robust controlled-not gate in the presence of large fabrication-induced variations of the exchange interaction strength. *Phys. Rev. A*, 76(1):012302, 2007.

[TLAR03] A. M. Tyryshkin, S. A. Lyon, A. V. Astashkin, and A. M. Raitsimring. Electron spin relaxation times of phosphorus donors in silicon. *Phys. Rev. B*, 68:193207, 2003.

[TMAL06] A. M. Tyryshkin, J. J. L. Morton, A. Ardavan, and S. A. Lyon. Davies electron-nuclear double resonance revisited: Enhanced sensitivity and nuclear spin relaxation. *J. Chem. Phys.*, 124:234508, 2006.

[TMB06] A. M. Tyryshkin, J. J. L. Morton, S. C. Benjamin, A. Ardavan, G. A. D. Briggs, J. W. Ager, and S. A. Lyon. Coherence of spin qubits in silicon. *J. Phys. Cond. Matt.*, 18:S783–S794, 2006.

[Tof80] T. Toffoli. Reversible computing automata, languages and programming, 7th colloquium (lecture notes in computer science 84) ed JW de Bakker and J van Leeuwen, 1980.

[TPK07] M. S. Tame, M. Paternostro, and M. S. Kim. One-way quantum computing in a decoherence-free subspace. *New J. Phys.*, 9(6):201, 2007.

[TTM11] A. M. Tyryshkin, S. Tojo, J. J. L. Morton, H. Riemann, N. V Abrosimov, P. Becker, H. J. Pohl, T. Schenkel, M. L. W. Thewalt, K. M. Itoh, and S. A. Lyon. Electron spin coherence exceeding seconds in high purity silicon. *Arxiv preprint*, arXiv:1105.3772, 2011.

[TUN95] M. Takata, B. Umeda, E. Nishibori, M. Sakata, Y. Saitot, M. Ohno, and H. Shinohara. Confirmation by X-ray diffraction of the endohedral nature of the metallofullerene Y@C82. *Nature*, 377(6544):46–49, 1995.

[Twa03] J. Twamley. Quantum-cellular-automata quantum computing with endohedral fullerenes. *Phys. Rev. A*, 67(5):52318, 2003.

[TY08] K.H. Takashi Yamamoto et al. Robust photonic entanglement distribution by state-independent encoding onto decoherence-free subspace. *Nature Photon.*, 2(8):488–491, 2008.

[vB08] L. van Beveren. Broadband electrically detected magnetic resonance of phosphorus donors in a silicon field-effect transistor. *App. Phys. Lett.*, 93(7), 2008.

[VFP01] L. Viola, E. M. Fortunato, M. A. Pravia, E. Knill, R. Laflamme, and D. G. Cory. Experimental realization of noiseless subsystems for quantum information processing. *Science*, 293(5537):2059–2063, 2001.

[VSB01] L. M. K. Vandersypen, M. Steffen, G. Breyta, C. S. Yannoni, M. H. Sherwood, and I. L. Chuang. Experimental realization of Shor's quantum factoring algorithm using nuclear magnetic resonance. *Nature*, 414:883–887, 2001.

[VYW00] R. Vrijen, E. Yablonovitch, K. Wang, H. W. Jiang, A. Balandin, V. Roychowdhury, T. Mor, and D. P. DiVincenzo. Electron-spin-resonance transistors for quantum computing in silicon-germanium heterostructures. *Phys. Rev. A*, 62(1):012306, 2000.

[WdSDS05] W. M. Witzel, R. de Sousa, and S. Das Sarma. Quantum theory of spectral-diffusion-induced electron spin decoherence. *Phys. Rev. B.*, 72(16):161306, 2005.

[WEO88] F. D. Weiss, J. L. Elkind, S. C. O'Brien, R. F. Curl, and R. E. Smalley. Photophysics of metal complexes of spheroidal carbon shells. *J. Am. Chem. Soc*, 110(13):4464–4465, 1988.

[WF61] D. K. Wilson and G. Feher. Electron spin resonance experiments on donors in silicon. III. Investigation of excited states by the application of uniaxial stress and their importance in relaxation processes. *Phys. Rev.*, 124(4):1068–1083, 1961.

[WGW10] H. Wu, R. E. George, J. H. Wesenberg, K. Mølmer, D. I. Schuster, R. J. Schoelkopf, K. M. Itoh, A. Ardavan, J. J. L. Morton, and G. A. D. Briggs.

Storage of multiple coherent microwave excitations in an electron spin ensemble. *Phys. Rev. Lett.*, 105(14):140503, 2010.

[WHS07] W. M. Witzel, Xuedong Hu, and S. Das Sarma. Decoherence induced by anisotropic hyperfine interaction in si spin qubits. *Phys. Rev. B*, 76(3):035212, 2007.

[WIZ08] J. H. Warner, Y. Ito, M. Zaka, L. Ge, T. Akachi, H. Okimoto, K. Porfyrakis, Andrew A. R. Watt, H. Shinohara, and G. A. D. Briggs. Rotating fullerene chains in carbon nanopeapods. *Nano Lett.*, 8(8):2328–2335, 2008.

[WKD99] N. Weiden, H. Kass, and K. P. Dinse. Pulse Electron Paramagnetic Resonance (EPR) and Electron- Nuclear Double Resonance (ENDOR) Investigation of N@C60 in Polycrystalline C60. *J. Phys. Chem. B*, 103(45):9826–9830, 1999.

[WKD04] N. Weiden, T. Kato, and K.P. Dinse. Hyperfine Interactions in La@ C82 Studied by W-Band Electron Paramagnetic Resonance and Electron Nuclear Double Resonance. *J. Phys. Chem. B*, 108(27):9469–9474, 2004.

[WLH01] M. Waiblinger, K. Lips, W. Harneit, A. Weidinger, E. Dietel, and A. Hirsch. Thermal stability of the endohedral fullerenes N@C_{60}, N@C_{70}, and P@C_{60}. *Phys. Rev. B.*, 64(15):159901, 2001.

[WLS05] D. Wei, J. Luo, X. Sun, X. Zeng, M. Zhan, and M. Liu. Realization of a decoherence-free subspace using multiple quantum coherences. *Phys. Rev. Lett.*, 95(2):020501, 2005.

[WRR05] P. Walther, K. J. Resch, T. Rudolph, E. Schenck, H. Weinfurter, V. Vedral, M. Aspelmeyer, and A. Zeilinger. Experimental one-way quantum computing. *Nature*, 434:169–176, 2005.

[WS88] J. S. Waugh and C. P. Slichter. Mechanism of nuclear spin-lattice relaxation in insulators at very low temperatures. *Phys. Rev. B*, 37(8):4337–4339, 1988.

[WSSW10] L. Wang, K. Shen, B. Y. Sun, and M. W. Wu. Singlet-triplet relaxation in multivalley silicon single quantum dots. *Phys. Rev. B*, 81(23):235326, Jun 2010.

[WW74] R. E Walstedt and L. R Walker. Nuclear-resonance line shapes due to magnetic impurities in metals. *Phys. Rev. B.*, 9(11):4857–4867, 1974.

[WZ82] W. K. Wootters and W. H. Zurek. A single quantum cannot be cloned. *Nature*, 299:802 – 803, 1982.

[XHJ10] M. Xiao, M. G. House, and H. W. Jiang. Measurement of the spin relaxation time of single electrons in a silicon metal-oxide-semiconductor-based quantum dot. *Phys. Rev. Lett.*, 104(9):096801, 2010.

[YN02] S. Yamamoto and T. Nakanishi. Spin-wave description of nuclear spin-lattice relaxation in $Mn_{12}O_{12}$ acetate. *Phys. Rev. Lett.*, 89(15):157603, 2002.

[YSS09] A. Yang, M. Steger, T. Sekiguchi, M. L. W. Thewalt, T. D. Ladd, K. M. Itoh, H. Riemann, N. V. Abrosimov, P. Becker, and H.-J. Pohl. Simultaneous subsecond hyperpolarization of the nuclear and electron spins of phosphorus in silicon by optical pumping of exciton transitions. *Phys. Rev. Lett.*, 102(25):257401, 2009.

[YXW10] W.L. Yang, Z.Y. Xu, H. Wei, M. Feng, and D. Suter. Quantum-information-processing architecture with endohedral fullerenes in a carbon nanotube. *Phys. Rev. A*, 81(3):32303, 2010.

[ZS69] G. M. Zhidomirov and K. M. Salikhov. Contribution to the theory of spectral diffusion in magnetically diluted solids. *Sov. Phys. JETP*, 29:1037, 1969.

[ZWI10] M. Zaka, Y. Ito, J. H. Warner, Y. Ito, J. J. L. Morton, M.H. Rümmeli, T. Pichler, A. Ardavan, H. Shinohara, and G. A. D. Briggs. Exchange interactions of spin-active metallofullerenes in solid-state carbon networks. *Phys. Rev. B*, 81(7):075424, 2010.